

**Characterization of the  
hyperpolarization-activated, highly-selective  
proton channel HCNL1 found in the sperm  
of the zebrafish *Danio rerio***

**Dissertation**

zur

Erlangung des Doktorgrades (Dr. rer. nat.)

der

Mathematisch-Naturwissenschaftlichen Fakultät

der

Rheinischen Friedrich-Wilhelms-Universität Bonn

vorgelegt von

**Lea Wobig**

aus

Düsseldorf

Bonn 2020



Angefertigt mit Genehmigung der Mathematisch-Naturwissenschaftlichen Fakultät der  
Rheinischen Friedrich-Wilhelms-Universität Bonn

1. Gutachter: Prof. Dr. U. B. Kaupp

2. Gutachter: Prof. Dr. M. Pankratz

Tag der Promotion: 25.02.2021

Erscheinungsjahr: 2021



# Abstract

---

Zebrafish are external fertilizers and release their gametes into the surrounding water. Yet, the freshwater environment with its low osmolarity poses a challenge for the gametes. Given these unique ion conditions, it seems likely that zebrafish sperm have evolved specialized ion channels that are adapted to the freshwater environment. However, very little is known about the sperm of freshwater fish.

Another field that is still poorly understood is that of proton channels. Proton channels are exceptional among ion channels. Since protons differ substantially from other ions in their properties, their permeation pathways are very different from those of other ion channels. Proton channels select protons against other ions that are up to a million-fold more abundant, and only a few have been identified so far.

In my PhD thesis, I characterized a novel proton channel that belongs to the HCN channel family and is found in zebrafish sperm (drHCNL1). Despite its overall similarity to classical HCN channels that conduct  $K^+$  and  $Na^+$ , drHCNL1 is exquisitely selective for protons. Activated by hyperpolarization, it conducts protons into the cytosol under physiological conditions, whereas the only other known voltage-gated proton channel,  $H_v1$ , is activated by depolarization and expels protons from the cell. Remarkably, protons permeate through drHCNL1's voltage-sensing domain, whereas the "classical" pore domain is non-functional. Crucial for this proton permeation pathway is a methionine residue, which interrupts the series of regularly spaced arginine residues in the S4 voltage sensor. DrHCNL1 forms a tetramer and thus contains four proton pores. In contrast to classical HCN channels, drHCNL1 is not modulated by cyclic nucleotides. Another ion channel in zebrafish sperm previously identified, drCNGK, is also insensitive to cyclic nucleotides and, instead, is controlled by intracellular pH. My results suggest that both channels are functionally related, and that protons rather than cyclic nucleotides serve as cellular messengers in zebrafish sperm. The primary function of HCN channels is to depolarize the cell after hyperpolarization. In freshwater that is extremely low in  $Na^+$ , a channel conducting  $Na^+$  would hyperpolarize sperm even further. Through small modifications in two key functional domains, drHCNL1 has been transformed to a proton-selective channel and thus evolutionarily adapted to the freshwater environment so that the sperm's ability to depolarize is conserved.

# Zusammenfassung

---

Zebrafische pflanzen sich durch externe Befruchtung fort und geben hierzu ihre Gameten in das umgebende Wasser ab. Die Süßwasserumgebung mit ihrer geringen Osmolarität stellt jedoch eine besondere Herausforderung für die Gameten dar. Angesichts dieser einzigartigen Ionenbedingungen scheint es wahrscheinlich, dass die Spermien des Zebrafisches spezialisierte Ionenkanäle entwickelt haben, die an die Süßwasserumgebung angepasst sind. Über die Spermien von Süßwasserfischen ist jedoch sehr wenig bekannt.

Ein weiteres Feld, das noch wenig verstanden ist, ist das der Protonenkanäle. Protonenkanäle sind unter den Ionenkanälen eine Besonderheit. Da sich Protonen in ihren Eigenschaften wesentlich von anderen Ionen unterscheiden, erfolgt ihre Permeation auf eine ganz andere Art und Weise als die von anderen Ionen. Protonenkanäle selektieren für Protonen gegen andere Ionen, die bis zu einer Million Mal häufiger vorkommen, und nur wenige wurden bisher identifiziert.

In meiner Doktorarbeit habe ich einen neuartigen Protonenkanal charakterisiert, der zur Familie der HCN-Kanäle gehört, und in den Spermien von Zebrafischen (drHCNL1) vorkommt. Trotz seiner prinzipiellen Ähnlichkeit mit klassischen HCN-Kanälen, die  $K^+$  und  $Na^+$  leiten, ist drHCNL1 ein äußerst selektiver Protonenkanal. Durch Hyperpolarisation aktiviert, leitet es Protonen in das Zytosol. Damit ist er das genaue Gegenteil des bisher einzigen anderen bekannten spannungsgesteuerten Protonenkanals Hv1, der durch Depolarisation aktiviert wird und die Protonen aus der Zelle ausstößt. Bemerkenswert ist, dass die Protonen durch die Spannungssensordomäne von drHCNL1 geleitet werden, während die Porendomäne nicht funktionsfähig ist. Entscheidend für diesen Protonen-Permeationsweg ist ein Methionin-Rest, der die Sequenz der regelmäßig angeordneten Arginin-Reste im S4-Spannungssensor unterbricht. DrHCNL1 bildet ein Tetramer und enthält somit vier Protonenporen. Im Gegensatz zu den klassischen HCN-Kanälen wird drHCNL1 nicht durch zyklische Nukleotide angesteuert. Ein weiterer, zuvor von Sylvia Fechner identifizierter Ionenkanal im Zebrafischsperma, drCNGK, ist ebenfalls unempfindlich gegenüber zyklischen Nukleotiden und wird stattdessen durch den intrazellulären pH-Wert gesteuert. Meine Ergebnisse deuten darauf hin, dass beide Kanäle eine enge funktionelle Beziehung haben und dass Protonen statt zyklischer Nukleotide als

zelluläre Botenstoffe in Zebrafischspermien dienen. Eine Hauptfunktion der HCN-Kanäle ist die Depolarisation der Zelle nach der Hyperpolarisation. In Süßwasser, das einen extrem niedrigem  $\text{Na}^+$ -Gehalt hat, würde ein  $\text{Na}^+$ -leitender Kanal die Spermien nur weiter hyperpolarisieren. Durch kleine Modifikationen in zwei wichtigen funktionellen Domänen hat sich drHCNL1 in einen selektiven Protonenkanal verwandelt und damit evolutionär an die Süßwasserumgebung angepasst, so dass die Fähigkeit der Spermien zur Depolarisation erhalten bleibt.

# Preface

---

Part of the results of this thesis were already published in:

Wobig L, Wolfenstetter T, Fechner S, Bönigk W, Körschen HG, Jikeli JF, et al. A family of hyperpolarization-activated channels selective for protons. Proc Natl Acad Sci. 2020

May 28

# Contents

---

List of abbreviations .....	IV
1 Introduction .....	1
1.1 Zebrafish fertilization .....	1
1.2 Molecular players of zebrafish sperm physiology .....	2
1.3 HCN channels .....	4
1.3.1 The voltage-sensing domain .....	5
1.3.2 The pore domain .....	8
1.3.3 The cyclic-nucleotide binding domain .....	9
1.4 Aim of this study .....	10
1.5 Data from previous work and collaborators .....	11
2 Materials and Methods .....	12
2.1 <i>Escherichia coli</i> cell culture .....	12
2.1.1 Bacterial strains and vectors .....	12
2.1.2 <i>E. coli</i> culture media .....	14
2.1.3 Culture of <i>E. coli</i> for plasmid preparation .....	15
2.2 Molecular genetics .....	15
2.2.1 Preparation of plasmid DNA .....	15
2.2.2 Purification of DNA .....	16
2.2.3 Quantification of nucleic acids .....	17
2.2.4 Separation of nucleic acids by agarose gel electrophoresis .....	17
2.2.5 Restriction digest of DNA .....	18
2.2.6 Ligation of DNA fragments .....	19
2.2.7 Transformation of <i>E. coli</i> .....	19
2.2.8 Polymerase chain reaction (PCR) .....	20
2.2.9 Site-directed mutagenesis .....	22

## Contents

2.2.10	<i>In vitro</i> transcription .....	24
2.3	Mammalian cell culture.....	25
2.3.1	Media and conditions for mammalian cell culture .....	25
2.3.2	Heterologous expression in mammalian cells.....	26
2.3.3	Generation of a stable Cherry-CAAX CHO cell line .....	28
2.4	<i>Danio rerio</i> .....	30
2.4.1	Heterologous expression in <i>X. laevis</i> oocytes.....	30
2.4.2	<i>D. rerio</i> husbandry .....	30
2.4.3	Preparation of <i>D. rerio</i> tissue.....	30
2.5	<i>Xenopus laevis</i> oocytes .....	31
2.5.1	<i>X. laevis</i> husbandry and harvesting of oocytes .....	31
2.6	Protein biochemistry.....	32
2.6.1	Protein purification.....	32
2.6.2	Protein quantification.....	35
2.6.3	Separation of proteins using gel electrophoresis .....	36
2.6.4	Western blot analysis.....	38
2.7	Immunocytochemistry.....	40
2.7.1	Fixation of CHO cells.....	40
2.7.2	Preparation and fixation of membrane sheets .....	41
2.7.3	Fixation of <i>D. rerio</i> sperm .....	42
2.7.4	Immunocytochemical staining .....	43
2.8	Electrophysiology.....	44
2.8.1	Theoretical principles .....	44
2.8.2	Experimental setups .....	51
2.8.3	Electrophysiological measurements of mammalian cells .....	53
2.8.4	Electrophysiological measurements of <i>D. rerio</i> sperm .....	56
2.8.5	Combined pH-fluorometry and voltage clamp measurements .....	57

2.8.6	Electrophysiological measurements of <i>X. laevis</i> oocytes .....	59
2.8.7	The liquid-junction potential.....	61
2.9	pH-fluorometry of <i>D. rerio</i> sperm.....	61
2.9.1	Single-cell pH-fluorometry.....	61
2.9.2	pH-fluorometry in the stopped-flow apparatus .....	62
3	Results.....	63
3.1	The HCNL protein family.....	64
3.2	Activation of drHCNL1.....	67
3.3	Selectivity of drHCNL1 for protons .....	71
3.3.1	DrHCNL1 conducts protons .....	71
3.3.2	Quantification of the proton selectivity of drHCNL1 .....	77
3.4	Permeation pathway in drHCNL1 .....	82
3.4.1	Sequence comparison of HCNL1 and classical HCN channels .....	82
3.4.2	Blockers of VSD and PD .....	85
3.4.3	Truncation and mutation of the PD .....	88
3.4.4	Mutation of M169 in the S4 motif of the VSD .....	90
3.5	Heterologous expression of drHCNL2 .....	94
3.6	DrHNCL1 in zebrafish sperm .....	96
3.6.1	Electrophysiological recording from <i>D. rerio</i> sperm .....	96
3.6.2	Detection of drHCNL1 in <i>D. rerio</i> tissue.....	98
3.6.3	pH-fluorometry in <i>D. rerio</i> sperm.....	101
4	Discussion .....	104
5	References .....	114
6	Appendix.....	128

# List of abbreviations

---

°C	Degrees Celsius
A. bidest.	Double-distilled water
ATP	Adenosine triphosphate
BCA	Bicinchoninic acid
BCECF	2',7'-bis-(2-carboxyethyl)-5-(and-6)-carboxyfluorescein
<i>C. auratus</i>	<i>Carassius auratus</i>
<i>C. carpio</i>	<i>Cyprinus carpio</i>
cAMP	Cyclic adenosine monophosphate
CatSper	Cation channel of sperm
cGMP	Cyclic guanosine monophosphate
CHO cells	Chinese hamster ovarian cells
CNBD	Cyclic nucleotide-binding domain
CNG channel	Cyclic nucleotide-gated channel
CNGK channel	K <sup>+</sup> -selective cyclic nucleotide-gated channel
<i>D. rerio</i>	<i>Danio rerio</i>
Di-8-ANEPPS	4-(2-[6-(Diocetylamino)-2-naphthalenyl]ethenyl)-1-(3-sulfopropyl)pyridinium inner salt
DTT	Dithiothreitol
DNA	Deoxyribonucleic acid
DNase	Deoxyribonuclease
dNTP	Desoxy-nucleoside triphosphate
E	Potential
e <sub>0</sub>	Elementary charge (e <sub>0</sub> = 1.602176634×10 <sup>-19</sup> C)
<i>E. coli</i>	<i>Escherichia coli</i>
EDTA	Ethylenediaminetetraacetic acid
ES	Extracellular solution
FCS	Fetal calf serum
GC	Guanylate cyclase
GFP	Green fluorescent protein
GHK equation	Goldman-Hodgkin-Katz equation
GTC	gating-charge transfer-center
HA-tag	Human influenza hemagglutinin-tag
HCN channel	Hyperpolarization-activated cyclic nucleotide-gated channel
HCNL	HCN-like channel

HCS	Hydrophobic constriction site
HEK cells	Human embryonic kidney cells
I	Current
I <sub>f</sub>	Funny current
I <sub>h</sub>	Hyperpolarization-activated current
IS	Intracellular solution
K <sub>v</sub> channel	Voltage-gated K <sup>+</sup> -channel
LB-medium	Lysogeny broth medium
M	Molar
min	Minutes
ml	Milliliter
mRNA	Messenger RNA
P	Permeability
PBS	Phosphate-buffered saline
PCR	Polymerase chain reaction
PD	Pore domain
PVDF	Polyvinylidene fluoride
Q	Charge
RNA	Ribonucleic acid
RNase	Ribonucleas
RT	Room temperature
s	Slope
<i>S. anshuiensis</i>	<i>Synocyclocheilus anshuiensis</i>
s.d.	Standard deviation
<i>S. purpuratus</i>	<i>Strongylocentrotus purpuratus</i>
sNHE	Sperm-specific Na <sup>+</sup> /H <sup>+</sup> -exchanger
SDS	Sodium dodecyl sulfate
SDS-PAGE	Sodium dodecyl sulfate polyacrylamide gel electrophoresis
T	Temperature
t	Time
TAE buffer	Tris acetate EDTA buffer
TE buffer	Tris EDTA buffer
U	Enzyme unit
UV	Ultraviolet
V	Voltage
VSD	Voltage-sensing domain
<i>X. laevis</i>	<i>Xenopus laevis</i>



# 1 Introduction

---

Fertilization is the first step in the genesis of a new organism via sexual reproduction. The success of fertilization hinges on the sperm cell finding and entering the egg cell. The process is best understood in mammals, where the sperm are released into the female reproductive tract (internal fertilization), and in marine invertebrates, where both sperm and eggs are released into the surrounding sea water (external fertilization) (1). However, not much is known about the sperm physiology of freshwater fish, many of which are external fertilizers. Their gametes face an entirely different environment and are confronted with low osmolarity and very low concentrations of almost all common ions (2). In recent decades, the zebrafish has become a popular model organism due the relative ease with which genetically-modified lines can be created (3). Their investigation could provide exciting new insights into how sperm function in the unique freshwater environment.

## 1.1 Zebrafish fertilization

Zebrafish are freshwater fish and external fertilizers meaning they release both gametes in the freshwater environment (2). Upon release, the drop in osmolarity activates motility and starts the fertilization process (4). However, the low osmolarity also continuously damages the sperm (2,5). The hostile freshwater environment has led to a number of interesting adaptations which causes the fertilization process to strongly differ from that of marine external fertilizers (i.e. the sea urchin) or that of internal fertilizers (i.e. humans) (2).

The egg is surrounded with a dense protective protein layer called the chorion. Because zebrafish sperm lack an acrosome or other means to penetrate the chorion, it contains a small opening: the micropyle (6). Sperm not only have to find the egg and the precise location of the micropyle but also pass through it. In order to avoid excessive damage caused by low osmolarity, the sperm must complete this task as quickly as possible (2,5); zebrafish sperm are only motile for about one minute after activation by the spawning medium (7). But the time window for fertilization is not only limited by the sperm, but

also by the egg: after fertilization, the eggs of many teleost fish undergo a process known as activation, in which the chorion hardens and separates from the egg itself (2,8). Whereas in some species, this process is triggered by fusion of a sperm cell with the egg, in zebrafish and other *Cyprinids* it is independent of insemination and triggered by the exposure to the spawning medium itself (spontaneous activation) after a short delay (30 s). About 30 s after the onset of activation, cortical granules are released from the egg which alter the chorion and the micropyle and, thereby, prevent fertilization thereafter (9,10). Due to these factors, fertilization needs to occur within one minute or less.

During the mating process, female and male pair up and release their gametes simultaneously (2,11). Fertilization occurs in less than one minute during the period where sperm are motile and before egg activation prevents fertilization. This also ensures that the eggs will not be inseminated by a male other than the original mate of the female (2).

How exactly the sperm finds the egg and enters the micropyle in this short period of time is largely unknown. Whereas sea urchin sperm locate the egg by following a chemoattractant gradient over long distances (sperm are attracted to the egg at a distance of approximately 0.5 mm, which is 100 times the total length of the sperm)(12), there is no evidence of chemotaxis in fish sperm (13). Several species (e.g. herring *Clupea pallasii*, rainbow trout *Oncorhynchus mykiss* and barfin flounder *Verasper moseri*) possess proteins bound to the egg surface that are crucial for guiding the sperm to the micropyle: when eggs or chorions are treated with proteases, sperm are no longer able to locate the micropyle effectively (14,15). However, this mechanism is not universal: in goldfish (*Carassius auratus*), trypsin treatment had no effect on fertilization rates (14).

### **1.2 Molecular players of zebrafish sperm physiology**

The chemotactic signaling cascade of sea urchin sperm is probably one of the best described signaling cascade (Figure 1-1) (1,16). Sperm locate the egg by following a gradient of chemoattractant. The chemoattractant binds to a receptor guanylate cyclase (GC), which synthesizes cGMP that, in turn, activates a K<sup>+</sup>-selective cyclic nucleotide-

gated (CNGK) channel. Opening of CNGK causes hyperpolarization, which activates two proteins: a voltage-gated  $\text{Na}^+/\text{H}^+$ -exchanger (sNHE) that causes the sperm to alkalize, and a hyperpolarization-activated, cyclic-nucleotide gated (HCN) channel that causes sperm to depolarize. Both of these effects lead to the activation of the sperm-specific  $\text{Ca}^{2+}$  channel CatSper: alkalization shifts the voltage-dependence of CatSper to more negative values such that the depolarization by HCN is sufficient for activation.  $\text{Ca}^{2+}$  influx through CatSper modulates the swimming behavior that steers sperm towards the egg (1,16,17).

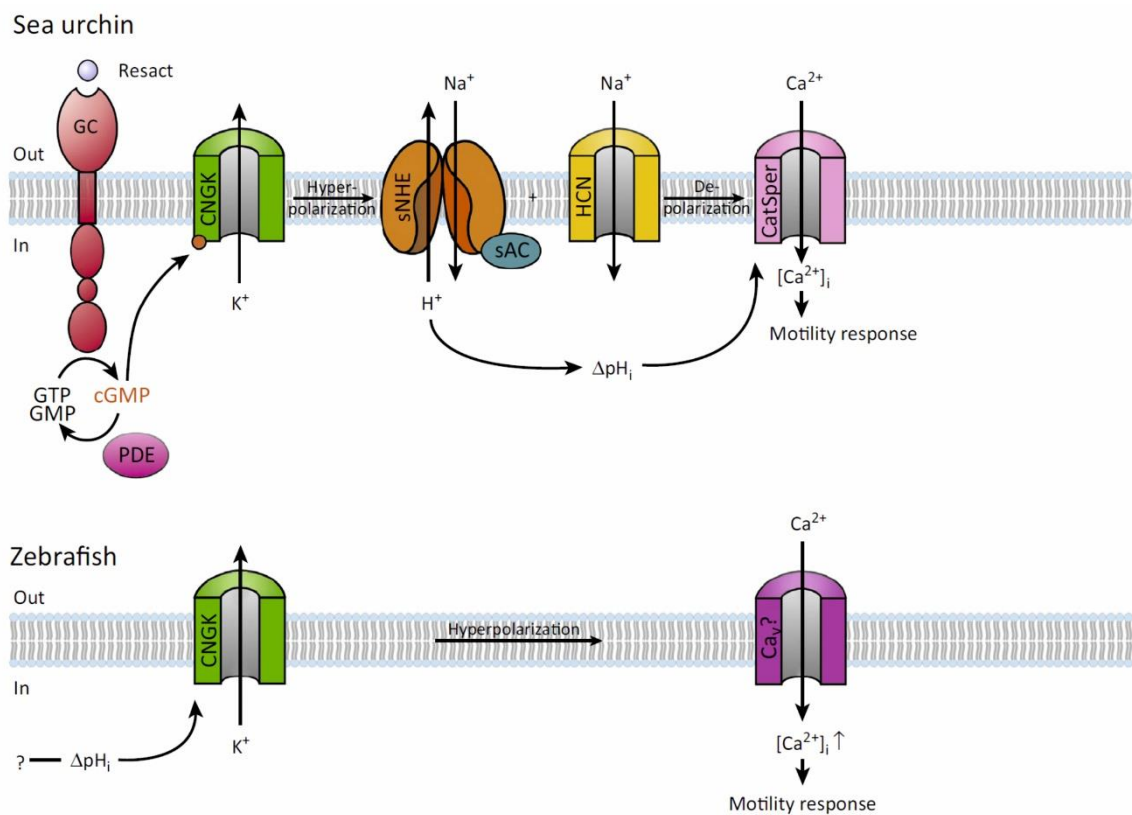


**Figure 1-1: Comparison of the signaling cascade of sea urchin sperm and zebrafish sperm.** Modified from (16).

On the other hand, the signaling pathway of zebrafish sperm is largely unknown (Figure 1-1). In 2012, Fechner et al. identified a CNGK channel in zebrafish sperm (drCNGK) that is activated by intracellular alkalization (18,19). In a freshwater environment, opening of drCNGK would cause  $\text{K}^+$  to flow out of sperm and cause hyperpolarization. Fechner et al. could also show that an increase of intracellular  $\text{Ca}^{2+}$

caused a change in the swimming behavior of zebrafish sperm (18,19). Together with the fact that  $\text{Ca}^{2+}$  plays a central role in sperm motility in most species, it seems plausible that zebrafish sperm also possess a voltage-gated  $\text{Ca}^{2+}$  channel similar to CatSper, even though no such channel has been identified, yet. After drCNGK, a protein resembling another component of the signaling cascade of sea urchin sperm - the HCN channel - was identified in zebrafish sperm.

### 1.3 HCN channels

Hyperpolarization-activated, cyclic-nucleotide gated (HCN) channels are probably best known as “pacemaker channels” because they control spontaneous rhythmicity in the sinoatrial node of the heart and in certain neurons of the brain (20–24). The hyperpolarization following an action potential opens HCN channels that carry an inward  $\text{Na}^+$  current and subsequently depolarize the cell until the threshold for the next action potential is reached (25–27). This current through HCN channels is referred to as hyperpolarization-activated current ( $I_h$ ), pacemaker current, or - because current activation at such a negative membrane voltage is so unusual - funny current ( $I_f$ ) (20–23,28). Cyclic nucleotides can bind to HCN channels and modulate their voltage-dependence and activation kinetics. For example, in the sinoatrial node, intracellular cAMP levels determine how fast  $I_h$  depolarizes the cell and thus how quickly the next action potential is triggered, which causes the heart rate to increase or decrease (23,24,29). HCN channels were first discovered in heart, brain and sperm (30–32) but have since been found in variety of cells and tissues (28).

Like most voltage-gated ion channels, HCN channels contain four subunits that assemble into a tetramer (24,26,28). Each subunit consists of six transmembrane segments (S1-S6) that form two functional domains: the voltage-sensing domain (VSD, in S1-S4) that allows the channel to change conformation in response to the membrane voltage and the pore domain (PD, assembled from S5 and S6 with a pore loop between the two helices) through which ions permeate the channel. Additionally, HCN channel subunits possess a C-terminal cyclic-nucleotide binding domain (CNBD) that conveys conformational changes to the pore domain when cyclic nucleotides bind (24,26,28).

In the next section, I will describe each functional domain in more detail to give the reader an overview of the properties of HCN channels and their underlying molecular mechanisms.

### 1.3.1 The voltage-sensing domain

The voltage-sensing domain (VSD) of HCN channels is overall similar to those of other voltage-gated ion channels. Most strikingly, they all feature a sequence of regularly spaced, basic amino-acid residues (Arg and Lys) in S4 separated by two hydrophobic residues (RXXR) (24,28,33). These basic amino acids carry a partially positive charge. When the membrane voltage changes, these charges move in the electrical field of the membrane and thus the protein undergoes a conformational change that opens or closes the channel gate (see Chapter 1.3.2). As the charged amino acids of many VSDs move through the electrical field of the membrane, they generate a small current: the so-called gating current (33,34).

Gating currents can be directly measured when ionic currents and other capacitive currents that occur when the membrane capacitance is charged during voltage changes are eliminated (34). For a more detailed description of the methodology of gating current measurements, see Chapter 2.8.3.1. Because there is only a fixed number of charged amino acids in S4 that can move over a limited distance (i.e. the thickness of the membrane), gating currents have a number of unique characteristics that distinguish them from ionic currents:

- 1) *Gating currents are transient.* When the membrane voltage is changed, the gating charges will move to a different location in the membrane (33,34). For example, when the membrane voltage is hyperpolarized, the charges in S4 of an HCN channel will move toward the intracellular side of the membrane (the convention is to refer to a motion towards the intracellular side of the membrane as a downward motion). This motion produces a transient current that ceases once all the charges have reached their new positions (Figure 1-2a) (34,35).

## 1 Introduction

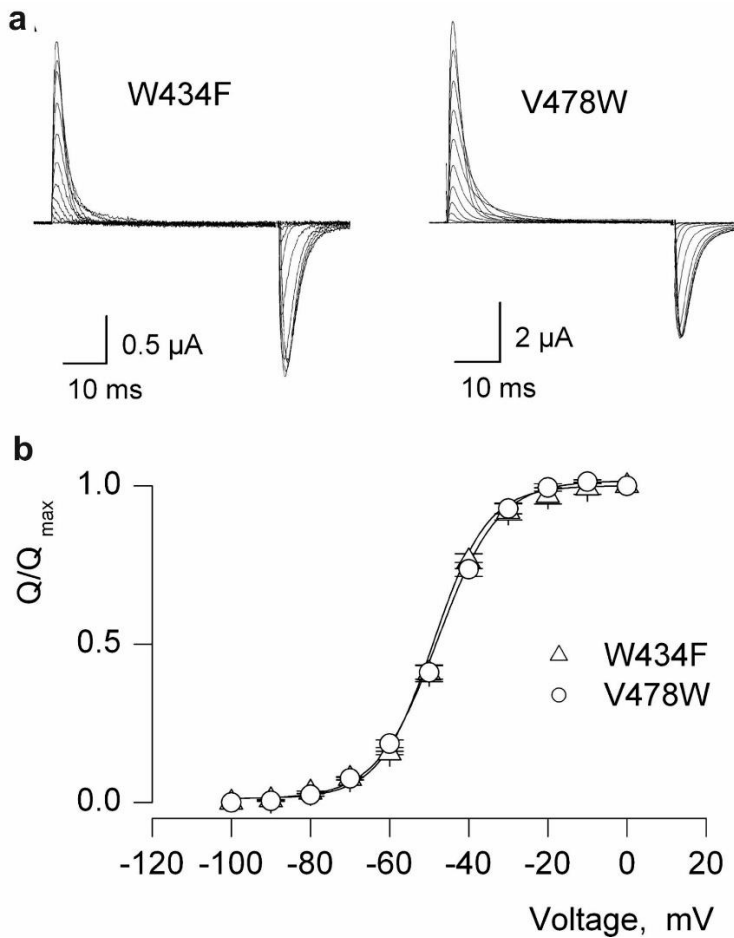


**Figure 1-2: Gating currents in *Shaker*.** **a**, Recordings of gating currents in two non-conducting mutants of the *Shaker*  $K^+$  channel. **b**, Charge-voltage ( $Q/V$ ) plot of the *Shaker* mutants pictured above. Modified from (36).

- 2) *Gating charges saturate.* When the voltage is changed in incremental steps, gating currents will increase as more charges are moved farther across the membrane. However, at some voltage all gating charges have been moved to their new positions. Increasing the voltage even further will result in the gating charges assuming their final position faster (i.e. gating currents will rise and decay faster) but the number of charges that have moved will remain constant. When plotting the total charges moved (which is the area under the curve of the gating current) against the voltage ( $Q/V$  plot), the resulting curve will have a sigmoid shape (Figure 1-2b)(34).

- 3) *Gating currents have two components.* The gating current transient that results from a channel's VSD moving in response to an activating voltage step is referred to as the *on* current. When the activating voltage step ceases, the gating charges will move back to their previous, non-activated positions, which elicits a second gating current transient, called the *off* current (Figure 1-2a). *On* and *off* currents can have different kinetics, but the total number of *on* and *off* charges will always be the same, as both currents represent the movement of the same charges between the same two positions (34). However, for some channels, a phenomenon called “voltage-sensor immobilization” has been described: after prolonged activation, the VSD enters a stable conformation from which it recovers only slowly (34,37–39). Because this process happens over a prolonged time period (relative to the standard gating current), it results in a very small current that is difficult to detect. Due to voltage-sensor immobilization, *off* currents appear smaller than *on* currents when the channel is activated for long times, but will be more similar for short activation periods (34).
- 4) *Gating currents have a defined direction.* For hyperpolarization-activated channels like HCN channels, the *on* current will be negative (as positive gating charges move downward) and the *off* current positive (as they move upward to return to their initial positions). The situation is reversed in depolarization-activated channels (e.g. the voltage-gated K<sup>+</sup> channel *Shaker*) (Figure 1-2a) (34).

How exactly does S4 move during voltage sensing? By examining gating currents of *Shaker* in membrane patches where the number of channels is known, it was found that each channel contained 13 elementary charges ( $e_0$ ) as gating charges or  $3.25 e_0$  for each subunit (40). Evidently, even though each subunit possesses 7 positively charged amino acids, only some cross the electrical field of the membrane and some only partially. However, this does not mean that these charges need to cross the entire width of the membrane ( $\sim 30 \text{ \AA}$ ). Instead, the electrical field is focused over just a small distance (3–4  $\text{\AA}$ ) due to the specific structure of the VSD: its shape resembles an hourglass with aqueous clefts above and below a central hydrophobic constriction site (HCS) formed by hydrophobic residues from S1-S3, and over which most of the electrical field drops (41–44). During the voltage-sensing motion, the charged amino acids in S4 pass

through this site one by one; therefore, this part is also referred to as the gating-charge transfer-center (GTC) (45).

The fact that the hyperpolarization-activated HCN channels possess the same VSD as depolarization-activated ion channels had confounded researchers for some time. Why does the downward movement of S4 lead to opening of the pore in some channels but to the closing in others? Although this question has not been definitively answered, new evidence provided some insight: In hyperpolarization-activated channels, it seems likely that instead of stabilizing the open state of the pore - as it is the case in depolarization-activated channels - the depolarized position of the VSD stabilizes the closed position. Here, S4 and S5 interact closely and are positioned in a manner to “compress” the pore (46–48). Upon hyperpolarization, S4 moves downwards  $\sim 10$  Å and incurs a  $\sim 80^\circ$  bend at the lower half of the helix moving almost parallel to the membrane (47,48). Because of its strong interaction with S4, S5 moves and “splays from the central pore in an iris-like motion” (48). The central pore is no longer constricted and can open. It appears that the breakpoint in S4 that allows for the  $\sim 80^\circ$  bend is critical for hyperpolarization-activated opening of the pore: depolarization-activated channels exhibit no break in S4 in the hyperpolarized conformation, and preventing the S4 break by amino-acid substitution in HCN channels reverses the sign of activation (from hyperpolarization- to depolarization-activated) (48).

### 1.3.2 The pore domain

Like voltage-gated  $K^+$  ( $K_v$ ) channels, HCN channels have a highly-conserved pore loop between S5 and S6 (24,26,28). In HCN channels, the sequence CIGYG (in  $K_v$  channels TVGYG) forms the selectivity filter with the GYG motif being especially crucial: channels where this motif is disrupted in just one subunit are non-conducting (49,50). High-resolution structures have revealed that the selectivity filter forms the narrowest part with a wider external opening and an internal water-filled vestibule. The carbonyl groups of the peptide backbone of the selectivity filter form binding sites for  $K^+$ , and, to pass this narrow constriction,  $K^+$  ions are stripped of their hydration shell and are hopping along these binding sites (46,51). This mechanism endows  $K_v$  channels with a very high  $K^+$  selectivity (permeability ratio  $P_{K^+}:P_{Na^+} = 1,000 - 10,000$ )(51,52). Despite

the highly similar amino-acid sequence of their selectivity filters, HCN channels are only weakly selective for  $K^+$  compared to classical  $K_v$  channels ( $P_{K^+}:P_{Na^+} = \sim 4$ ) (28,30,31). Surprisingly, structural studies revealed that HCN channels carry only two binding sites for  $K^+$  in the selectivity filter, whereas  $K_v$  channels contain four (46). Four binding sites allow the binding of two  $K^+$  at a time, which conveys high selectivity: although the ion-binding site is strongly favoring  $K^+$ , a  $Na^+$  can bind briefly and then rapidly exit to either side; however, when the neighboring binding site is occupied by a  $K^+$  ion, a  $Na^+$  ion's path through the selectivity filter is blocked and it must exit to the same side it entered (53). Because HCN channels can bind only one  $K^+$  ion at a time,  $Na^+$  can occasionally permeate the selectivity filter (46,53). For HCN channels, this poor ion selectivity is a critical prerequisite to depolarize the cell upon hyperpolarization, because at these potentials, most of the inward current is carried by  $Na^+$  (28).

### **1.3.3 The cyclic-nucleotide binding domain**

Lastly, HCN channels possess a C-terminal cyclic-nucleotide binding-domain (CNDB) that, upon cyclic nucleotide binding modulates the channel kinetics and voltage dependence (24,28). The CNBD of HCN channels can bind both cAMP and cGMP; even though cGMP is a full agonist of HCN (shift in  $V_{1/2}$  is in the same range than that caused by cAMP), it is much less potent than cAMP (30). However, being different from CNG channels, binding of cyclic nucleotides is not a prerequisite for opening of HCN channels (54). Instead, the generally accepted model is that, in the absence of cyclic nucleotides, the CNBD partially inhibits the channel. This inhibition is relieved upon binding of cAMP (55).

## 1.4 Aim of this study

In contrast to our extensive knowledge about the physiology of sperm in marine invertebrates and in some mammals (such as humans and mice), very little is known about sperm of freshwater fish. Their sperm face a vastly different environment than sperm of marine external fertilizers and internal fertilizers. Surprisingly, we find orthologues of components of the signaling cascade in sea urchin sperm in zebrafish. The  $K^+$ -selective cyclic nucleotide-gated channel (CNGK) channel of zebrafish (drCNGK) has been characterized previously by Sylvia Fechner; she could show several functional differences between drCNGK and sea urchin CNGK (18). Zebrafish sperm also contain a channel that resembles HCN channels (termed “drHCNL1” for “HCN-like channel 1”). I started to characterize this channel during my master thesis (56) and also identified some striking differences: I could demonstrate that drHCNL1 was a hyperpolarization-activated, highly-selective proton channel, and I provided some preliminary evidence suggesting that protons are conducted via the voltage-sensing domain (VSD) of the channel and not via its pore domain (56). During my PhD thesis, I wanted to support and expand these findings with additional experimental evidence. My main goals are the following:

- Gather additional evidence to delineate the permeation pathway by site-directed mutagenesis and pharmacological methods.
- Characterize a different HCNL channel in zebrafish, drHCNL2, by heterologous expression.
- Explore the physiological role of drHCNL1 in zebrafish sperm.

## 1.5 Data from previous work and collaborators

This PhD thesis is heavily based on the results of my master thesis (56). To provide context and clarify the motivation behind several experiment, findings from my master will be cited frequently and several figures from my master thesis are reproduced in this thesis. During my PhD thesis, several data sets obtained during my master thesis were expanded and re-analyzed. Figures including these data sets are labeled with “Parts of this data set were already published in (56).”

The characterization of HCNL was a project involving a lot of collaboration in our lab. Sylvia Fechner had already performed some experiments with drHCNL1 and some her data sets were expanded during my PhD thesis. Then, Thérèse Wolfenstetter and I worked on the project as PhD students in parallel, with our supervisors Thomas Berger and Reinhard Seifert contributing to the lab work as well. Whereas Thérèse focused on the *Xenopus laevis* oocyte expression system, I mainly worked with mammalian cells. We approached the project with these two expression systems at the same time because frequently some ion channel constructs are expressed better in one system than the other (or are not expressed in one system at all). Additionally, the different expression systems make a wider range of experiments available.

Due to this collaborative nature, many of my experiments were informed by the findings of the other people working on the project. There are also several findings that were not obtained by me personally, but that I felt important to include in order to provide a full picture. Therefore, these findings will be cited frequently and occasionally figures will be reproduced for added clarity. The respective references are either Thérèse Wolfenstetter’s PhD thesis (57) or our lab’s joint publication (58) and figures are labeled with “This data set was obtained by...” or “Parts of this data set were obtained by...”.

## 2 Materials and Methods

---

### 2.1 *Escherichia coli* cell culture

The descriptions for methods concerning *E. coli* cell culture were mainly taken from (18) and partially modified.

#### 2.1.1 Bacterial strains and vectors

For amplification of plasmid DNA the *E. coli* strain K-12 XL1-Blue (Stratagene, La Jolla, USA) was used (genotype: *recA1*, *endA1*, *gyrA96*, *thi-1*, *hsd-R17* ( $r_{K^-}$ ,  $m_{K^+}$ ), *supE44*, *relA1*, *lac* [ $F'$ *proAB*, *lacI $\phi$ Z $\Delta$ M15*, Tn10( $Tet^r$ ).]) Table 2-1 shows the plasmid vectors used in this thesis. Table 2-1: Plasmid vectors

Vector	Source	Description
pBluescript	Stratagene (La Jolla, USA)	Cloning of recombinant DNA
pcDNA3.1(+)	Life Technologies (Carlsbad, USA)	Expression of protein in mammalian cells
pc3QBI-Citrin/ pc3QBI-Cherry- CAAX	W. Bönigk	Modified version of pcDNA3.1(+) where the neomycin gene is replaced by a Citrine or mCherry-CAAX fluorescent protein preceded by a QBI SP163 enhancer sequence; used to allow identification of transfected cells by their fluorescence
pcDNA1.1/Amp	Life Technologies (Carlsbad, USA)	Expression of protein in mammalian cells (only used for certain constructs where, when pcDNA3.1(+) was used, plasmid amplification was impaired)
pGEMHE	Liman et al., 1992 (59)	<i>In vitro</i> transcription (Chapter 2.2.10)

Most of the DNA constructs used in this thesis were prepared by W. Bönigk (Forschungszentrum Caesar). All DNA constructs used in this thesis are listed in Table 2-2. All constructs contained an N-terminal HA-tag with the exception of constructs

with an N-terminal GFP. Identical constructs that exist both in the pcDNA3.1(+) and the pGEMHE vector share the same abbreviation throughout the thesis. Depending on the respective application (expression in mammalian cells or *in vitro* transcription) the corresponding construct was used.

**Table 2-2: DNA constructs**

<b>Vector</b>	<b>Construct</b>	<b>Abbreviation</b>
pcDNA3.1(+)	pc3-DrHCNlike1pA	drHCNL1
pcDNA3.1(+)	pc3-DrHCNlike2	drHCNL2
pcDNA3.1(+)	pcDNA3.1-drHCNL1-M169R	drHCNL1-M169R
pcDNA3.1(+)	pcDNA3.1-drHCNL1-M169C	drHCNL1-M169C
pcDNA3.1(+)	pcDNA3.1-drHCNL1-Δ(R208-S308)	drHCNL1-Δ(R208-S308)
pcDNA3.1(+)	pcDNA3.1-drHCNL1-Δ(K204-S308)	drHCNL1-Δ(K204-S308)
pcDNA3.1(+)	pcDNA3.1-drHCNL1-Δ(R208-S504)	drHCNL1-Δ(R208-S504)
pcDNA3.1(+)	pcDNA3.1-drHCNL1-Δ(S196-S504)	drHCNL1-Δ(S196-S504)
pcDNA3.1(+)	pcDNA3.1-drHCNL1-Δ(S251-S504)	drHCNL1-Δ(S251-S504)
pcDNA3.1(+)	pcDNA3.1-hHv1 (by David Fußh�ller)	hHv1
pcDNA3.1(+)	pc3-mHCN2	mHCN2
pcDNA1.1/Amp	pcA-HCNL1VSD-SpIhPD-HCNL1CNBD-GFP	drHCNL1-SpIH-PD
pcDNA1.1/Amp	pcA-HCNL1VSD-SpIhPore-HCNL1CNBD-GFP	drHCNL1-SpIH-Pore
pcDNA1.1/Amp	pcA-HCNL1VSD-SpIhPoreAYA-HCNL1CNBD-GFP	drHCNL1-SpIH-PoreAYA
pcDNA1.1/Amp	pcA-Cherry	mCherry
pc3QBI-Citrin	pc3QCit-DrHCNlike	drHCNL1+YFP
pc3QBI-Citrin	pc3QCit-drHCNL1-M196R	drHCNL1-M69R+YFP
pGEMHE	pGEMHE-drHCNL1	drHCNL1
pGEMHE	pGEMHE-drHCNL1-M169R	drHCNL1-M169R
pGEMHE	pGEMHE-drHCNL1-M169C	drHCNL1-M169C
pGEMHE	pGEMHE-drHCNL1-F96A	drHCNL1-F96A
pGEMHE	pGEMHE-drHCNL1-Δ(R208-S308)	drHCNL1-Δ(R208-S308)
pGEMHE	pGEMHE-drHCNL1-Δ(K204-S308)	drHCNL1-Δ(K204-S308)
pGEMHE	pGEMHE-drHCNL1-Δ(R208-S504)	drHCNL1-Δ(R208-S504)
pGEMHE	pGEMHE -drHCNL1-Δ(S196-S504)	drHCNL1-Δ(S196-S504)

<b>Vector</b>	<b>Construct</b>	<b>Abbreviation</b>
pGEMHE	pGEMHE-drHCNL1- $\Delta$ (S251-S504)	drHCNL1- $\Delta$ (S251-S504)
pGEMHE	pGEMHE-HCNL1VSD-SpIhPD- HCNL1CNBD-GFP	drHCNL1-SpIH-PD
pGEMHE	pGEMHE-HCNL1VSD-SpIhPore- HCNL1CNBD-GFP	drHCNL1-SpIH-Pore
pGEMHE	pGEMHE-HCNL1VSD-SpIhPoreAYA- HCNL1CNBD-GFP	drHCNL1-SpIH-PoreAYA
pGEMHE	pGEMHE-HCNL1VSD-mIH2PD- HCNL1CNBD-GFP	drHCNL1-HCN2-PD
pGEMHE	pGEMHE-HCNL1VSD-mIH2Pore- HCNL1CNBD-GFP	drHCNL1-HCN2-Pore
pGEMHE	pGEMHE-HCNL1VSD-mIH2PoreAYA- HCNL1CNBD-GFP	drHCNL1-HCN2-PoreAYA

### 2.1.2 *E. coli* culture media

For cultivation of *E. coli* standard LB-medium (Carl-Roth, Karlsruhe) was used (Table 2-3).

**Table 2-3: LB-medium**

tryptone	10 g/l
yeast extract	5 g/l
NaCl	5 g/l
pH	7.0 $\pm$ 0.2

For the preparation of agar plates 15 g/l agar (Sigma, Steinheim) was added to the medium. The liquid media were autoclaved in bottles or flasks (20 min, 121 °C) and then stored at RT. Agar-containing media were first autoclaved and then poured into sterile Petri dishes (25-30 ml per plate). If necessary, ampicillin (final concentration: 100  $\mu$ g/ $\mu$ l) was added to agar with a maximum temperature of 60 °C shortly before the plates were poured. After curing the plates were stored at 4 °C.

### 2.1.3 Culture of *E. coli* for plasmid preparation

*E. coli* cells of a bacterial colony or a preculture were incubated for at least 8 h in LB-medium at 37 °C in a rotary incubator (New Brunswick Scientific, Edison, USA) or in a shaker incubator (Infors HT, Bottmingen-Basel). To select the cells that had taken up plasmids, ampicillin was added to the medium (Chapter 2.1.3).

## 2.2 Molecular genetics

The descriptions for methods concerning molecular genetics were mainly taken from (18) and partially modified.

### 2.2.1 Preparation of plasmid DNA

The DNA was usually eluted in double-distilled water (A. bidest.). In some cases, TE buffer was used (Table 2-4).

**Table 2-4: TE buffer**

Tris/HCl (pH 8.0)	10 mM
EDTA	0.1 mM

#### 2.2.1.1 Mini-preparation by alkaline lysis

Mini-preparation of plasmid DNA was carried out according to a modified protocol based on the work of Birnboim and Doly (60), using alkaline cell lysis. The bacteria were pelleted from 1.5 ml of an overnight culture by centrifugation (1 min, 20,000 g, 4 °C) and resuspended in 50 µl solution I (Table 2-5) by vortexing. Addition of 60 µl solution II (Table 2-5) and careful mixing (inverting) causes the cells to lyse. To precipitate cell debris, proteins and chromosomal DNA, 75 µl solution III (Table 2-5) are added, carefully mixed by inverting and centrifuged at 20,000 g.5-7 min at 4 °C. The supernatant was removed and the containing plasmid DNA precipitated by addition of 550 µl ice-cold 100% (v/v) ethanol. The precipitation was carried out either for 2-3 min at RT or for 20 min at -20 °C. The precipitate was then centrifuged (2-3 min, 20,000 g, 4 °C), the pellet washed in 500 µl ice-cold 70% (v/v) ethanol and centrifuged again for

2-3 min (20,000 g, 4 °C). The pellet was dried in the heating block at 37 °C for 10 min and then resuspended with 20 µl A. bidest.

**Table 2-5: Solutions for mini-preparation**

solution I		solution II		solution III	
Tris/HCl (pH 7.5)	25 mM	NaOH	0.2 M	KAc (pH 4.8)	3 M
EDTA	0.1 mM	SDS	1% (w/v)		

#### 2.2.1.2 Plasmid preparation using the NucleoSpin Plasmid Kit and the NucleoBond XtraMidi Kit

To increase the yield and purity of DNA preparations for transfection of mammalian cells (Chapter 2.4.2), the NucleoSpin Plasmid Kit from Macherey & Nagel (Düren) was used. Bacterial cells from 1.5 ml of an overnight culture were lysed using alkaline lysis according to the manufacturer's instructions. The lysate was then purified via an anion exchange column. The plasmid DNA was eluted with 20 – 50 µl A. bidest.

To prepare larger amounts of DNA, a midi preparation was performed using the NucleoBond Xtra Midi Kit from Macherey & Nagel. Bacterial cells from 50 ml of an overnight culture were pelleted for 10 min at 5,000 g and 4 °C and also lysed using alkaline lysis according to the manufacturer's instructions. The resulting DNA pellet was dried for 15 min at RT and resuspended in 50 – 200 µl A. bidest.

### 2.2.2 Purification of DNA

#### 2.2.2.1 Ethanol precipitation

To concentrate the DNA or exchange buffer, the DNA can be precipitated from a saline solution by adding alcohol. The DNA solution was adjusted to a sodium acetate concentration of 0.3 M (pH 4.8) and mixed with 3 times the volume of ethanol. The DNA was then pelletized by centrifugation (15-60 min, 17,000 g, 4 °C). The DNA pellet was finally washed with 70% (v/v) ethanol and resuspended in the desired buffer (or water) after drying.

#### 2.2.2.2 Purification using the “SureClean Kit”

The DNA solution was mixed with the same volume of “SureClean” reagent (Bioline, Taunton, USA), centrifuged and pelleted according to the manufacturer's instructions and finally washed with 70% (v/v) ethanol. The pellet was resuspended in A. bidest. after drying.

#### 2.2.3 Quantification of nucleic acids

The concentration of nucleic acids was determined using the Nanodrop ND-1000 (NanoDrop Products, Wilmington, USA). The device only requires a small sample volume (2  $\mu$ l) and has a wide detection range (2 ng/ $\mu$ l - 3,7  $\mu$ g/ $\mu$ l for double-stranded DNA). In the “Nucleic Acid” mode, the device measures the absorption of the sample at 230, 260 and 280 nm. Nucleotides, RNA, single-stranded DNA (ssDNA) and double-stranded DNA (dsDNA) all have their absorption maximum near 260 nm. The absorption of the sample at 260 nm is proportional to the concentration of nucleic acid in the sample and is calculated by the device using Beer's Law. Absorption at 280 nm indicates a contamination with phenols and proteins, whereas absorption at 230 nm indicates a contamination with other organic substances. As a measure of purity of the sample, the device calculates the ratios of sample absorbance at 260 nm and 280 or 230 nm respectively (“260/280” and “260/230”). A sample can be considered pure when the “260/280” ratio is  $\sim$ 1.8 for DNA or  $\sim$ 2.0 for RNA and the “260/230” ratio is  $\sim$ 2.0-2.2, whereas appreciably lower ratios indicate a contaminated sample.

#### 2.2.4 Separation of nucleic acids by agarose gel electrophoresis

With agarose gel electrophoresis nucleic acids can be separated by size for analytical and preparative purposes. 1% agarose gels were used for separations in the 500-10,000 bp range. The agarose was boiled in 1x TAE buffer (Table 2-6) until it was completely dissolved. After the gel solution had cooled to below 60 °C, it was mixed with 1  $\mu$ g ethidium bromide per ml agarose solution and poured into a gel carrier with a sample comb. The samples were mixed with a 10x loading buffer (

## 2 Materials and Methods

Table 2-7) and carefully pipetted into the sample pockets of the gel. Electrophoresis was performed in 1x TAE as a running buffer at a constant voltage of 120 V for 20 min. The nucleic acids were then examined under UV light.

**Table 2-6: 50x TAE buffer**

Tris/acetate (pH 7.5)	2 M
EDTA	50 mM

**Table 2-7: 10x loading buffer**

10x TAE buffer	
glycerol	50% (v/v)
xylene cyanol	0.25% (v/v)

### 2.2.4.1 Elution of DNA fragments from agarose gels

The Nucleo Spin Extract II kit (Macherey & Nagel) was used for elution from agarose gels. The DNA band was cut out of the gel and eluted from the agarose according to the manufacturer's instructions.

### 2.2.5 Restriction digest of DNA

To cut DNA with restriction endonucleases, the preparations were incubated in reaction buffers of the respective manufacturer (Ambion (Austin, USA), MBI Fermentas (Vilnius, Litauen) or New England Biolabs (Frankfurt am Main)) at the optimum temperature (usually 37 °C) for the respective enzyme. Incubation with several enzymes was performed simultaneously under identical buffer conditions. If this was not possible, the DNA was precipitated between reactions by ethanol precipitation (Chapter 2.2.2.1) or the restriction fragment was eluted from a preparative agarose gel. Restriction analyses were performed in a volume of 10 µl and, unless otherwise stated, after incubation for 2-4 h applied completely to an agarose gel. The volume for preparative preparations was 10-50 µl. After the complete restriction, the preparation was applied to an agarose gel and eluted for further use (Chapter 2.2.4).

### 2.2.6 Ligation of DNA fragments

Ligation was performed by mixing approximately 50 ng of cut vector with a 3-5-fold molar excess of DNA fragment and 10x ligase reaction buffer (Table 2-8). A total volume of 10  $\mu$ l was ligated with 0.5  $\mu$ l of a T4 DNA ligase (New England Biolabs) for at least 60 min at RT.

**Table 2-8: 10x ligase reaction buffer**

Tris/HCl (pH 7.5)	500 mM
MgCl <sub>2</sub>	100 mM
DTT	100 mM
ATP	10 mM

### 2.2.7 Transformation of *E. coli*

For the transformation of competent XL1-Blue *E. coli*, 5  $\mu$ l of the ligation reaction (Chapter 2.2.6) were used. 50  $\mu$ l competent cells (Chapter 2.1.1) were thawed on ice and added to the DNA, cautiously mixed and kept on ice for 20 minutes. After a short heat shock at 42 °C (60 s) and another 10 min on ice, 200  $\mu$ l of preheated LB-medium were added. The bacteria were incubated for 20-30 min at 37 °C and then ~150  $\mu$ l were plated with a Drigalski spatula on LB agar (0), and incubated overnight at 37 °C. To amplify already purified plasmid DNA (Chapter 2.2.1, 2.2.2), a so-called “re-transformation” can be performed. For this purpose 1  $\mu$ l plasmid DNA can be transformed as described above.

### **2.2.8 Polymerase chain reaction (PCR)**

DNA fragments can be amplified using the polymerase chain reaction (PCR). In several cycles, the matrix DNA is heat denatured, hybridized with suitable oligonucleotides ("primers") and extended with the aid of a heat-stable polymerase. Throughout this process, sequence between the two primers is repeatedly reproduced (61). The PCR fragment can be cloned into a vector via restriction interfaces (Chapter 2.2.5, 2.2.6).

All PCRs were carried out in a thermocycler (Perkin Elmer, Waltham, USA). The standard temperature step protocol is listed in

Table 2-9. The annealing temperature was selected based on the two primers' melting temperature ( $T_m$ ). It was calculated according to the following formula, where  $n_{G/C}$  stands for the number of guanine and cytosine bases and  $n_{A/T}$  for the number of adenine and thymine bases.

$$T_m = n_{G/C} \times 4^\circ\text{C} + n_{A/T} \times 2^\circ\text{C}$$

The annealing temperature was selected to be 4 °C below the  $T_m$  of the primer with the lower  $T_m$ . The duration of the elongation period was based on the length of the fragment to be amplified, where approx. 20 s were set per 1,000 bp. After the PCR protocol finished, the samples were kept 8 °C by the thermocycler until they were removed for further use or storage. The polymerase used was the "KOD Hot Start DNA Polymerase" (Novagen, Billerica, USA) with the buffer supplied by the manufacturer. The PCR reactions were prepared in a volume of 25-50  $\mu\text{l}$ . The composition for a standard 50  $\mu\text{l}$  PCR reaction is given in Table 2-10.

PCR products were either used immediately or cleaned by ethanol precipitation (Chapter 2.2.2.1) with the "SureClean Kit" (Chapter 2.2.2.2). If unwanted by-products were present or the PCR product was to be sub-cloned into a vector, the desired fragment was eluted from an agarose gel (Chapter 2.2.4.1).

**Table 2-9: Temperature protocol for PCR**

Phase	Temperature (°C)	Duration (min)	Cycles
initial denaturation	94	2:00	1x
denaturation	94	0:30	38x
annealing	50-65	0:30	38x
elongation	68	0:20 – 2:00	38x
final elongation	68	2:00	1x

**Table 2-10: Composition of PCR reaction mix**

template DNA	1-10 ng
forward/reverse primer	75 ng each
10x PCR buffer	5 µl
dNTP mix (2 mM)	5 µl
MgSO <sub>4</sub> (25 mM)	2 µl
polymerase	1 U
A. bidest	ad 50 µl

### 2.2.9 Site-directed mutagenesis

Point mutations of drHCNL1 were generated by site-directed mutagenesis using mismatch primers. In this approach, primers are used that don't match the template exactly but contain a slightly altered codon for the amino acid that is exchanged. The newly synthesized DNA will contain the altered codon. Here, the “QuikChange Site-Directed Mutagenesis Kit” by Stratagene was used. The annealing temperature was based on the melting temperature of the primers which was calculated with following formula (where “% GC” stands for the percentage of bases that are guanine or cytosine, “N” stands for the primer length in bases and “% mismatch” stands for the percentage of bases that are mismatched):

$$T_m = 81.5 + 0.41 (\% GC) - \left( \frac{675}{N} \right) - (\% mismatch)$$

The standard temperature protocol is given in Table 2-11.

The composition of the PCR reaction mix was the same as for the standard PCR (Chapter 2.2.8) except that 5 – 50 ng of template DNA were used. The primers used for each construct are listed in Table 2-12.

After the PCR reaction, 1.5  $\mu$ l of DpnI (New England Biolabs) was added to the samples. DpnI cuts only methylated DNA and thereby degrades the template DNA. The resulting DNA could then immediately be used for transformation (Chapter 2.2.7).

**Table 2-11: Temperature protocol for site-directed mutagenesis PCR**

Phase	Temperature (°C)	Duration (min)	Cycles
initial denaturation	95	3:20	1x
denaturation	95	1:00	26x
annealing	51-55	1:00	26x
elongation	72	1:30-2:00	26x
final elongation	72	10:00	1x

**Table 2-12: Primer for site-directed mutagenesis**

Mutant	Reading direction	Sequence (5' – 3')
drHCNL1-M169R	forward	GTCCGAATTCTGAGGTTTCGCGCGCTTC
	reverse	GAAGCGCGCGAACCTCAGAATTCGGAC
drHCNL1-M169C	forward	GTCCGAATTCTGTGCTTCGCGCGCTTC
	reverse	GAAGCGCGCGAAGCACAGAATTCGGAC
drHCNL1-F96A	forward	CTCTGACATATTAGCTTGCCTGGACATC
	reverse	GATGTCCAGGCAAGCTAATATGTCAGAG

### 2.2.10 *In vitro* transcription

In *in vitro* transcription, DNA is transcribed into mRNA. All solutions for RNA work were prepared with RNase-free H<sub>2</sub>O. First, the plasmids were linearized with NheI for 1.5 h at 37 °C. The linearized DNA was purified the NucleoSpin Gel and PCR Clean-up Kit (Macherey & Nagel). Residual ethanol was removed from the elution volume by centrifugation in a vacuum-concentrator centrifuge for 5-10 min (Univapo 150H, Uniequip, Planegg, Germany). The linearized DNA was then transcribed into mRNA using the “T7 mMESSAGE mMACHINEKit” (Thermo Fischer Scientific, Waltham, USA). After the reaction, the sample was mixed with 1 µl TURBO DNase (1 U/µl) (15 min, 37 °C) to remove the linearized DNA. To remove excess nucleotides and purify the RNA, LiCl precipitation was performed. 30 µl of 7.5 M LiCl and 30µl of A. bidest. were added to each sample. The reaction was incubated overnight at -20 °C and then centrifuged (45 min, 18,000 g, 4 °C). After a wash with 70% ethanol it was centrifuged again (30 min, 18,000 g, 4 °C). The pellet was resuspended in 25 µl A. bidest. The final concentration of the sample was determined with the Nanodrop (2.2.3) and the quality was assessed using an agarose gel (2.2.4).

## 2.3 Mammalian cell culture

The descriptions for methods concerning mammalian cell culture were mainly taken from (18) and partially modified. For heterologous expression, either HEK (human embryonic kidney) 293 cells or CHO (Chinese hamster ovary) K1 cells were used. HEK293 cells were sourced from Life Technologies and CHO cells from ECACC.

### 2.3.1 Media and conditions for mammalian cell culture

HEK293 cells were cultured in DH10 medium (Invitrogen) with 10% FCS (Biochrome, Berlin) at 37 °C, 7.5% CO<sub>2</sub> and approx. 95% humidity in cell culture dishes (Ø 9 cm). The generation time of the cells was about 24 hours. CHO K1 cells were cultured in the same manner, but were kept in F12 medium (Invitrogen) with 10 % FCS at 5% CO<sub>2</sub>. For electrophysiology and immunocytochemistry, a CHO cell line stably expressing drHCN1 (“CHO drHCN1 #E6D5”, generated by H. G. Körschen, research center caesar) was used. For plasma membrane sheets, a CHO cell line stably expressing a membrane-anchored mCherry (“CHO Cherry-CAAX”, generated during this thesis (Chapter 2.3.3)). Both stable cell lines were kept in medium with 400 µg/ml G418 added. Cells were grown to approx. 70% confluency before splitting. After washing with 10 ml of sterile PBS, the cells were detached 1 ml 0.05% trypsin EDTA (Life Technologies) for 2-3 min at 37 °C on a heating plate (Präzitherm; Harry Gestigkeit, Düsseldorf). The cells were then resuspended in 10 ml medium. If necessary, the cell density was determined in a Neubauer counting chamber. HEK cells were either split 1:8 or 1:16 for incubation for 3 or 4 days respectively, or seeded  $1 \times 10^6$  or  $5 \times 10^5$ . CHO cells either split 1:32 or 1:64 for incubation for 3 or 4 days respectively, or seeded  $3 \times 10^5$  or  $1.5 \times 10^5$ . After 30-40 passages the cells were discarded and a new aliquot of frozen cells was used.

### 2.3.1.1 Cryo-conservation of cells

For cryopreservation, cells were harvested that were in the logarithmic growth phase (60-70% confluence). The cells were detached as described above (Chapter 2.3.1) and then pelleted for 5 min at 200 g and resuspended in cryo-medium (growth medium with 10% DMSO). 1 ml aliquots with approx.  $2 \times 10^6$  cells/ml were transferred into cryotubes (Nunc A/S, Thermo Scientific, Waltham, USA). Freezing was performed at -80 °C in an isopropanol-filled cryo-container (“Mr. Frosty” Freezing Container, Nalgene, Thermo Scientific, Waltham, USA); the cryo-container ensures that the temperature is gradually reduced by 1 °C per minute which prevents damage to the cells. To return the cells to culture, the cells were defrosted in a water bath at 37 °C. The cells were carefully resuspended in approx. 20 ml culture medium (37 °C) and centrifuged for 5 min at 200 g twice to eliminate any cytotoxic DMSO from the medium. Afterwards, two plates were seeded with one third and two thirds of the cells each.

### 2.3.2 Heterologous expression in mammalian cells

#### 2.3.2.1 Transfection using Lipofectamine 2000

The transfection using Lipofectamine 2000 (Life Technologies) was most commonly used method for transfection in this thesis. Here, the Lipofectamine 2000 reagent forms liposome complexes with the DNA. These liposomes consist of cationic and neutral lipids that bind the anionic backbone of the DNA. The liposome/DNA complex can fuse with the cell membrane and thereby enter into cell (62).

For transfection with Lipofectamine 2000, the cells were seeded to be approx. 80% confluent on the day of transfection. For each transfection reaction, the respective amount of DNA and Lipofectamine 2000 were both diluted in Opti-MEM (Life Technologies), separately. These pre-dilutions were then combined and incubated for 20 min at RT: The volumes for different cell culture dishes are summarized in Table 2-13. In the meantime, the culture medium was removed from the cells, washed briefly in PBS and then covered in OptiMEM (Table 2-13 for volumes). After 20 min the

transfection batch was applied to the cells and incubated for 4 – 6 h at 37 °C and 5% CO<sub>2</sub>. After this time, the medium was aspirated and the cells cultivated in their respective culture medium. If higher expression levels were required, Na<sup>+</sup> butyrate (final concentration: 5 mM) was added to the culture medium for 8 – 24h. Occasionally, the transfection efficiency of certain constructs was poor (<30% transfected cells); in these cases, the standard composition (as stated in Table 2-13) was optimized in 4-well plates by varying the amount of DNA (0.4 – 2 µg) and the ratio of Lipofectamine to DNA (1:0.5 – 1:5).

**Table 2-13: Composition of a standard Lipofectamine 2000 transfection reaction**

	<b>4-well/24-well</b>	<b>9 cm dish</b>
<b>DNA dilution</b>	0.8 µg in 50 µl Opti-MEM	24 µg in 1.5 ml Opti-MEM
<b>Lipofectamine 2000 dilution</b>	2 µl in 50 µl Opti-MEM	60 µl in 1.5 ml Opti-MEM
<b>Opti-MEM added to cells</b>	400 µl Opti-MEM	12 ml Opti-MEM

### 2.3.2.2 Transfection using electroporation

Transfection using electroporation was used to transfect large numbers of cells (mostly for preparation of protein for proteinbiochemistry, Chapter 2.6). In this method very strong voltage pulses are applied to a cell suspension containing the DNA construct to be transfected. The voltage pulses introduce small pores in the cell membrane and allow the DNA to enter the cells (63,64).

CHO cells were harvested and counted as described in 2.3.1. The cells were resuspended in PBS with a final concentration of  $5 \times 10^6$  cells/ml. For each transfection reaction 125 µl of this cell suspension were pelleted (5 min, 200 g) and resuspended in 125 µl “buffer R” (Invitrogen). 2 µg of DNA were added and this transfection reaction was aspirated in a special gold tip (100 µl Invitrogen) of the microporator (Digital Bio Neon Transfection System, Thermo Fischer Scientific, Waltham, USA). The tip was placed into the electroporation chamber, which was filled with “buffer E2” (Invitrogen). Electroporation was performed by application of three voltage pulses of 1245 V for 0.1 ms each. The cells were then seeded onto 5 cm or 9 cm plates in F12 medium.

### 2.3.2.3 Transfection using PEI

Transfection using polyethylenimine (PEI) was used in some cases when transfection efficiency using Lipofectamine 2000 was poor (<30% transfected cells). PEI is a cationic polymer that forms complexes with DNA. These positively-charged PEI:DNA complexes are endocytosed by the cells which allows the DNA to enter the cytoplasm (65,66).

For transfection with PEI, the cells were seeded to be approx. 80% confluent on the day of transfection. For each transfection reaction, the appropriate amount of DNA was diluted in Opti-MEM (see Table 2-14 for volumes). Afterwards the appropriate amount of PEI (Sigma) was added from a 1 $\mu$ g/ $\mu$ l stock solution. The transfection reaction was incubated at RT for 10 min. In the meantime, the culture medium was removed from the cells and replaced with “starvation medium” (containing only 2% FCS). Afterwards, the DNA:PEI mixture was added to the medium and cells were incubated under normal cell culture conditions overnight. Finally, the medium was again replaced with regular culture medium.

As the transfection efficiency using PEI varied greatly between different DNA constructs, a previous optimization was necessary for each construct. This was done in a 24-well format for 0.4 – 2  $\mu$ g of DNA and DNA:PEI ratios of 1:1 – 1:10.

**Table 2-14: Volumes for PEI transfection**

	<b>4-well/24-well</b>	<b>9 cm dish</b>
<b>Final volume of DNA:PEI mix</b>	50 $\mu$ l	1.5 ml
<b>Starvation medium added to cells</b>	300 $\mu$ l	5 ml

### 2.3.3 **Generation of a stable Cherry-CAAX CHO cell line**

For the preparation of membrane sheets a monoclonal CHO cell line was generated, that stably expressed a membrane-anchored mCherry (“CHO Cherry-CAAX”). For this purpose a mCherry was used which has a C-terminal CAAX-motif. The CAAX-motif consists of a cysteine (“C”) followed by two aliphatic amino acids (“A”) and any

amino acids (“X”) in the fourth position. The presence of a CAAX-motif leads to the modification of the protein with a farnesyl moiety – a form of prenylation. The addition of lipid moiety to the protein causes it to accumulate in the cell membrane (instead of the cytosol) (67,68).

CHO K1 cells were transfected with mCherry-CAAX in 9 cm dish using Lipofectamine 2000. 24 h after transfection 600µg/ml G418 were added to culture medium. G418 is an aminoglycoside antibiotic that blocks protein biosynthesis in both pro- and eukaryotic cells (69). Even though mammalian cells are normally sensitive to G418, the introduction of a neomycin-resistance gene can render the cells resistant the antibiotic (70). The neomycin-resistance gene is included in the pcDNA3.1 vector and ensures that only transfected cells survive the treatment with G418. The expression of mCherry was monitored by examining the cells under a fluorescence microscope and G418 treatment was continued until only cells expressing mCherry remained. To select a single clone with favorable expression levels and growth behavior, the cells were detached and seeded to 96-well plates at concentration of 0.3 cells/well. This ensured that in each well no more than one cell (or none at all) was seeded. As cell growth is considerably slowed at these low densities, the cells were cultured in “conditioned medium” that contained growth factors that are usually excreted by neighboring cells. To obtain “conditioned medium” 9 cm dishes were seeded with cells at approx. 25% confluency and incubated under normal conditions. After 24 h (when cells had reached approx. 50-60% confluency), the medium was aspirated and centrifuged at 10,000 g for 10 min to remove any cells and debris. The supernatant was then frozen at -20 °C until use. The 96-well plates were monitored and wells that contained one colony based from a single cell were marked. Several of these colonies that displayed both high expression (based on their fluorescence) and a reasonably fast generation time (approx. 24 h) were detached and grown to higher densities (approx. 70% confluency) in increasingly large culture dishes. To continually select for transfected cells, the culture medium contained 400 µg/ml G418. After two 9 cm dishes had reached a confluency of approx. 70%, cryo-stocks of four lines were generated (Chapter 2.3.1.1). During this thesis, only the line with the clone number “#C4” was used.

## **2.4 *Danio rerio***

### **2.4.1 Heterologous expression in *X. laevis* oocytes**

For heterologous expression, *X. laevis* oocytes were injected with 50 nl mRNA (0.1 - 2.5 µg/µl, Chapter 2.2.10) per oocyte with a nano-injector device (Nanoliter2010, Worts Precision Instruments Europe, Berlin). Injected oocytes were incubated one to five days at 13 – 18 °C. For patch-clamp recordings, the oocyte's vitelline membrane was manually removed with a pair of fine forceps immediately before measurement.

### **2.4.2 *D. rerio* husbandry**

Zebrafish (*D. rerio*, strain: TL/*brass*) were sourced as adult fish from Dr. B. Odermatt (Universität Bonn, Institute for Anatomy) or from Dr. K. Briggman (research center Caesar, Department of Computational Neuroethology) where the fish were bred and raised in automated zebrafish facilities. The fish were then housed in groups of 10 – 60 fish in large tanks (60 l, 28 °C) and fed with standard flake food (Tetramin, Tetra, Melle).

### **2.4.3 Preparation of *D. rerio* tissue**

#### **2.4.3.1 Preparation of *D. rerio* testes**

Male zebrafish were anesthetized with 200 mg/l MS-222 (Sigma-Aldrich, St. Louis, MO) in 20 mM phosphate buffer (pH 7.0) and subsequently killed by decapitation. A ventral incision was performed and the two testis strands were removed with forceps as a whole. For preparation of sperm (Chapter 2.4.3.2) the testes were placed in 100 µl of ES (composition see Table 2-35) and kept on ice. For protein biochemistry (Chapter 2.6.1.4) the testes were placed in a clean Eppendorf tube, frozen immediately in liquid nitrogen and stored at -80 °C.

#### 2.4.3.2 Preparation of *D. rerio* sperm

The whole testes were either gently flicked or triturated with cut-off pipette tip to flush out the sperm. The testes were kept on ice for approx. 15 min after which the supernatant containing the sperm were carefully removed. The sperm were kept on ice. For protein biochemistry (Chapter 2.6.1.3) the sample was pelleted at 20,000 g for 10 min (4 °C), the supernatant removed, the pellet immediately frozen in liquid nitrogen and stored at -80 °C.

#### 2.4.3.3 Preparation of other *D. rerio* tissues

Fish were anesthetized and killed as described in Chapter 2.4.3.1. Organs (ovary, brain and/or eyes) were carefully removed and placed in a clean Eppendorf tube, frozen immediately in liquid nitrogen and stored at -80 °C.

## **2.5 *Xenopus laevis* oocytes**

### **2.5.1 *X. laevis* husbandry and harvesting of oocytes**

The descriptions for methods concerning *X. laevis* husbandry and harvesting of oocytes were mainly taken from (57) and partially modified.

*X. laevis* oocytes were mainly harvested from an in-house frog colony. The female frogs were purchased from Nasco (Fort Atkinson, USA) and housed in a specialized *X. laevis* facility (AquaSchwarz, Göttingen). *X. laevis* oocytes were also purchased from an oocyte delivery service (EcoCyte, Castrop-Rauxel) or were generously donated by Dr. C. Volk (Hochschule Bonn-Rhein-Sieg, Rheinbach).

To harvest fresh oocytes, frogs were anesthetized by a 7-10 min immersion in a 20 mM phosphate buffer (pH 7.0) containing 6 mM MS-222. After ensuring the animal's sedation by testing the toe-pinch reflex, it was placed on MS-222 -soaked paper towels within the surgery dish and its abdomen was incised with a sterile blade. Two to four ovarian folia, each one containing ~200 oocytes, were harvested and placed in a petri dish filled with ND96 (oocyte storage medium, Table 2-15). The abdominal incision

was sutured using resorbable Vicryl thread (Johnson & Johnson, Norderstedt) by separate stitches into the muscle layer and the skin. After awaking from anesthesia, frogs were given three days recovery in an individual tank followed by a minimum of eight weeks recovery in a group tank before the next surgery.

The harvested oocytes were isolated from the connective tissue of the ovarian follicles, first by rough manual tearing with a pair of forceps, and then by a 90 min incubation in ~1.2 mg/ml collagenase (from *Clostridium histolyticum*, Type IA) diluted in Ca<sup>2+</sup>-free ND96 to catalyze the hydrolysis of peptide bonds within collagen proteins. Finally, removal of tissue debris by thorough washing of oocytes served to singularize the cells. Oocytes were then kept in ND96 at 14 °C until used for experiments.

**Table 2-15: Composition of ND96 buffer**

NaCl	96 mM
Na-Pyruvate	2.5 mM
KCl	2 mM
CaCl <sub>2</sub>	1.8 mM
MgCl <sub>2</sub>	1 mM
HEPES	5 mM
Gentamicin	50mg/ml
pH (adjusted with NaOH)	7.5

## 2.6 Protein biochemistry

### 2.6.1 Protein purification

#### 2.6.1.1 Preparation of total protein from CHO and HEK cells

For the preparation of total protein from mammalian cells, cells were detached from 9 cm dishes with a rubber spatula after an incubation for approx. 1 min in 1 ml PBS-EDTA (PBS with 0.05% (w/v) EDTA) and the cells were pelleted for 10 min at 200 g. The pellet was resuspended in hypotonic lysis buffer (approx. 150 µl per 9 cm dish, Table 2-16) containing a protease inhibitor cocktail for mammalian cells and tissues (“mPIC”, Sigma-Aldrich). The low osmolarity of the buffer caused the cells to rupture.

After 5 minutes incubation on ice, the cells were sonified in a cup horn sonifier (Branson Sonifier 450, Branson, Danbury, USA) three times for 30 s at 40% intensity. The protein concentration of the lysate was quantified using the Bradford assay (Chapter 2.6.2.1) to ensure complete lysis. In the case of a very high protein concentration ( $>5\mu\text{g}/\mu\text{l}$ ) additional lysis buffer was added and sonification was repeated until the final protein concentration was  $<5\mu\text{g}/\mu\text{l}$ . Cell debris and nuclei were removed by a centrifugation 500 g for 10 min. The final protein concentration of the sample was quantified using the Bradford assay. The sample was kept on ice and stored at  $-20\text{ }^{\circ}\text{C}$  or  $-80\text{ }^{\circ}\text{C}$  for long-term storage. After defrosting a sample, the sample was briefly sonified to re-homogenize the membrane fraction.

**Table 2-16: Composition of hypotonic lysis buffer**

HEPES pH 7.0	10 mM
EDTA	1 mM
mPIC	0.1% (v/v)

#### 2.6.1.2 Preparation of membrane protein from CHO cells

To prepare membrane protein from CHO cells, a sample of total protein (prepared as described under 2.6.1.1) was centrifuged for 15 min at maximum speed (150,000g,  $4\text{ }^{\circ}\text{C}$ ) in a “TLA55” ultracentrifuge (Beckmann Coulter, Brea, USA). The supernatant – containing cytosolic proteins – was discarded and the pellet was resuspended in lysis buffer (Table 2-16) or PBS<sup>++</sup> (Table 2-17). The final protein concentration of the sample was quantified using either the Bradford assay (Chapter 2.6.2.1) or bicinchoninic acid (Chapter 2.6.2.2). The sample was kept on ice and stored at  $-20\text{ }^{\circ}\text{C}$  or  $-80\text{ }^{\circ}\text{C}$  for long-term storage. After defrosting a sample, the sample was briefly sonified to re-homogenize the membrane fraction.

**Table 2-17. Composition of PBS<sup>++</sup>**

PBS	
EDTA	2 mM
DTT	1 mM
mPIC	0.2% (v/v)

### 2.6.1.3 Preparation of total protein from *D. rerio* sperm

For the preparation of total protein from sperm, a sperm pellet was thawed and resuspended in 100 µl of solubilization buffer (Table 2-18). The sample was sonified as described above (Chapter 2.6.1.1). To solubilize the membrane proteins, 1% (v/v) Triton-X100 was added to the lysate and the sample gently shaken for 1.5 h. The final protein concentration was determined using bicinchoninic acid (Chapter 2.6.2.2).

**Table 2-18: Composition of solubilization buffer**

NaCl	200 mM
HEPES	50 mM
DTT	1 mM
mPIC	0.2% (v/v)

### 2.6.1.4 Preparation of total protein from other *D. rerio* tissues

For the preparation of total protein from other zebrafish tissues, the samples were thawed and homogenized in 200-400 µl of PBS<sup>++</sup> (Table 2-17) by trituration with a 20G followed by a 27 G hypodermic needle (Braun, Melsungen). The homogenized tissue was then sonified and solubilized as described for sperm (Chapter 0). The final protein concentration was determined using bicinchoninic acid (Chapter 2.6.2.2).

### 2.6.1.5 Preparation of membrane protein from *X. laevis* oocytes

For the preparation of membrane protein from *X. laevis* oocytes, 10-20 were mechanically devitellinated using forceps and washed twice with 1 ml PBS. The oocytes were homogenized in 1 ml oocyte lysis buffer (Table 2-19) and sonified as described above (Chapter 2.6.1.4). To remove cell debris, the lysate was centrifuged twice at 300 g for 10 min (4 °C). Finally the membrane fraction was enriched by ultracentrifugation for 60 min at 150,000 g (4 °C). The final protein concentration of the sample was quantified using either the Bradford assay (Chapter 2.6.2.1) or bicinchoninic acid (Chapter 2.6.2.2).

**Table 2-19: Composition of oocyte lysis buffer**

NaCl	150 mM
NaH <sub>2</sub> PO <sub>4</sub>	50 mM
KCl	10 mM
mPIC	1% (v/v)
pH (adjusted with NaOH)	7.2

## 2.6.2 Protein quantification

### 2.6.2.1 Quantification using the Bradford assay

The Bradford protein assay is a colorimetric protein assay based on the dye Coomassie Brilliant Blue G250. The dye stably binds to proteins and when doing so will shift its color from a reddish brown to blue under acidic conditions. This shift to the blue form of the dye can be quantified by measuring the absorbance of the sample at 595 nm (71). During this thesis, a 5× ready-made assay solution (BioRad, Feldkirchen) was used.

### 2.6.2.2 Quantification using bicinchoninic acid

The bicinchoninic acid (BCA) assay is a colorimetric assay in which the sample changes from green to purple in proportion to the amount of protein present. The assay solution contains copper(II) sulfate and BCA and is highly alkaline. When protein is introduced, the peptide bonds reduce Cu<sup>2+</sup> ions to Cu<sup>+</sup> ions. Two molecules of BCA and one Cu<sup>+</sup> ion then form a stable purple-colored complex that can be quantified by measuring the absorbance of the sample at 562 nm (72). During this thesis this assay was performed using the “Pierce BCA Protein Assay Kit” (ThermoFisher Scientific). In a 96-well plate the assay was performed together with a BSA protein standard and the color change was quantified in a plate reader (Packard Instrument Company, Meriden, USA).

### 2.6.3 Separation of proteins using gel electrophoresis

#### 2.6.3.1 Denaturing SDS polyacrylamide gel electrophoresis (SDS-PAGE)

To analyze protein samples, the proteins were separated by size using SDS-PAGE based on Laemmli (73). Here, proteins are denatured in the presence of sodium dodecyl sulfate (SDS). The charged SDS molecules bind to the unfolded protein strands and confer negative charges to the protein that are proportional to the proteins mass. This allows the proteins to be separated in an acrylamide gel-matrix based on their size.

The samples (containing 10 -30 µg of protein) were denatured in SDS sample buffer (Table 2-20) for 5 min at 95 °C before they were loaded onto the gel. As a size standard the “Applichem Prestained Protein Marker VI” (Applichem, Darmstadt) was used. In most cases, gel electrophoresis was performed in a discontinuous gel system with the collection gel containing 5% (v/v) acrylamide and the separating gel 10% (Table 2-21 and Table 2-22). The gels were placed in the running buffer (Table 2-23) and 15 mA of current were applied, which was increased to 25 mA after the sample had traversed the stacking gel. In some cases pre-cast gradient gels featuring a grading of 4-12% acrylamide (“Novex NuPAGE 4-12% Bis-Tris Protein Gel”, Life Technologies) were used. These gels were used with a pre-made MOPS-SDS running buffer supplied by the manufacturer and electrophoresis was performed at 180 V.

**Table 2-20: Composition of 4x SDS sample buffer**

Tris/HCl (pH 6.8)	200 mM
SDS	8% (w/v)
2-mercaptoethanol	4% (v/v)
glycerol	50% (v/v)
bromophenol blue	0.04% (w/v)

**Table 2-21: Composition of stacking gel (5%)**

0.5 M Tris-HCNL (pH 6.8)	0.5 ml
10% (w/v) SDS	20 $\mu$ l
30% (w/w) acrylamide solution	340 $\mu$ l
10% (w/v) ammonium persulfate	40 $\mu$ l
TEMED	1 $\mu$ L
A. bidest.	1.12 ml

**Table 2-22: Composition of separating gel (10%)**

1.5 M Tris-HCNL (pH 8.8)	1.5 ml
10% (w/v) SDS	60 $\mu$ l
30% (w/w) acrylamide solution	2 ml
10% (w/v) ammonium persulfate	40 $\mu$ l
TEMED	1 $\mu$ L
A. bidest.	2.42 ml

**Table 2-23: Composition of 10x SDS running buffer**

Tris	250 mM
glycine	1.92 M
SDS	1% (w/v)

### 2.6.3.2 Coomassie Brilliant Blue staining

To visualize the separated protein bands the gels were stained with dye “Coomassie Brilliant Blue R250) (Serva, Heidelberg). The gels were stained for 1-2 h in Coomassie staining solution (Table 2-24) and then destained in Coomassie de-staining solution (Table 2-25) until the desired staining was achieved. Prior to documentation the gel was washed in water for at least 1 h.

**Table 2-24: Composition of Coomassie staining solution**

Coomassie R250	0.2% (w/v)
acetic acid (96%)	10% (v/v)
ethanol	30% (v/v)

**Table 2-25: Composition of Coomassie de-staining solution**

acetic acid (96%)	5% (v/v)
ethanol	25% (v/v)

### 2.6.4 Western blot analysis

In Western blot analysis, proteins that have been separated by gel electrophoresis are transferred to a membrane. Then the membrane can then be treated with antibodies to immunologically detect specific proteins (74,75).

#### 2.6.4.1 Immobilization of protein on PVDF membranes

After SDS-PAGE (Chapter 2.6.3.1) the proteins were transferred to a polyvinylidene difluoride (PVDF) membrane (Immobilon P, Millipore, Burlington, USA). For self-cast gels semi-dry blotting was performed in the “Maxi Semi-dry Blotter T788.1” (Carl Roth). The PVDF membrane was briefly activated in methanol and then placed in a stack with the gel and Whatman papers soaked in various buffers in the following order (from bottom (anode) to top (cathode)): anode buffer 1, anode buffer 2, membrane, gel, cathode buffer. 2.4 mA/cm<sup>2</sup> were applied for 35-45 min and the success of the transfer was verified by the appearance of the protein marker on the membrane. Additionally, the gel was stained with Coomassie Brilliant Blue (Chapter 2.6.3.2) to verify that all protein had been transferred.

Pre-cast Novex gradient gels were occasionally blotted in the same fashion as described above, but in most cases, blotting was performed with the tank blot method using the “XCell II Blot Module” (Life Technologies) according to the manufacturer’s directions using the pre-made “Novex Tris Glycine Transfer Buffer” (containing 20% methanol).

The blot module was placed in a water-filled chamber that acted as a cooling system. The transfer was performed according to the supplier's directions either with 25 V at RT for 1-2 h or with 12 V at 4° C overnight.

#### 2.6.4.2 Immunostaining of immobilized proteins

The immunological detection of the transferred proteins (2.6.4.1) involved three steps. First, any unspecific binding sites of the membrane were blocked using the ready-made blocking solution “Odyssey Blocking Buffer (PBS)” (LI-COR Biosciences, Lincoln, USA). Second, the membrane was incubated with the primary antibody against the protein of interest. Third and finally, the membrane was incubated with the secondary antibody against the primary antibody that was covalently linked to an infrared fluorescent dye. In this manner, bands containing the protein of interest were fluorescently labeled. All incubation and washing steps after the application of the secondary antibody were carried out in the dark to avoid bleaching. Between these steps, the membrane was washed using PBS supplemented with 0.05% Tween-20 (Sigma, “PBS-T”). All steps were performed under gentle agitation at room temperature. Occasionally, the incubation with primary antibody was carried out overnight at 8 °C. The sequence of work steps are listed in detail in Table 2-26. All the primary and secondary antibodies with their respective dilutions that were used are listed in Table 2-27 and Table 2-28, respectively. All antibody dilutions were prepared with blocking solution. The blots were developed using an “Odyssey Infrared Imaging System” (LI-COR).

**Table 2-26: Steps for immunostaining of immobilized proteins**

<b>Step</b>	<b>Duration</b>
blocking	30 min
primary antibody incubation	60 min
wash	3 × 5 min
secondary antibody incubation	20 min
wash	3 × 5 min

**Table 2-27: Primary antibodies used for immunostaining of immobilized proteins**

<b>Antibody</b>	<b>Species</b>	<b>Manufacturer</b>	<b>Dilution</b>
anti-HA	rat	E. Kremmer (HZ München)	1:10,000
anti-HA	mouse	Sigma	1:5,000
anti HCNL1 (C-terminal)	rat	E. Kremmer (HZ München)	1:10
anti-HCNL1 (N-terminal)	rat	E. Kremmer (HZ München)	1:10
anti- $\beta$ -actin [AC-15]	mouse	Abcam (Cambridge, UK)	1:10,000

**Table 2-28: Secondary antibodies used for immunostaining of immobilized proteins**

<b>Antibody</b>	<b>Species</b>	<b>Manufacturer</b>	<b>Dilution</b>
anti-rat-800	goat	LI-COR	1:20,000
anti-mouse-800	mouse	LI-COR	1:20,000

## 2.7 Immunocytochemistry

In immunocytochemistry, antigen-specific primary antibodies and fluorescently-labeled secondary antibodies (Chapter 2.6.4.2) are used to fluorescently-label specific cells and/or specific parts of cells containing a protein of interest (76). Additionally, 4',6-diamidino-2-phenylindole (DAPI) was used to fluorescently label DNA and thereby stain the nucleus of cells.

### 2.7.1 Fixation of CHO cells

In this thesis, immunocytochemistry was performed on stable cell lines, as well as cells that were transiently transfected (both in a wildtype and a stable cell line background). The cells were seeded on poly-L-lysine (PLL) coated glass coverslips; the charged PLL molecules cause the cells to adhere to the glass by electrostatic interactions. 1.5H glass coverslips with a diameter of 13 mm were placed into the wells of a 24-well plate and incubated with a PLL-solution (0.1 mg/ml in PBS) for 30 min at RT and then washed with PBS. If no transfection was required, the cells were seeded at least 24 h before immunostaining to be approx. 70% confluent. Transfection was performed as

described in 2.3.2 at least 24 h before immunostaining to ensure sufficiently high expression and appropriate cell density.

Prior to immunostaining, the cells needed to be fixed and permeabilized. Fixation denatures proteins in order to prevent their degradation and preserve the cell structure. Permeabilization disrupts the cell membrane and allows antibodies to enter the cell in order to bind and label intracellular structures.

In this thesis, two different fixation reagents were used: paraformaldehyde (PFA) and methanol. In the PFA method, a PFA solution (in PBS) is prepared and heated at 60 °C to degrade the PFA to formaldehyde. Formaldehyde causes cross-linking of the amino groups of proteins which leads to fixation. In this thesis, cells were washed with PBS and fixed with a 4% (w/v) PFA solution for 5 min at RT. Then, the cells were permeabilized with the detergent Triton X-100. Additionally, the permeabilized cells were treated with a protein-rich blocking solution, to block any unspecific binding sites. For this purpose a commercial blocking solution containing mouse immunoglobulins (“Chemiblock II”, Millipore) was used. In this thesis, permeabilization and blocking were performed simultaneously using a 5% (v/v) Chemiblock solution in PBS containing 0.5% (v/v) Triton X-100 (Sigma) (referred to as “CT”).

As the fixation using PFA involves the cross-linking of proteins, some antibodies no longer recognize their respective epitopes; the epitopes become “masked”. This was the case for the monoclonal HCNL1 antibodies (Table 2-31). Therefore, a different fixation method was used for stainings involving these antibodies: methanol fixation. The application of pure methanol will rapidly dehydrate and thereby denature and fix proteins. As methanol will also dissolve cell membranes, an additional permeabilization step is not necessary when using this fixation method. In this thesis, the cells were washed with PBS and fixed using pre-chilled, pure methanol for 5 min at -20 °C.

### **2.7.2 Preparation and fixation of membrane sheets**

To exclusively examine proteins in the plasma membrane of cells, I generated so-called “membrane sheets”. Here, the cells are “unroofed” by a short ultrasound pulse that destroys and removes all parts of the cell with the exception of the basal plasma

membrane that is attached to the glass coverslip (77). For these experiments the stable CHO Cherry-CAAX cell line was used to visualize the membrane sheets. The cells were transfected with the protein of interest as described in Chapter 2.3.2 and cultured for at least 24 h to ensure appropriately high expression and a cell density of approx. 70%. The cells were washed with PBS and placed in ice-cold sonification buffer (Table 2-29). The cells were then positioned 2 mm underneath the probe of rod sonifier (VibraCell VCX 400, Sonics, Newtown, USA) submerged in sonification buffer and one ultrasound pulse of 20 % amplitude and 100 ms duration was applied. The cells were immediately fixed as described under 2.7.1. As the intracellular side of the plasma membrane was already exposed after unroofing, no permeabilization was necessary.

**Table 2-29: Composition of sonification buffer**

potassium glutamate	120 mM
potassium acetate	20 mM
HEPES	10 mM
EGTA	10 Mm
pH (adjusted with KOH)	7.2

### 2.7.3 Fixation of *D. rerio* sperm

In order to allow staining, the sperm needed to be attached to a surface first. 13 mm PLL-coated coverslips in 24-well plates as described in 2.7.1 were used. 5-10  $\mu$ l of sperm solution (preparation described under 2.4.3.2) was added to each well containing 0.5 ml of ES solution (Table 2-35) and incubated for 30 min in order for the sperm to adhere to the coverslips.

Afterwards, the sperm were fixed by addition of 50  $\mu$ l ice-cold methanol and incubation for 5 min at -20 °C. Unspecific binding sites were blocked using 5% Chemiblock solution in PBS (referred to as “CB”).

### 2.7.4 Immunocytochemical staining

Whole CHO cells, membrane sheets and *D. rerio* sperm were all stained using the same procedure. After fixation the samples were blocked and permeabilized if necessary (Chapter 2.7.1, 2.7.2 and 2.7.3). Then the samples were incubated with the specific primary antibody directed against the protein of interest after that with the secondary fluorescently-labeled antibody and DAPI. Between these steps, the samples were washed with PBS. All incubation and washing steps after addition of the secondary antibody were performed in the dark to avoid bleaching. The sequence of work steps are listed in detail in Table 2-30: Occasionally, the incubation with primary antibody was carried out over night at 8 °C All the primary and secondary antibodies with their respective dilutions that were used are listed in Table 2-31 and Table 2-32, respectively. All antibody dilutions of PFA-fixed cells were prepared with CT solution (containing Triton X-100) whereas antibody dilutions for all methanol-fixed cells as well as plasma membrane sheets were prepared with CB solution (without Triton X-100).

After the staining procedure, the samples were briefly washed with A. bidest. and then covered with Aqua Poly/Mount (PolySciences Inc., Warrington, USA) mounting medium. After hardening overnight, the samples were imaged with a confocal laser scanning microscope (Fluoview FV1000, Olympus, Tokyo, Japan).

**Table 2-30: Steps for immunocytochemistry**

<b>Step</b>	<b>Duration</b>
primary antibody incubation	60 min
wash	3 × 1 min
secondary antibody incubation + DAPI (1:10,000)	20 min
wash	3 × 1 min

**Table 2-31: Primary antibodies for immunocytochemistry**

Antibody	Species	Manufacturer	Dilution
anti-HA	rat	E. Kremmer (HZ München)	1:200
anti-HA	mouse	Sigma	1:5,000
anti HCNL1 (C-terminal)	rat	E. Kremmer (HZ München)	1:10
anti-HCNL1 (N-terminal)	rat	E. Kremmer (HZ München)	1:5
anti-RFP	rabbit	Biomol (Hamburg)	1:500

**Table 2-32: Secondary antibodies for immunocytochemistry**

Antibody	Species	Fluorescent dye	Manufacturer	Dilution
anti-rat	donkey	A488	Dianova	1:400
anti-rat	donkey	Cy3	Dianova	1:250
anti-mouse	goat	A488	Life Technologies	1:400
anti-rabbit	donkey	Cy3	Dianova	1:250

## 2.8 Electrophysiology

### 2.8.1 Theoretical principles

#### 2.8.1.1 The patch-clamp technique

The patch-clamp technique is a electrophysiological method, in which a small section of membrane (a *patch*) is electrically isolated and recorded from – instead of recording over the whole cell. Using a glass pipette with a small opening (typically only a few  $\mu\text{m}$  wide) and smooth, fire-polished edges a tight connection between the cell membrane and the pipette is established. This connection can reach an electrical resistance of multiple gigaohms and is therefore called “gigaseal” (78). The recording can be performed in two modes: voltage-clamp and current clamp. In voltage-clamp mode, the voltage is held constant (*clamped*) and any currents over the membrane are recorded. In contrast, in current-clamp mode, the current over the membrane is held constant which allows the measurement of changes in membrane voltage (e.g. action potentials) (79).

The recording of single-channels currents was only made possible by the patch-clamp technique. Within the membrane patch a single ion channel or only few ion channels could be isolated and recorded individually. Additionally the technique allowed the reduction of noise during the recording so that the extremely small currents through individual ion channels with amplitudes of only few picoamperes: a majority of the noise in early attempts of single-channel recordings was due to fluctuations in the leak current, i. e. the current that flows through the gap between pipette and membrane, due to thermal noise. The variance of thermal noise is inversely proportional to the resistance over which the current flows; thus, when a gigaseal with an extremely high resistance is established, the noise in the recording is strongly reduced (80).

Patch-clamp recordings can be performed in various different configurations (Figure 2-1). First, the pipette is pressed against the cell membrane and light suction is applied until the resistance reaches values  $>1 \text{ G}\Omega$ . In this configuration, current can be recorded from the membrane patch while the cell is intact (cell-attached). By quickly pulling the pipette away from the cell, the membrane patch can be ripped out while the gigaseal remains intact resulting in one of the two excised-patch configurations. Here, intracellular side of the patch faces the bath solution, whereas the extracellular side is exposed to the pipette solution (inside-out). Alternatively, when in the cell-attached configuration the membrane patch can be destroyed by application of rapid, strong suction and/or a strong voltage pulse ( $>400 \text{ mV}$ ). Hereby, the experimenter gains electrical access to the inside of the cell. In this configuration, the current is recorded over the whole cell membrane (whole-cell). The solution inside of the cell is replaced with the pipette solution relatively quickly by diffusion. When in the whole-cell configuration, the experimenter can again pull away the pipette ripping out two small pieces of membrane. The membrane will spontaneously close again around the pipette forming a new membrane patch. Here, the extracellular side of the membrane faces the bath solution and the intracellular side the pipette solution (outside-out), which is the second excised-patch configuration.

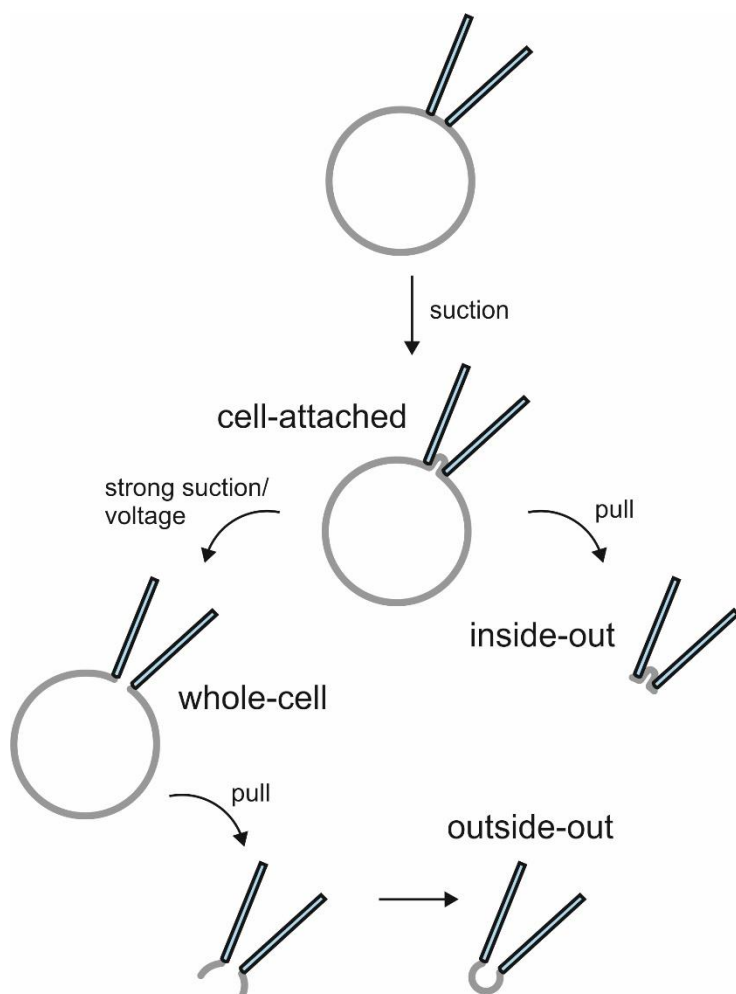


**Figure 2-1: Schematic representation of various patch-clamp configurations.** After the formation of the gigaseal on the cell (cell-attached), the pipette can be pulled away to rip out a membrane patch of which the intracellular side faces the bath solution (inside-out). Alternatively, the membrane patch can be destroyed by strong suction or high voltage to gain electrical access to the inside of the cell (whole-cell). Afterwards, a membrane patch can be excised again where the extracellular side faces the bath solution (outside-out). Modified from (80).

### 2.8.1.2 Series resistance and membrane capacitance compensation

In this thesis, many recordings of CHO cells were performed in the whole-cell configuration (Chapter 2.8.1.1, Figure 2-1). Pipettes with a resistance of 5-10 M $\Omega$  were used. After formation of the gigaseal and access into the cell was established, series resistance and membrane capacitance needed to be compensated to ensure an accurate recording (Figure 2-2).

The series resistance is a sum of the pipette resistance and any additional access resistances at the pipette tip (e.g. residual membrane on the inside of the pipette). In typical whole-cell recordings  $R_s$  was between 7-20 M $\Omega$ . When current flows through  $R_s$  the voltage at the membrane ( $V_m$ ) will not be the same as the desired voltage that is applied at the pipette. This voltage drop is dependent on  $R_s$  and the current over the membrane  $I_m$  in the following manner:

$$V_m = V_p - I_m R_s$$

This error is larger when  $I_m$  or  $R_s$  is large (or both). In addition to steady-state errors, dynamic errors can occur due series resistance and membrane capacitance. When a voltage is applied, the membrane acts as a capacitor which causes a lag. The time constant of this lag can be described by:

$$\tau \approx R_s C_m$$

In this thesis, series resistance and membrane capacitance compensation were performed for all whole-cell recordings (~80-90% correction).

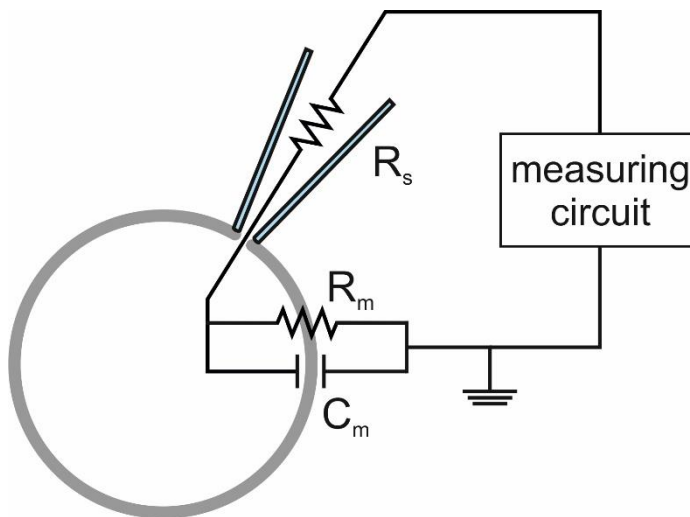


**Figure 2-2: Simplified circuit diagram for the whole-cell configuration.** The cell membrane acts both as a resistor (with resistance  $R_m$ ), through which currents over the membrane ( $I_m$ ) flow, and as a capacitor (with capacitance  $C_m$ ). Additionally, a combination of pipette resistance and access resistance introduce the series resistance  $R_s$ . Modified from (81).

2.8.1.3 The patch-clamp amplifier

In this thesis, all electrophysiological recordings were performed in voltage-clamp mode. Here, the membrane is held at a constant, defined command voltage  $V_C$  and any currents over the membrane are measured (Chapter 2.8.1.1). The patch-clamp amplifier achieves this with a feedback-amplifier that corrects any changes in voltage and a differential amplifier that measures the required currents (Figure 2-3). All of this takes place in a pre-amplifier unit called “headstage”. The first amplifier compares the voltage at the pipette  $V_P$  with the command voltage  $V_C$ . When a current  $I_M$  flows over the membrane,  $V_P$  will gradually deviate from  $V_C$ . Whenever  $V_P$  differs from  $V_C$ , a current is injected over  $R_F$  to compensate this difference. The current that is required to counteract the change in  $V_P$  is exactly the same as  $I_M$  but with the opposite sign. During the recording the amplifier compensates changes in  $V_P$  within microseconds. When current is injected over  $R_F$ , it causes a voltage drop of  $V = R_F \times I$  that is measured by the second amplifier. In the main amplifier unit, this voltage is converted (using the known value for  $R_F$ ) back into a current signal (which corresponds to  $-I_M$ ). The signal is further amplified, filtered and then digitized in an A/D converter. During this thesis data were filtered with 5-10 kHz 4-pole low-pass Bessel filter and digitized with a sampling rate of 10-50 kHz.

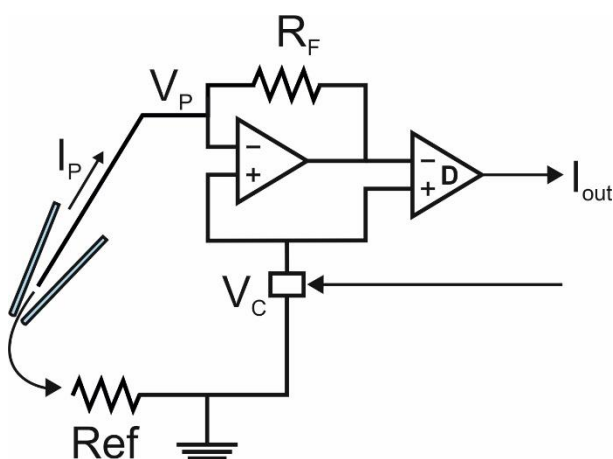


**Figure 2-3: Simplified circuit diagram of a patch-clamp amplifier.** The differential amplifier is labeled “D”. See 2.8.1.3 for a detailed description. Modified from (81).

#### 2.8.1.4 Two-electrode voltage clamp

For measuring currents in whole *X. laevis* oocytes, the two-electrode voltage clamp (TEVC) method was used. The electrodes used for TEVC have a lower resistance (0.3 – 1.5 M $\Omega$ ) and a sharp tip that is directly impaled into the oocyte without forming a seal first. Their higher capacity for passing current allows the measurement of very large currents. Additionally, the use of two electrodes – one for measuring the membrane potential and a second one to inject current to hold the membrane at the desired potential – makes it possible to clamp the voltage even in cells as large as frog oocytes (with a diameter of 1-2 mm). Injecting current at a more distant point on the other side of the cell from where the membrane potential is measured ensures that the potential is adjusted correctly over the entirety of the cell and not just in the proximity of the measuring electrode. During TEVC measurements, the composition of the solution inside of the oocyte is generally not altered as diffusion from the sharp electrodes is only very limited.

A simplified circuit diagram of the TEVC amplifier is shown in Figure 2-4. The voltage electrode  $E_V$  measures the membrane potential ( $V_M$ ) which an operational amplifier compares to a reference bath electrode ( $Ref_V$ ) set to 0 mV. This voltage is recorded and allows the experimenter to monitor  $V_M$  throughout the experiment. The membrane voltage is also compared to the command voltage  $V_C$  at a second operational amplifier. Whenever there is a difference between these two voltages, a current is injected over the current electrode  $E_I$ . The current that is required to counteract a given change in  $V_M$  from  $V_C$  is exactly the same as the current that passed over the membrane ( $I_M$ ) to cause this change in  $V_M$  in the first place but of the opposite sign. Therefore, the voltage drop caused by the current injected at  $E_I$  allows the measurement of  $I_M$  in the same manner as described for the patch-clamp amplifier (Chapter 2.8.1.3).

During this thesis data were filtered with 5 kHz 4-pole low-pass Bessel filter and digitized with a sampling rate of 10 kHz.

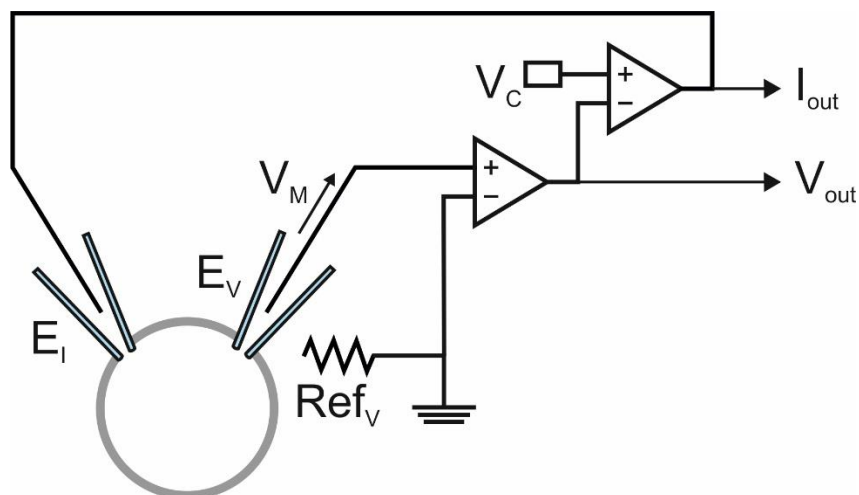


**Figure 2-4: Simplified circuit diagram of a TEVC amplifier.** See 2.8.1.4 for a detailed description. Modified from (82).

#### 2.8.1.5 Voltage and current conventions

Voltages are always given relative to the reference bath electrode to which the potential 0 mV is ascribed. A positive voltage indicates that the interior of the cell is positively charged compared to the bath and a negative voltage a negative interior. A positive current corresponds to a flow of cations over the cell membrane out of the cell whereas a negative current signifies an influx of cations. When observing anions, a positive current indicates an influx of anions and a negative current an outward flow of anions.

## 2.8.2 Experimental setups

### 2.8.2.1 The patch-clamp setup

A standard patch-clamp setup consists of four basic components:

- a stable platform that minimizes mechanical disturbances
- a microscope that allows visual inspection of the sample and the patch pipettes
- a micromanipulator that allows precise movement of the patch pipette and the sample
- electronics for stimulation and recoding

Except for the large electronic equipment (main amplifier unit, digitizer, computer) all components were mounted on an air-cushioned table. The whole table was surrounded by a Faraday cage to shield the recording equipment any external electromagnetic fields. To visualize the sample and patch pipettes, an inverted microscope (either a Zeiss Axiovert 200, Jena or an Olympus IX 71, Tokio, Japan) was used. The sample was placed in a measuring chamber with a glass bottom to allow inspection with the microscope from below. For different applications, different measuring chambers could be used. The measuring chamber was fixed in a self-made object stage that could be positioned freely using a micromanipulator (PatchStar, Scientifica, Uckfield, UK). Using a gravity-driven perfusion system attached to the measuring chamber, the sample could be superfused with different bath solutions. For pharmacology on excised-patches from mammalian cells, a special multi-channel bath chamber was used. Here, instead of exchanging the whole volume of the measuring chamber, the patch pipette can be placed into a different perfusion channel. All patch pipettes were manufactured from borosilicate glass (Hilgenberd, Malsfeld) using a DMZ puller (Zeitz Instruments GmbH, Martinsried). To position the patch pipette, it was first filled with pipette solution and placed in a pipette holder containing a silver chloride wire. In this holder, the pipette could be freely position using a second micromanipulator. The pipette holder was attached to the headstage unit of the patch-clamp amplifier (Axopatch 200B,

Molecular Devices, Sunnyvale, USA). Also connected to the headstage unit was the reference electrode which consisted of a second silver chloride wire that was placed in the bath chamber as well. As large changes in the ionic composition of the bath solution can cause fluctuations in the offset potential at the bath electrode, it was connect via an agar-filled salt bridge containing 3 M KCl solution. The headstage unit was connected to the main amplifier unit. The signal was then digitized with a Digidata 1440A (Molecular Devices) to be recorded on a computer running the pCLAMP 10 (Molecular Devices) software. All electrophysiological recordings were performed at room temperature (approx. 22 °C).

### 2.8.2.2 Fluorescence imaging at the patch-clamp setup

To perform fluorescence imaging at the patch-clamp setup a 75 W xenon lamp (Photon Technology International, PTI, Birmingham, UK) together with a monochromator (DeltaRAM X, PTI, Birmingham, UK) was used. Using the monochromator light of the desired wavelength was selected to excite fluorescence which was fed to microscope via a light guide. Citrine fluorescence was excited with light of a wavelength of 480 nm with a bandwidth of 12.5 nm (480/12.5 nm). Ratiometric excitation of BCECF was performed by alternating excitation light of 440/12.5 nm and 480/12.5 nm at a frequency of 5 Hz. Both for Citrine and BCECF either the filter set “Fs09” (Zeiss) or a custom filter-set for GFP (using Semrock BrightLine filters) was used. Observation of mCherry fluorescence was performed with excitation light of 560/17.5 nm and either the filter set “Fs 31” (Zeiss) or “mCherry-B” (Semrock). For detailed specification of the filter sets see Table 2-33 and Table 2-34. A 60× water objective (Olympus UplanSApo, 60x, 1.20W) was used for all fluorescence imaging.

**Table 2-33: Specifications of Zeiss filter sets**

	<b>Fs 09</b>	<b>Fs 31</b>
excitation filter	bandpass 450-490 nm	bandpass 565/30 nm
dichroic	510 nm	585 nm
emission filter	longpass 515 nm	bandpass 620/60 nm

**Table 2-34: Specifications of Semrock BrightLine filter sets**

	<b>custom GFP</b>	<b>mCherry-B</b>
excitation filter	bandpass 466/40 nm	bandpass 562/40 nm
dichroic	495 nm	593 nm
emission filter	525/50 nm	bandpass 641/75 nm

### 2.8.3 Electrophysiological measurements of mammalian cells

For electrophysiological investigations, the cells were seeded on poly-L-lysine (PLL) coated glass coverslips. The charged PLL molecules cause the cells to adhere to the glass by electrostatic interactions. 1.5H glass coverslips with a diameter of 5 mm were placed into the wells of a 4-well plate and incubated with a PLL-solution (0.1 mg/ml in PBS) for 30 min at RT and washed with PBS. If no transfection was required, the cells were seeded at least 24 h before immunostaining to be approx. 70% confluent. Transfection was performed as described in Chapter 2.3.2 at least 24 h before electrophysiological experiments to ensure sufficiently high expression and appropriate cell density. Occasionally, the cells were treated with 5mM sodium butyrate in normal growth medium at least over night to boost expression of the transfected construct. Whereas the mechanisms underlying this are not entirely known, exposure to sodium butyrate leads to an increase in histone acetylation and changes in the chromatin structure both of which correlate with expression modulation. Sodium butyrate treatment is effective in variety of cell lines (including HEK and CHO cells) and when using a variety of promoters (including CMV promotor that is featured on the pcDNA3.1 vector used in this thesis) (83,84).

For all transient transfections the channel of interest was either transfected on a vector also containing a citrine (pc3QCit) or was co-transfected with citrine or mCherry on a separate vector. The fluorescent protein then functioned as a marker that allowed the identification of successfully transfected. Only fluorescent cells were selected for electrophysiological measurements.

## 2 Materials and Methods

To measure, a glass plate with cells attached was placed in the measuring chamber. After visual inspection, a suitable cell was selected (that showed the appropriate fluorescent marker in case of a transient transfection). Cells were only measured once and a fresh glass plate was used every 15 – 60 minutes. Patch pipettes had an initial resistance of 5-10 M $\Omega$ .

All solutions for mammalian cells featured an osmolarity of approx. 300 mOsmol/kg. Most measurements were performed using solutions mimicking physiological conditions for many mammalian cells (termed “ES” for the extracellular solution and “IS” for the intracellular solutions, see Table 2-35 and Table 2-36). For applications where a lower intracellular buffer concentration was needed (e.g. for measurement of intracellular pH shifts) an IS with a lower amount of buffer (“IS LB”, Table 2-36) was used. For measurements of proton reversal potentials so-called “NMDG-based solutions” were used (Table 2-37). These contain high concentrations of buffer to minimize proton redistribution and feature only large organic cations instead of alkali ions. These solutions have been previously proven in the study of proton-selective channels (85–87). In some cases, solutions containing symmetrical (inside and outside of the cell) sodium and potassium concentrations were used (Table 2-38).

**Table 2-35: Composition of ES solution**

NaCl	140 mM
KCl	5.4 mM
CaCl <sub>2</sub>	1.8 mM
MgCl <sub>2</sub>	1 mM
Glucose	10 mM
HEPES	5 mM
pH (adjusted with NaOH)	7.4

**Table 2-36: Composition of IS/IS-LB solution**

NaCl	14 mM
potassium aspartate (KAsp)	130 mM
EGTA	1 mM
MgATP	2 mM
HEPES	10/1 mM
pH (adjusted with KOH)	7.4

**Table 2-37: Composition of NMDG-based solutions**

NMDG	120 mM
MES/HEPES	100 mM
EGTA	1 mM
TEA-Cl	5 mM
pH (adjusted with MS)	variable

**Table 2-38: Composition of symmetrical NaCl/KCl solution**

NaCl	75 mM
KCl	75 mM
HEPES	5 Mm
EGTA	1 mM
pH (adjusted with NaOH)	7.4

### 2.8.3.1 Measurement of gating currents

In voltage-gated ion channels, charged amino acids in the VSD move according to the membrane voltage allowing the channel to sense membrane voltage (Chapter 1.3.1). As these charges move through the electric field of the membrane they generate a small, transient current (33,34). When these currents were first described in Na<sup>+</sup> channels, they correlated with the opening of the channels and were therefore called gating currents (88).

Due to the fast and transient nature and small size of gating currents they are easily obscured by transient currents that are caused by the membrane capacity  $C_m$  in the

whole-cell conformation (Chapter 2.8.1.2). These currents increase or decrease linearly with the applied voltage over the whole range of voltage that the membrane can tolerate (i.e. their linearity is only limited by membrane breakdown) (34). Gating currents, on the other hand, only occur in response to certain voltage changes where the voltage sensor can move. To subtract the linear, capacitive currents, a preliminary voltage step can be applied where no gating currents occur because the voltage sensor remains in one of its extreme positions. To achieve this, these preliminary pulses are often applied in the opposite direction of the activating voltage pulse. Because the capacitive currents behave linearly, their expected contribution to the total current measured for a voltage step where gating currents do occur can be calculated from the preliminary pulse and then subtracted. This method will also subtract any leak currents that behave in a linear fashion. Usually multiple preliminary voltage steps with only a fraction of the actual voltage pulse are performed that are then added (e.g. 4 preliminary pulses of  $P/4$  mV for a pulse of  $P$  mV) to avoid membrane breakdown and damaging the gigaseal at high voltages (34,89).

For gating current measurements, a  $P/4$  protocol of pulses in the opposite direction was applied using the built-in  $P/4$  correction function of Clampex.

### **2.8.4 Electrophysiological measurements of *D. rerio* sperm**

For electrophysiological measurements, approx. 5  $\mu$ l of the fresh sperm suspension (preparation described in Chapter 2.4.3.2) was added to the well of a 4-well plate containing 0.5 ml of ES (Table 2-35) with multiple uncoated 5 mm coverslips. The sperm was kept undisturbed on ice for at least 15 min to allow the sperm to gently adhere to the coverslips. To measure, a glass plate with sperm cells attached was placed in the measuring chamber. Due to the comparatively high osmolarity of the ES solution, the sperm are immotile. Only sperm that were lightly attached at the head, with the flagellum still moving in the flow of the perfusion or due to positive pressure applied to the patch pipette, were selected for measurement. Gigaseals were formed at the neck region of the sperm. After a stable gigaseal had formed, the sperm was lifted from the coverslip by moving the patch pipette slowly upwards.

Measuring solutions were similar to those used for mammalian cells but contained Cs<sup>+</sup> instead of K<sup>+</sup> to block currents through the CNGK potassium channel (19) and are therefore referred to as “Cs-ES” and “Cs-IS” (Table 2-39 and Table 2-40). Patch pipettes had an initial resistance of 7-12 M $\Omega$ .

**Table 2-39: Composition of Cs-ES**

NaCl	140 mM
CsCl	5.4 mM
CaCl <sub>2</sub>	1.8 mM
MgCl <sub>2</sub>	1 mM
Glucose	10 mM
HEPES	5 mM
pH (adjusted with NaOH)	7.4

**Table 2-40: Composition of Cs-IS/Cs-IS LB**

NaCl	14 mM
KAsp	130 mM
EGTA	1 mM
MgATP	2 mM
HEPES	10/1 mM
pH (adjusted with CsOH)	7.4

## 2.8.5 Combined pH-fluorometry and voltage clamp measurements

### 2.8.5.1 Voltage-clamp pH-fluorometry in mammalian cells

To monitor changes in the intracellular pH (pH<sub>i</sub>) in mammalian cells, the dye BCECF (2',7'-bis-(2-carboxyethyl)-5-(and-6)-carboxyfluorescein, Invitrogen) was used, a fluorescein derivate that changes its fluorescence properties in a pH-dependent manner with a pK<sub>a</sub> value of 6.98. BCECF can be imaged ratiometrically due to the fact that various parts of the fluorescence spectrum respond differently to pH changes. Whereas the fluorescence intensity increases with higher pH values when the dye is excited at 480 nm, no change can be observed for an excitation at 440 nm. The fluorescence is

then measured at both excitation wavelengths and the ratio of the two values is calculated. This fluorescence ratio  $R$  has the advantage that it is independent of dye concentration and bleaching effects (90).

For voltage clamp pH-fluorometry a single cell was selected. Prior to establishing the gigaseal, a rectangular aperture was adjusted to block out light from any surrounding cells or the background reaching the detector. The cell was loaded through the patch pipette which contained 50  $\mu\text{M}$  BCECF in IS LB. After the whole-cell configuration is established, the dye diffuses into the cell.

Ratiometric excitation of BCECF was performed by alternating excitation light from the monochromator of 440/12.5 nm and 480/12.5 nm at a frequency of 5 Hz. Either the filter set “Fs09” (Zeiss) or a custom filter-set for GFP (using Semrock BrightLine filters) was used (Table 2-33 and Table 2-34) with a 60x water objective (Olympus UplanSApo, 60x, 1.20 W) and a PTI D-104 photomultiplier system (Horiba).

### 2.8.5.2 Voltage-clamp pH-fluorometry in *D. rerio* sperm

As BCECF has shown to have toxic effects in sperm of several species, it was not used not pH fluorometry in zebrafish sperm. Instead, the dye pHrodo Red (Thermo Fisher) was used, which increases its fluorescence intensity with lower pH values. This dye was only available as an acetoxymethyl (AM) ester. Here, the dye is modified with AM groups that masks polar groups of the dye allowing it to cross the cell membrane. Inside the cytosol, intracellular esterases cleave off the AM groups which results in more polar dye molecules that can no longer pass across the membrane. In this manner, the dye accumulates inside the cell.

The sperm were attached to glass coverslips as described in 2.8.4, transferred into ES containing 15  $\mu\text{M}$  pHrodo Red-AM and incubated on ice for 20-60 min. After formation of the gigaseal and lifting of the sperm, a rectangular aperture was adjusted to block out light from any other sperm cells in the background. Excitation of pHrodo Red fluorescence was performed at 560/12.5 nm with the filter set “Fs 31” (Zeiss) (Table 2-33) and a 60x water objective (Olympus UplanSApo, 60x, 1.20W) and for detection a PTI D-104 photomultiplier system (Horiba) was used. After rupturing the

cell membrane to reach whole-cell configuration, the dye diffused out of the sperm into the patch pipette resulting in an exponential drop of fluorescence independently of pH. To correct for this, an exponential function was fitted to the fluorescence signal while the sperm was held at -15 mV. The entire fluorescence signal was then divided by this function which resulted in a stable baseline ( $\Delta F/F$ ).

## **2.8.6 Electrophysiological measurements of *X. laevis* oocytes**

### **2.8.6.1 Measurements of excised macropatches**

Patch-clamp measurements of oocytes were performed using the macropatch (or “giant patch”) technique. In this technique, relatively large excised patches (10-40  $\mu\text{m}$  diameter) that contain a large number of channels are used. This allows the measurement of larger currents than in conventional excised patches resulting in a better signal to noise ratio (91).

Before the measurement, the oocyte was mechanically devitellinated using forceps and placed in the measuring chamber. The patch pipettes were fire-polished using a Narishige MF-830 microforge (Narishige, Tokyo, Japan) to have an initial resistance of 0.7-1.5  $\text{M}\Omega$  (corresponding to an inner tip diameter of 10-20  $\mu\text{m}$ ). For measurements of proton reversal potentials solutions with high buffer concentrations and no alkali ions were used. These were similar to those used for mammalian cells (Chapter 2.8.3), but had a slightly different composition in order to feature an appropriate osmolarity for *Xenopus* oocytes (approx. 200 mOsmol/kg, Table 2-41). For measurements of cation selectivity, similar solutions were used. Here, the solutions contained either 90 mM of NMDG or of a certain cation (Table 2-42 and Table 2-43).

**Table 2-41: Composition of oocyte solutions for proton reversal potential measurements**

MES/HEPES	100 mM
MS	30 mM
TEA-Cl	5 mM
EGTA	5 mM
pH (adjusted with TEA-OH)	variable

**Table 2-42: Composition of oocyte solution for cation selectivity (NMDG-based)**

NMDG	90 mM
HCl	5 mM
MES	60 mM
EGTA	3 mM
pH (adjusted with MS)	variable

**Table 2-43: Composition of oocyte solution for cation selectivity (for various cations)**

Cation hydroxide	85 mM
Cation chloridel	5 mM
MES	60 mM
EGTA	3 mM
pH (adjusted with MS)	variable

### 2.8.6.2 Two-electrode voltage-clamp measurements

To measure whole-cell currents in *Xenopus* oocytes, the two-electrode voltage-clamp technique was employed. Here, the oocyte was directly impaled with two sharp electrodes with an initial resistance of 0.3 – 1.5 M $\Omega$ . The recording pipettes were filled with 3M KCl solution and the oocyte was bathed in ND96 (Table 2-15). Voltage-clamp was performed using a GeneClamp 500 amplifier with HS-2A headstage units (Molecular Devices). The measured data was acquired via a USB-6341 acquisition board (National Instruments, Austin, TX) with WinWCP (92) as the data acquisition software.

### 2.8.7 The liquid-junction potential

A liquid-junction potential develops, whenever two solutions with different ionic compositions come into contact. In electrophysiology, this happens when a different solution is used in the pipette than the bath solution. At the interface of the two solutions, each ion species moves according to its specific concentration gradient. The different magnitudes in the concentration gradients and differences in the mobilities of the different ion species can cause a potential to develop (e.g. the pipette solution might lose  $K^+$  more rapidly than gaining  $Na^+$  ions and gaining  $Cl^-$  ions more rapidly than losing  $Asp^-$ ). This potential needs to be compensated before the measurement by applying an offset potential. But once the gigaseal is established, the pipette solution is no longer in contact with the bath solution and the liquid junction potential disappears while the offset potential is still applied. Throughout the following measurement this offset potential is added to the membrane potential resulting in an error in the measured membrane voltage. In this thesis, this error was calculated using the liquid-junction potential calculator JPCalcW which is included in the pClamp 10 software. This program is based on the JPCalc program by P. H. Barry (93). The liquid-junction potential for ES and IS was -15.4 mV and the membrane voltage was adjusting accordingly offline.

## 2.9 pH-fluorometry of *D. rerio* sperm

### 2.9.1 Single-cell pH-fluorometry

For single-cell fluorometry of zebrafish sperm, the sperm were adhered to coverslips and loaded with pHrodo Red as described previously (Chapter 2.8.5.2). The cells were placed in a patch-clamp measuring chamber and perfused with different solutions. To hyperpolarize the sperm, a modified ES with only a very low  $K^+$  concentration (40  $\mu M$ ), similar to fresh water (94), but with the same osmolarity (adjusted with mannitol). To activate motility and assess the vitality of the sperm, a ES with a 50% reduced concentration of NaCl was used in order to induce a hypoosmotic shock. The experiment was carried out on an inverted IX71 microscope (Olympus) with a 60 $\times$

water objective (Olympus UplanSApo, 60×, 1.20 W). Fluorescence excitation was performed with a LED at 550 nm (SPECTRA X LED, Lumencor, Beaverton, USA) and a custom filter set (Table 2-44). The fluorescence was recorded using an iXon Ultra emCCD camera (Andor Technology, Belfast, North Ireland). After recording, a circular region of interest (ROI) was selected covering the sperm head and the fluorescence signal over time was determined. Only sperm that showed a motility response upon activation with hypoosmotic solution and thereby deemed vital were selected for analysis.

**Table 2-44: Specifications of the custom pHrodo Red filter set**

excitation filter	bandpass 543/22 nm
dichroic	562 nm
emission filter	longpass 568 nm

### 2.9.2 pH-fluorometry in the stopped-flow apparatus

For pH-fluorometry of populations of zebrafish sperm, a stopped-flow device ( $\mu$ SFM, Bio-Logic, Claix, France) was used. This device allowed the precise and rapid mixing (within milliseconds) of the contents of two different syringes; the mixture is then transferred to a measuring cuvette where fluorometric measurements occur. The sperm were loaded with pHrodo Red-AM (5  $\mu$ M in ES for 40-45 min at 18 °C). To activate the sperm, the sperm solution was mixed with a hypoosmotic ES that contained no NaCl (osmolarity: 36 mOsmol/kg). 16  $\mu$ l of the sperm solution (in ES) were mixed with 48  $\mu$ l hypoosmotic ES which resulted in a final osmolarity of 100 mOsmol/kg. Fluorescence excitation was performed using a M565L3 LED (Thorlabs, Newton, NJ) that was modulated at 50 kHz with a 628/40 nm emission filter (Semrock). The fluorescence signal was detected with a H10723-20 photomultiplier tube (Hamamatsu Photonics, Hamamatsu, Japan) and then amplified and filtered through a 7230 General Purpose DSP lock-in amplifier (Ametek, Berwyn, PA). Data were recorded with a PCI-6221 data acquisition board (National Instruments) with the Bio-Kine acquisition software (Bio-Logic).

## 3 Results

---

During my PhD thesis, I studied a member of a new subfamily of HCN channels that has been identified by our laboratory in zebrafish sperm, drHCNL1. In sea urchin sperm, HCN channels are required for recovery from hyperpolarization and subsequent activation of the voltage-activated  $\text{Ca}^{2+}$  channel CatSper; they play a key role in the chemotactic signaling cascade and thus in fertilization (1,16). The study of zebrafish sperm might be particularly interesting because most knowledge about sperm physiology stems from marine invertebrates and mammals, which fertilize in environments that are rich in various ions (1,16). In contrast, zebrafish reproduction takes place in freshwater, which contains only very low concentrations of almost all ions. Not much is known about the sperm physiology and underlying signaling molecules of freshwater fish. To date, only two ion channels have been identified in zebrafish sperm, drCNGK and drHCNL1 (16,19,56). Thus, the study of drHCNL1 may offer insight, how a well-known protein adapts during evolution to a unique environment.

I started characterizing drHCNL1 during my master thesis. Back then, I could demonstrate that drHCNL1 selectively conducts protons. Also, my work provided preliminary evidence that the channel might use the S4 segment, the so-called “voltage sensor”, as permeation pathway (56). After a brief description of the HCNL protein family, I will summarize some of these previous findings along with additional evidence that defines drHCNL1 channels as novel hyperpolarization-activated, highly selective proton channels. I will continue to present evidence that the voltage-sensing domain (VSD) is indeed the permeation pathway and that each drHCNL1 channel contains four pores. Also, I will briefly outline my efforts to characterize drHCNL2, a second member of the HCNL channel family. Finally, I will describe measurements of drHCNL1 in zebrafish sperm and outline the possible physiological role of drHCNL1 in zebrafish sperm.

### 3.1 The HCNL protein family

During a proteomic search for ion channels involved in the signaling cascade of zebrafish sperm (19), peptides of a putative HCN channel (NCBI accession number XP\_002662296) were identified (Figure 3-1a). The amino-acid sequence of this new channel overall is similar to other HCN channel sequences. Like HCN channels, the new channel possesses six transmembrane segments (S1-S6) (Figure 3-1); S1-S4 form a voltage-sensing domain (VSD) with several positively charged amino acids in S4. The transmembrane segments S5 and S6 form the pore domain (PD). Both, HCN channels and the new channel share a C-terminal cyclic-nucleotide binding domain (CNBD) (Figure 3-1).

To analyze how much the amino-acid sequence of the new channel is conserved, an alignment with human HCN2 (hsHCN2) was created, and each amino acid was assigned a conservation value (displayed on a false color scale in Figure 3-1a). This conservation value represents the similarity of the respective amino acid with its counterpart in hsHCN2. The more physico-chemical properties the two amino acids have in common, the higher the conservation value. In the case that all properties match, a conservation value of 10 is assigned. Identical amino acids receive a conservation value of 11 (95).

Several HCN channels (spIh from the sea urchin *Strongylocentrotus purpuratus*, hsHCN1 from human, and mmHCN2 from mouse) have similar sequences overall and therefore receive high conservation values when compared to hsHCN2 (mean conservation values: spIh:  $9.25 \pm 2.53$ , hsHCN1:  $10.36 \pm 1.88$ , mmHCN2:  $10.76 \pm 1.53$ , mean  $\pm$  standard deviation (s.d.)) (Figure 3-1a). For drHCNL1, sequence conservation is high in the six transmembrane segments (mean conservation value:  $8.97 \pm 1.92$ ) and several motifs that are common to classical HCN are also conserved (e.g. positively charged amino acids in S4, Figure 3-1a). However when analyzing the overall sequence, the mean conservation value (in reference to hsHCN2) is lower than that of another predicted zebrafish HCN channel (drHCN2) (drHCNL1:  $7.81 \pm 2.89$ , drHCN2:  $10.61 \pm 1.71$ ). It was therefore termed drHCNL1 (for HCN-like channel 1).

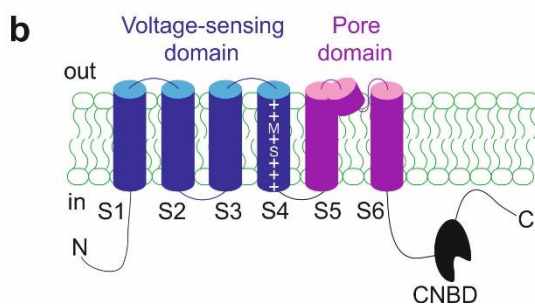
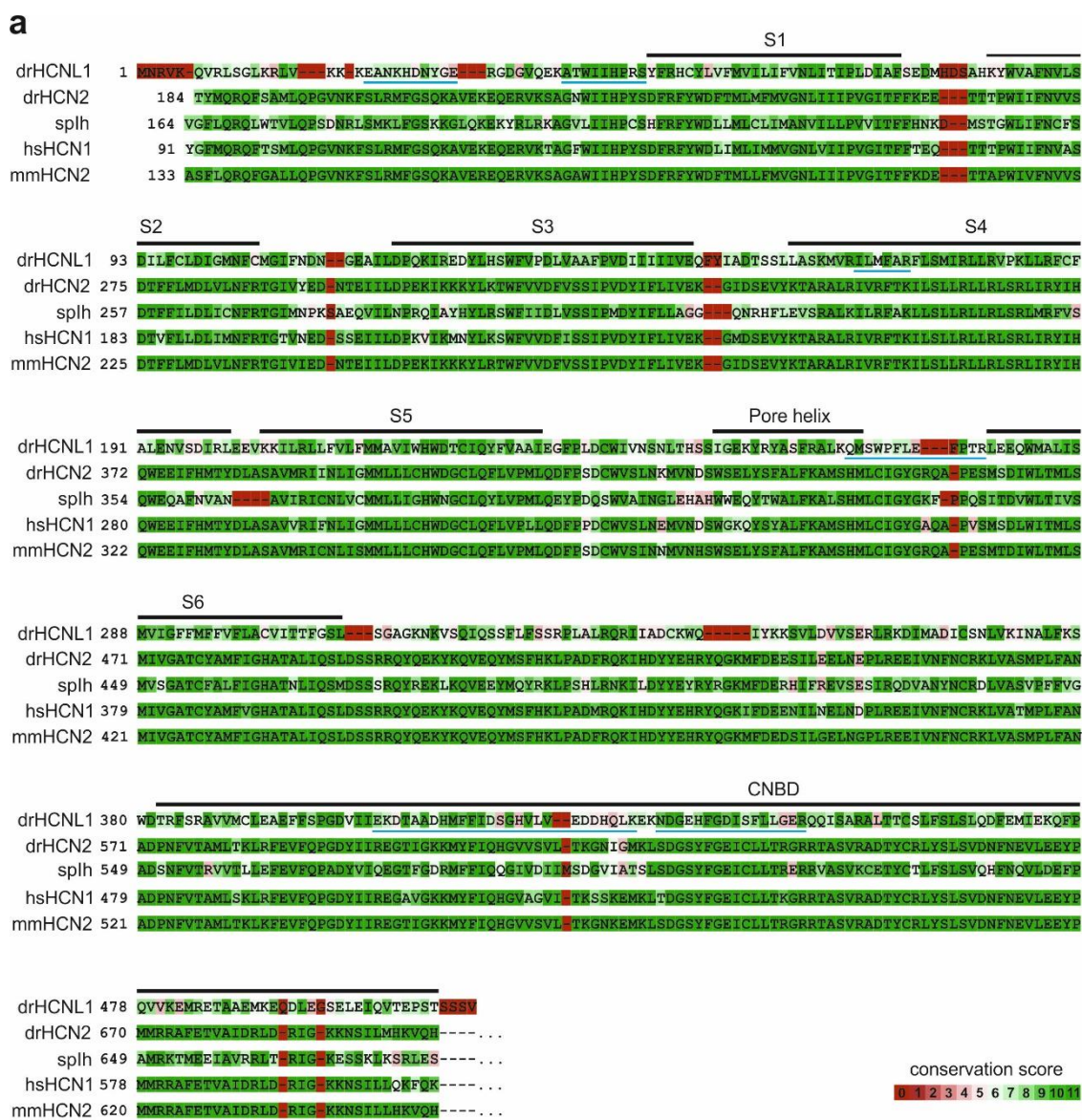


**Figure 3-1: Sequence alignment of drHCNL1 with several HCN channels.** **a**, Sequence alignment of full length drHCNL1 (*Danio rerio*), and core regions of drHCN2, splh (*Strongylocentrotus purpuratus*), hsHCN1 (*Homo sapiens*), and mmHCN2 (*Mus musculus*). Sequences are sourced from NCBI (accession numbers see Figure 6-1). Sequences are underlaid with their conservation score in reference to hsHCN2 (95). Helices and the CNBD, as identified in the hsHCN1 structure (46) are depicted by lines. The six tryptic peptides detected in zebrafish sperm with mass spectrometry are depicted by blue underlines. **b**, Cartoon of the presumed topology of drHCNL1.

A database search revealed 49 orthologue genes, all from fish (Supplemental Figure 6-1). Figure 3-2 depicts a phylogenetic tree of several HCNL channels, classical HCN channels and several other  $K^+$  channels containing a CNBD. In this tree, the previously established ion channels fall into distinct clusters representing the different ion channel families, with drHCN2 clustering together with other HCN channels. The HCNL channels do not fall into any of these established families; they form two groups: HCNL1 and HCNL2 channels, with HCNL2 channels being more similar to classical HCN channels than HCNL1 channels. As the nodes where HCNL and classical HCN channels diverge lie very close together in comparison to other channel families, it appears that they both belong the HCN channel family; within the HCN channel family, the HCNL channels constitute a novel subfamily alongside the classical HCN channels (Figure 3-2).

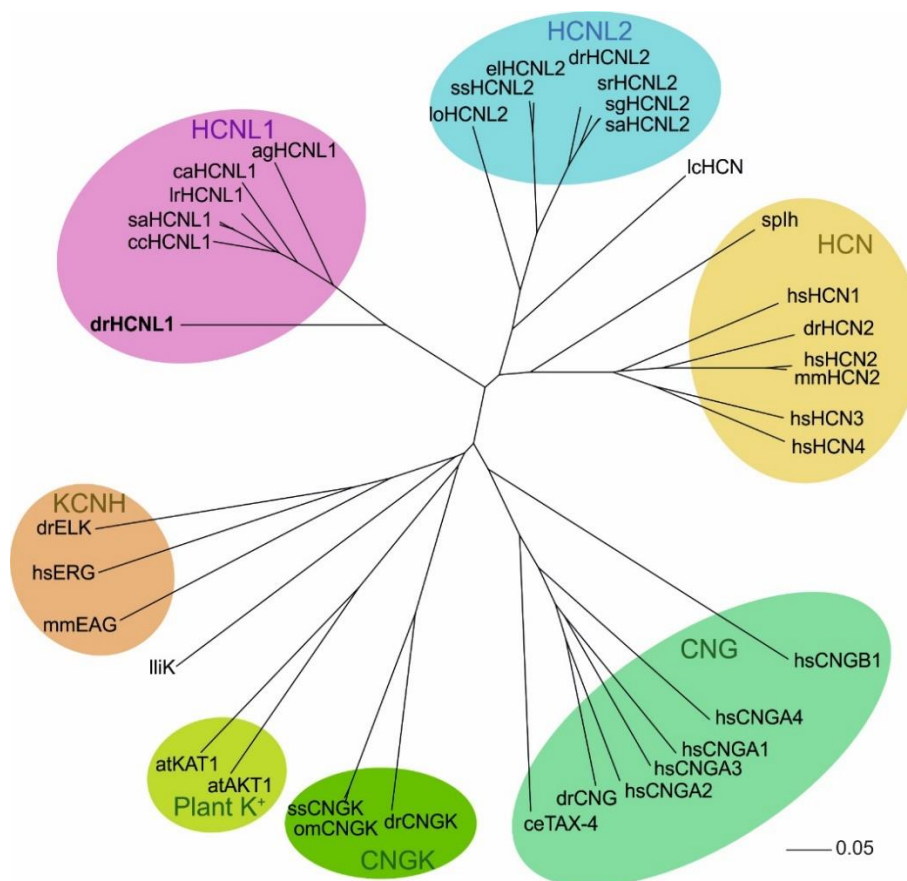


**Figure 3-2: The HCNL channel family.** Phylogenetic tree of ion channels containing a CNBD (accession numbers of HCNL1/2 channels are listed in Figure 6-1). Channel families are highlighted. Scale bar represents 0.05 substitutions per site.

### 3.2 Activation of drHCNL1

During my master thesis, I began to characterize the biophysical properties of drHCNL1 by heterologous expression in CHO cells (56). In transfected cells, hyperpolarizing voltage steps led to inward currents reminiscent of currents elicited by classical HCN channels (30,96)(Figure 3-3 a). These currents were half-maximal at  $V_{1/2} = -98.8 \pm 6.8$  mV with a slope of  $s = 5.8 \pm 1.5$  mV (mean  $\pm$  s.d.),  $n = 6$  experiments), which is similar to classical HCN channels. Before my PhD thesis, Sylvia Fechner had begun to characterize drHCNL1 and observed no sensitivity to cyclic nucleotides (personal communication); this finding is unexpected because a key characteristics of classical HCN channels is their change in voltage-dependence upon binding of cyclic nucleotides. During my PhD thesis, I studied the cyclic nucleotide sensitivity in greater detail: indeed, drHCNL1 showed no change in voltage dependence in the presence of either cAMP or cGMP (cAMP:  $V_{1/2} = -96.6 \pm 3.6$  mV,  $s = 6.6 \pm 1.3$  mV,  $n = 5$ ; cGMP:  $V_{1/2} = -100.1 \pm 3.0$  mV,  $s = 5.8 \pm 1.2$  mV,  $n = 6$ , Figure 3-3b).

### 3 Results

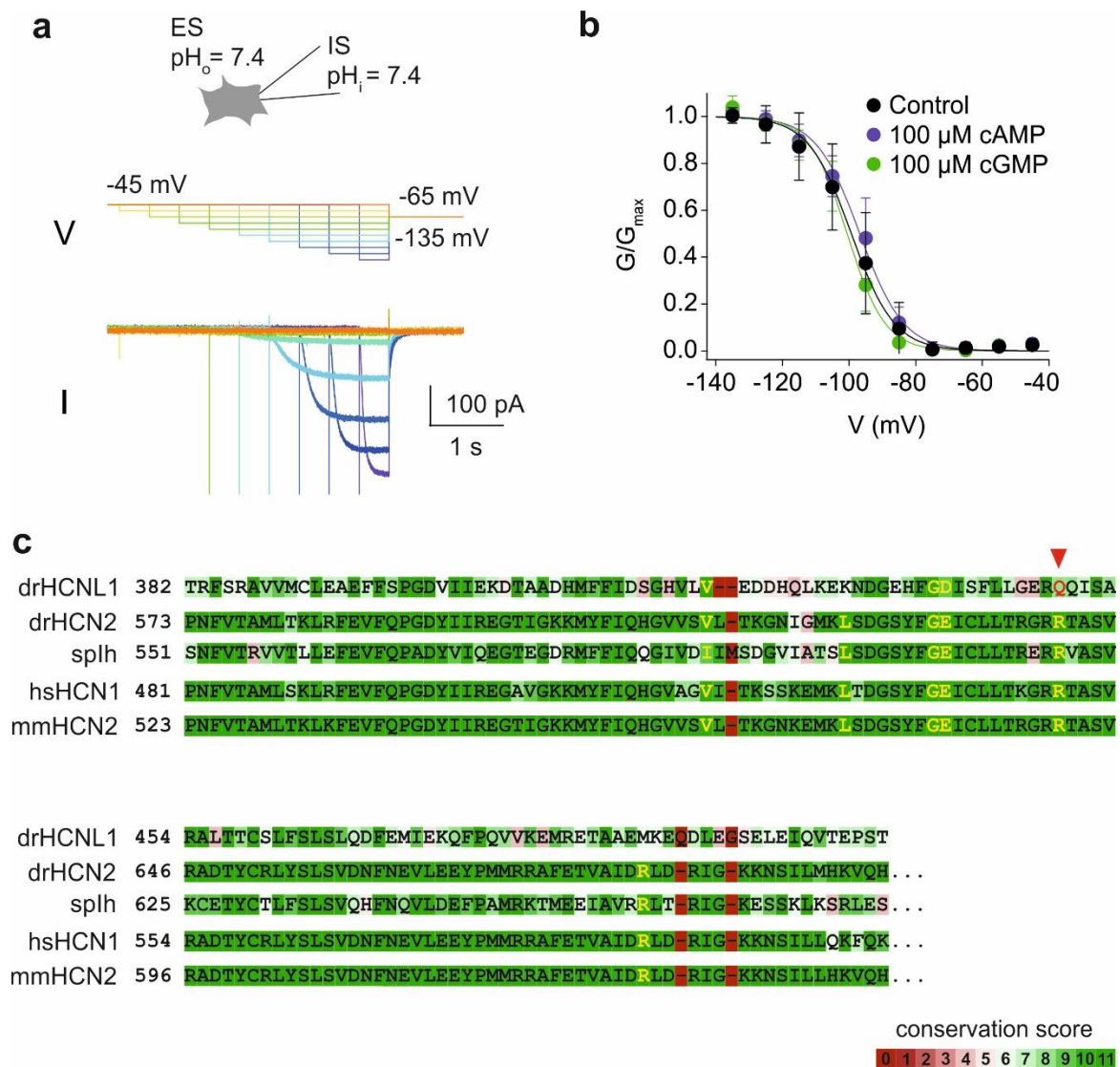


**Figure 3-3: Hyperpolarization-activated currents in drHCNL1-expressing CHO cells. a,** Whole-cell patch-clamp recording of a drHCNL1-expressing CHO cell. Voltage steps of increasing length and decreasing amplitude (color-coded, -135 to -45 mV in 10 mV increments) elicited voltage-dependent inward currents. **b,** Conductance-voltage relationships (GVs) derived from tail currents of drHCNL1-expressing CHO cells without (black) or with 100 μM intracellular cAMP (blue) or cGMP (green). **c,** Alignment of CNBDs of drHCNL1 and HCN channels. Sequences are underlaid with their conservation score in reference to hsHCN2 (95). Several amino acids involved in cyclic nucleotide binding are highlighted (97). Red arrow indicates an arginine not conserved in drHCNL1. Error bars denote standard deviation. Parts of this data set were already published in (56). Sylvia Fechner and Thomas Berger contributed to the data set shown in (b).

At first glance, this insensitivity to cyclic nucleotides seems surprising, because drHCNL1 possesses a CNBD with a relatively well conserved sequence. However, a crucial arginine (R591 in mmHCN2) is not conserved in drHCNL1 (Figure 3-3c). It interacts electrostatically with the phosphate group of the cyclic nucleotide and is,

therefore, critical for binding (98–100). The effect of a change from R to Q in drHCNL1 has been previously described by mutagenesis in classic HCN channels: the R/Q substitution considerably lowers the affinity of the CNBD for cyclic nucleotides, and channels functionally lose their sensitivity to cyclic nucleotides (99,101).

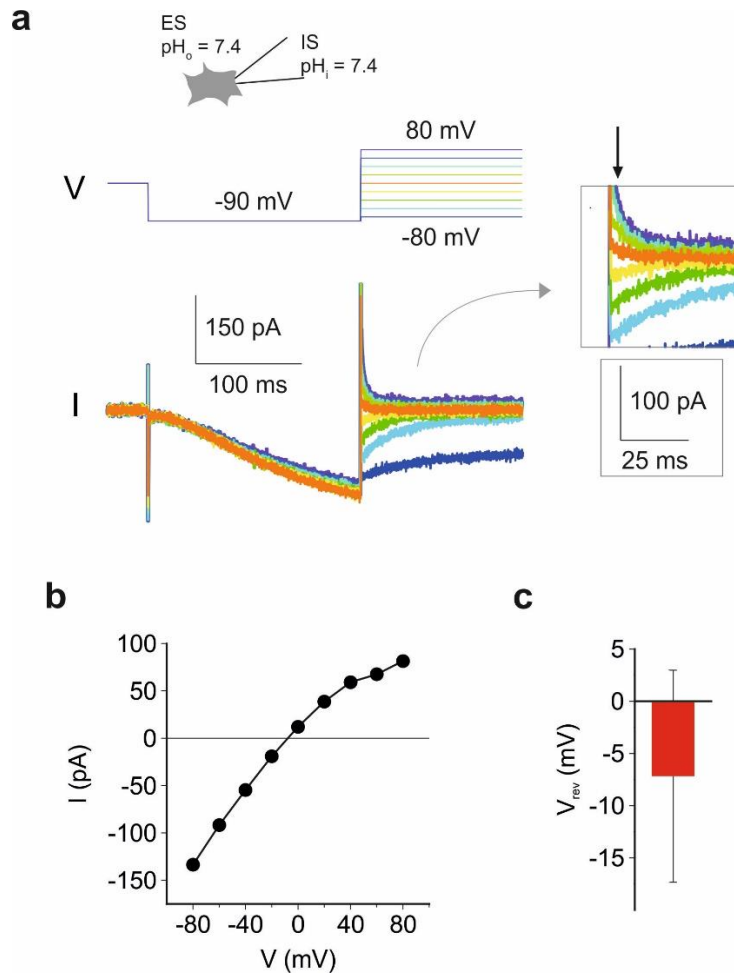


**Figure 3-4:  $V_{rev}$  of drHCNL1 in physiological solutions.** **a**, Whole-cell patch-clamp recording of a drHCNL1-expressing CHO cell to determine  $V_{rev}$ . After activation of drHCNL1 currents at -90 mV, various test voltage from -80 mV to +80 mV (color-coded) were applied. Inset shows magnified tail currents. The point in time where tail currents were analyzed is indicated by an arrow. **b**, Current-voltage relationship of tail currents of the measurement shown in (a). The voltage where the line crosses the x-axis is  $V_{rev}$ . **c**, Mean  $V_{rev}$  of drHCNL1 in physiological solutions ( $-7.18 \text{ mV} \pm 10.19 \text{ mV}$ ,  $n = 10$ ). Error bars denote standard deviation.

### 3 Results

In solutions mimicking physiological ion concentration of many mammalian cells (Table 2-35 and Table 2-36), the voltage at which currents through drHCNL1 reversed direction ( $V_{rev}$ ) was  $-7.18 \text{ mV} \pm 10.19 \text{ mV}$ , although this value was quite variable (Figure 3-4c). When all ion concentrations in intracellular and extracellular solutions are known, the ion selectivity of the channel can be inferred from  $V_{rev}$ . If an ion channel conducts only ion  $X^+$ , the  $V_{rev}$  will be equal to the Nernst potential that is described by the following equation:

$$E = \frac{RT}{zF} \ln \frac{[X^+]_{out}}{[X^+]_{in}} \quad \text{Eq. 1}$$

where  $R$  is the ideal gas constant,  $T$  the temperature in Kelvin,  $z$  the charge of the ion,  $F$  is Faraday's constant and  $[X^+]_{out}$  or  $[X^+]_{in}$  are the concentrations of the ion outside and inside of the cell, respectively. If an ion channel conducts several ion species, the  $V_{rev}$  will be a combination of the Nernst potentials of the conducted ions. HCN channels conduct both  $K^+$  and  $Na^+$  and the  $V_{rev}$  lies between the two respective Nernst potentials. In the solutions that were used in the experiment in Figure 3-4,  $E_{Na^+} = 58.6 \text{ mV}$  and  $E_{K^+} = -80.9 \text{ mV}$  (at  $22 \text{ }^\circ\text{C}$ ). Therefore, the  $V_{rev}$  of  $-7.18 \pm 10.19 \text{ mV}$  measured for drHCNL1 could be explained due to the channel conducting both  $Na^+$  and  $K^+$ . However, during my master thesis I could show that drHCNL1 conducts protons instead (56). In the next chapter, I will describe how we made this unexpected discovery and our attempts at quantifying the selectivity of drHCNL1 for protons.

### 3.3 Selectivity of drHCNL1 for protons

#### 3.3.1 DrHCNL1 conducts protons

In my master thesis, I could show that drHCNL1 does not conduct  $\text{Na}^+$  and  $\text{K}^+$  ions, like classical HCN channels, but conducts protons instead (56). An observation that prompted investigation whether protons are the permeant ion of drHCNL1 was that, upon prolonged stimulation, tail currents changed their direction from inward to outward (Figure 3-5). A possible reason for this could be that the ion selectivity of drHCNL1 is changed. There are a few precedents of channels sub-conductance states with an altered selectivity were found (102–104).

Another explanation could be that ions are redistributed at the membrane. If large currents flow across the membrane, sometimes the conducted ions are locally accumulated or depleted, which will affect  $V_{\text{rev}}$ . For abundant ion species such as  $\text{Na}^+$  or  $\text{K}^+$ , the ion concentration is so high that redistribution through ion channels is negligible. However, redistribution effects can become significant when the concentration of the respective ion is very low. In particular protons, given their low concentration under physiological conditions ( $\text{pH } 7.4 - 7.2 \triangleq 40 - 63 \text{ nM}$ ), are prone to redistribution during proton-channel activity (105). In the example shown (Figure 3-5), the proton concentration outside and inside of the cell is the same ( $\text{pH}_o = 7.4$  and  $\text{pH}_i = 7.4$ ). Thus, the Nernst potential for protons is  $E_{\text{H}^+} = 0 \text{ mV}$ ; under these conditions at  $-45 \text{ mV}$ , a proton-selective channel should give rise to an inward current. This is true for a short 100-ms activation where any redistribution effects should be small (Figure 3-5a, red arrow). However, when stimulated for a prolonged time, the tail current is an outward current (Figure 3-5b, black arrow), suggesting that stimulation led to redistribution of protons, such that  $E_{\text{H}^+} < -45 \text{ mV}$ . For  $\text{pH}_o = 7.4$ , this  $E_{\text{H}^+}$  is achieved at  $\text{pH}_i < 6.64$ .

### 3 Results

Additionally, during the prolonged stimulation, the amplitude of the inward current decreases over time (Figure 3-5b). This effect is called “current droop” and has been described for the voltage-gated proton channel  $H_v1$ ; it is also due to proton redistribution (105). Upon prolonged stimulation of drHCNL1 the intracellular proton concentration increases, which creates an outward-directed concentration gradient that counteracts the inward current of protons.

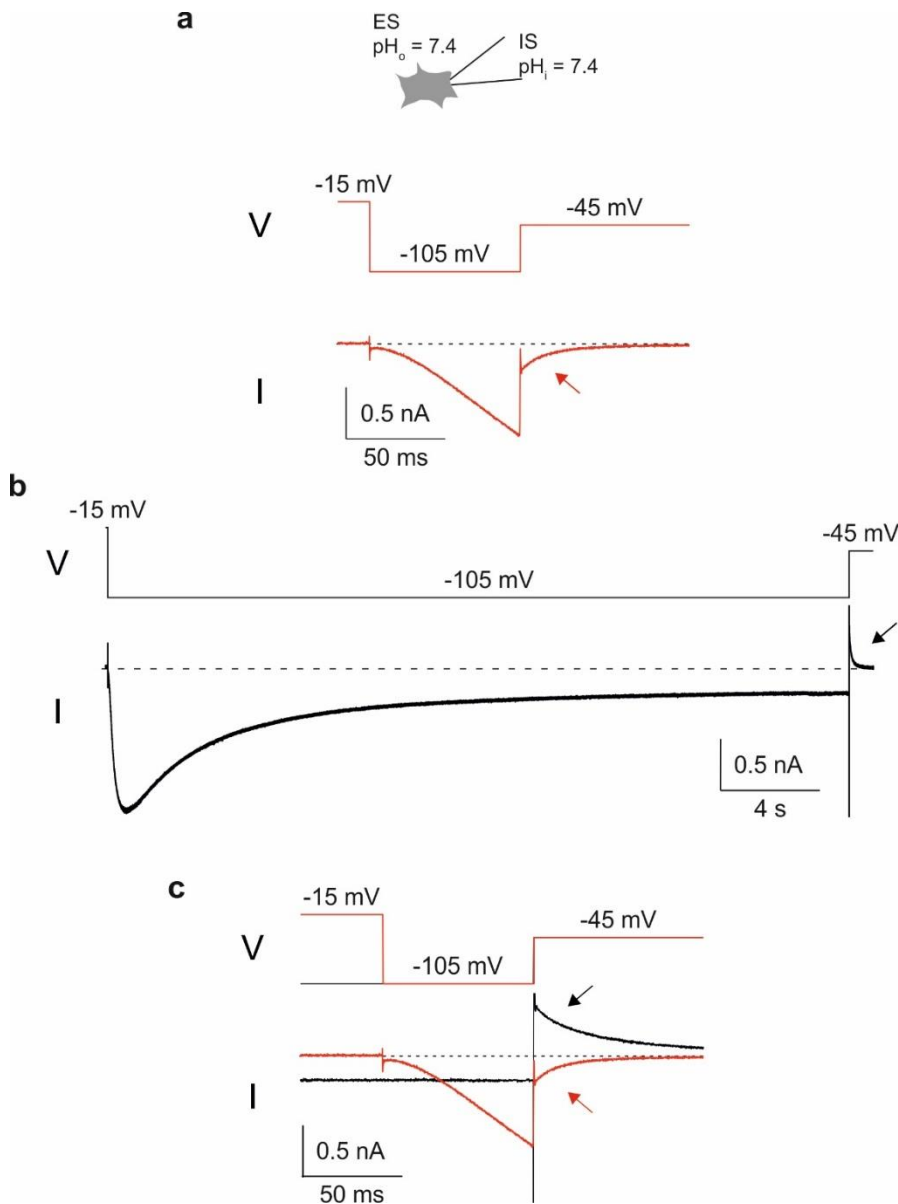


**Figure 3-5: Tail currents of drHCNL1 depend on stimulus length in low pH-buffer conditions. a–c,** Whole-cell patch-clamp recording of zebrafish HCNL1-expressing CHO cells. Hyperpolarizing voltage steps to  $-105$  mV were applied for 75 ms (a) or 15 s (b), followed by a voltage step to  $-45$  mV. Note the change in the direction of the tail current after the long stimulation (arrows). Panel (c) shows the two traces of panel (a) and (b) aligned on the time axis such that tail currents start at the same time point.

In my master thesis, I measured changes in  $\text{pH}_i$  induced by drHCN1 with the  $\text{pH}$ -sensitive dye BCECF that was loaded into the cell via the patch pipette. Upon reaching the whole-cell conformation, the dye diffused from the pipette into the cell indicated by an increase in fluorescence (Figure 3-6a). BCECF can be imaged ratiometrically by exciting the dye with light of 440 nm and 480 nm wavelength (Figure 3-6b). The ratio mode avoids correcting for variations in dye concentration and bleaching effects; in addition, it has the advantage that measurements could begin much earlier. Upon disruption of the membrane patch to reach whole-cell conformation (indicated by arrows in Figure 3-6b), the fluorescence at both excitation wavelengths increased slowly reaching a plateau within 5-10 minutes. In contrast, the ratio of fluorescence at both wavelengths reaches a stable value within approx. 30 seconds (Figure 3-6b).

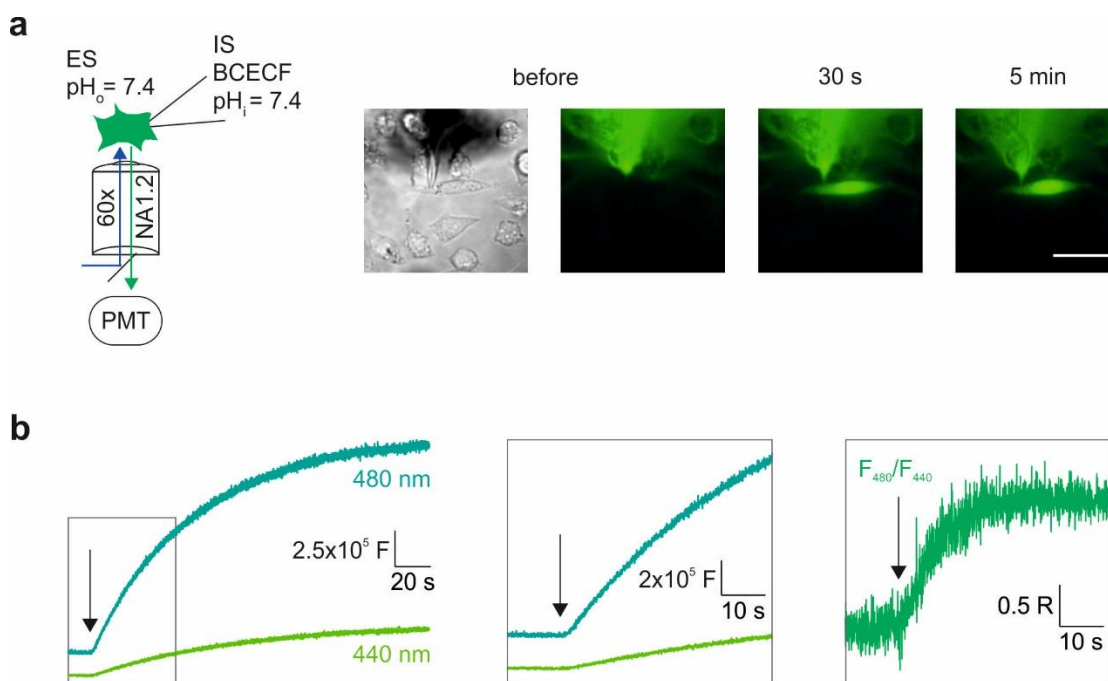


**Figure 3-6: Ratiometric imaging of CHO cells loaded with the  $\text{pH}$ -sensitive dye BCECF.** **a**, *Left panel:* Recording configuration. *Images from left to right:* Brightfield and fluorescence image of the patch pipette and a CHO cell before disruption of the membrane patch and fluorescence images 30 s and 5 min after disruption of the membrane patch, respectively. Fluorescence was excited at 480 nm. **b**, *Left panel:* Increase of fluorescence during loading with BCECF, excited at 480 nm (teal) and 440 nm (light green) after disruption of the membrane patch to reach whole-cell conformation (arrow). *Middle panel:* Magnified image of the highlighted section in the left panel. *Right panel:* Increase in the ratio of fluorescence excited at 440 and 480 nm (R, green). The ratio R (green, right panel) reaches a stable value more rapidly than both individual fluorescence values (teal and light green, middle panel).

### 3 Results

I recorded from CHO cells, loaded with BCECF, expressing either drHCNL1 or mmHCN2 (a classical HCN channel). In these experiments, I used pipet solutions with a low pH-buffer concentration (1 mM HEPES) in order to observe changes caused by proton currents more easily. When drHCNL1 was activated by hyperpolarization, the fluorescence ratio of BCECF decreased, indicating intracellular acidification. This shows that drHCNL1 indeed conducts protons. Similar to the experiment using prolonged stimulation (Figure 3-5b), I observed a marked “current droop” indicative of proton redistribution. During activation of mmHCN2, no change in BCECF fluorescence was observed, demonstrating that classical HCN channels do not conduct protons.

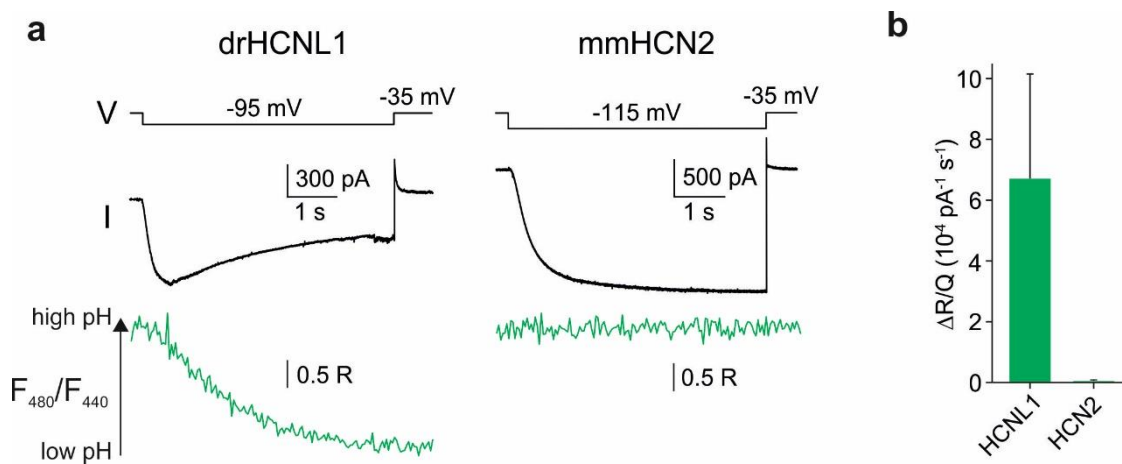


**Figure 3-7: drHCNL1 currents cause intracellular acidification.** **a**, Whole-cell patch-clamp fluorometry recording of drHCNL1- or mmHCN2-expressing CHO cells, loaded with BCECF. Upon activation of drHCNL1, the fluorescence ratio drops indicating acidification. **b**, Change in ratio of fluorescence amplitude over transported charge (drHCNL1,  $6.7 \times 10^{-4} \pm 3.4 \times 10^{-4} \text{ pA}^{-1}\text{s}^{-1}$ ,  $n = 9$ ; mmHCN2,  $5.1 \times 10^{-6} \pm 3.2 \times 10^{-6} \text{ pA}^{-1}\text{s}^{-1}$ ,  $n = 5$ ). Parts of this data set were already published in (56). Error bars denote standard deviation.

Another piece of evidence indicating that drHCNL1 indeed conducts protons is that currents persist in solutions previously established in the study of proton-selective channels. These solutions contain high pH-buffer concentrations that minimize proton redistribution and large organic cations instead of alkali-metal ions (85–87), which typically do not permeate ion channels (85,86). During my master thesis, I measured drHCNL1 in the aforementioned solutions and large currents persisted (Figure 3-8). The currents also resembled those measured in physiological solution in shape (see Figure 3-3) and had a similar voltage dependence ( $V_{1/2} = -116.3 \pm 3.1$  mV,  $s = 7.4 \pm 1.3$  mV,  $n = 5$ , Figure 3-8).

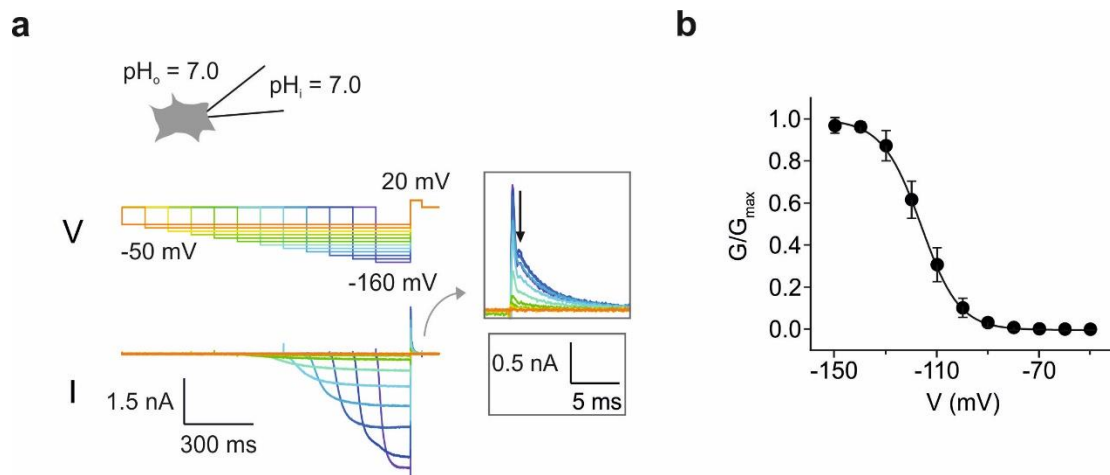


**Figure 3-8: DrHCNL1 currents persist in NMDG-based solutions.** **a**, Whole-cell patch-clamp recording of a drHCNL1-expressing CHO cell. Voltage steps of increasing length and decreasing amplitude (color-coded,  $-160$  to  $-50$  mV in 10 mV increments) elicited voltage-dependent inward currents. **b**, Conductance-voltage relationships (GVs) derived from tail currents of drHCNL1-expressing CHO cells. Error bars denote standard deviation. Parts of this data set were already published in (56).

I also wanted to assess whether proton conductance is unique to drHCNL1 or a property common to all HCNL1 channels. Within the scope of this thesis, I did not have the opportunity to characterize HCNL1 channels from other species in detail. However, I worked together with Thomas Berger to perform a similar experiment as shown in Figure 3-5 in *X. laevis* oocytes using two-electrode voltage-clamp (TEVC). After prolonged stimulation, tail currents of HCNL1 channels from common carp (*Cyprinus carpio*, ccHCNL1) and goldfish (*Carassius auratus*, caHCNL1) changed direction, as observed for drHCNL1 (58). For drHCNL1, this was due to redistribution of protons during channel activation (see above). The fact that we observe the same phenomenon in these other HCNL1 channels suggests that they probably also conduct protons. However, the fact that these are indeed proton channels still needs to be shown directly (e.g. by monitoring  $\text{pH}_i$  upon current activation with a pH-sensitive dye as in Figure 3-7).

### 3.3.2 Quantification of the proton selectivity of drHCNL1

The reversal potential  $V_{rev}$  is routinely used to estimate the ion selectivity of ion channels. One possible experimental approach is to measure the reversal potential under conditions where only one ion species (e.g.  $A^+$ ) is conducted. A second ion species (e.g.  $X^+$ ) is then added to one side of the membrane. The resulting shift of  $V_{rev}$  is proportional to how much  $X^+$  is conducted compared to  $A^+$ , i.e. the permeability of  $X^+$  ( $P_{X^+}$ ) compared to the permeability of  $A^+$  ( $P_{A^+}$ ).

In order to describe the contribution of both ions to  $V_{rev}$ , we can use of the Goldman-Hodgkin-Katz (GHK) equation. The GHK equation describes the reversal potential of the membrane based on ion concentration on the inside and outside of the membrane and the membrane's permeability for those ions, and was devised by Hodgkin and Katz in 1949 based on previous work by Goldman in 1943 (106,107).

$$V_{rev} = \frac{RT}{F} \ln \frac{P_{K^+}[K^+]_{out} + P_{Na^+}[Na^+]_{out} + P_{Cl^-}[Cl^-]_{in}}{P_{K^+}[K^+]_{in} + P_{Na^+}[Na^+]_{in} + P_{Cl^-}[Cl^-]_{out}} \quad \text{Eq. 2}$$

In the scenario that I described above, where only  $A^+$  is the only conducted ion species and  $X^+$  is then added to only the outside of the membrane, we can modify the equation to the following form:

$$V_{rev} = \frac{RT}{F} \ln \frac{P_{X^+}[X^+]_{out} + P_{A^+}[A^+]_{out}}{P_{A^+}[A^+]_{in}} \quad \text{Eq. 3}$$

I tried this experiment during my master thesis. Unfortunately, due to proton redistribution effects caused by currents through drHCNL1 (see Chapter 3.3.1), it proved very difficult to accurately measure  $V_{rev}$  (i.e. to obtain values agreeing with the calculated  $E_{H^+}$  under experimental conditions where only protons can be conducted, see Figure 3-8). Even in solutions with high buffer concentrations to minimize proton redistribution,  $V_{rev}$  values were lower than calculated values (Figure 3-9b).

This deviation from the expected  $V_{\text{rev}}$  value is likely due to proton redistribution effects during activation of drHCNL1. Often protons are accumulated and/or depleted locally at the membrane. Although a more than sufficient amount of buffer is available in the bulk solution, the amount available at the site of the proton influx is limited by diffusion (105). If protons are accumulated at the inside of the membrane during drHCNL1 activation, this local shift in  $\text{pH}_i$  shifts  $E_{\text{H}^+}$  in the same manner as if  $\text{pH}_i$  had changed throughout the whole intracellular volume. As described in Chapter 3.3.1, the influx of protons acidifies the intracellular side of the membrane and shifts the reversal potential of drHCNL1 towards more negative values (Figure 3-5).

The hypothesis that the deviation of  $V_{\text{rev}}$  is due to proton redistribution is supported by the fact that this deviation could be reduced by mitigating proton redistribution. An obvious method would be to reduce proton currents through drHCNL1 by applying hyperpolarizing voltage pulses of shorter duration and lower amplitude. Knowing the potential problem of proton redistribution, I continuously adjusted voltage protocols to keep proton currents as small as possible. However, a sufficiently larger current is required to accurately determine the reversal potential. Therefore, I systematically changed the pH of the solutions in which the measurements were performed. The pH can influence the magnitude of proton redistribution in two ways: first, if the overall concentration of protons is higher, a given proton flow will change the concentrations inside and outside the cell to a smaller extent. Second, if the concentration of protons is higher inside of the cell than outside of the cell (i.e.  $\text{pH}_i < \text{pH}_o$ ), inward proton currents will be smaller, resulting in less redistribution of protons; this difference in  $\text{pH}_i$  and  $\text{pH}_o$  can be expressed as  $\Delta\text{pH}$  ( $\Delta\text{pH} = \text{pH}_o - \text{pH}_i$ ). Indeed, when measured at lower pH ( $\text{pH}_o = 6$  vs.  $\text{pH}_o = 7$ , represented by circles and squares, respectively, in Figure 3-9b), the deviation of  $V_{\text{rev}}$  from the calculated  $E_{\text{H}^+}$  (indicated by the dashed line in Figure 3-9b) was smaller. This was also true, when  $\text{pH}_i$  was smaller than  $\text{pH}_o$  (i.e.  $\Delta\text{pH} > 0$ ). However, even at  $\text{pH}_i = 5.0$  and  $\text{pH}_o = 6.0$ , the measured  $V_{\text{rev}}$  was still 12.2 mV more negative than the  $E_{\text{H}^+}$  (Figure 3-9b).

Optimal conditions could only be obtained in excised inside-out patches from *X. laevis* oocytes: Thérèse Wolfenstetter found that when measured at  $\text{pH}_i = 5.5$  and  $\text{pH}_o = 6.5$ ,  $V_{\text{rev}}$  matched  $E_{\text{H}^+}$  (57). One reason, why this was not achieved in whole-cell recordings of CHO cells could be that diffusion of buffer molecules is likely better in an inside-out patch where a small patch of membrane is directly exposed to the bath solution. In *X. laevis* oocytes under the conditions described above, no shift in  $V_{\text{rev}}$  was measured upon the addition of various cations; thus, drHCNL1 was so selective for protons that other cations did not contribute to  $V_{\text{rev}}$  significantly (57).

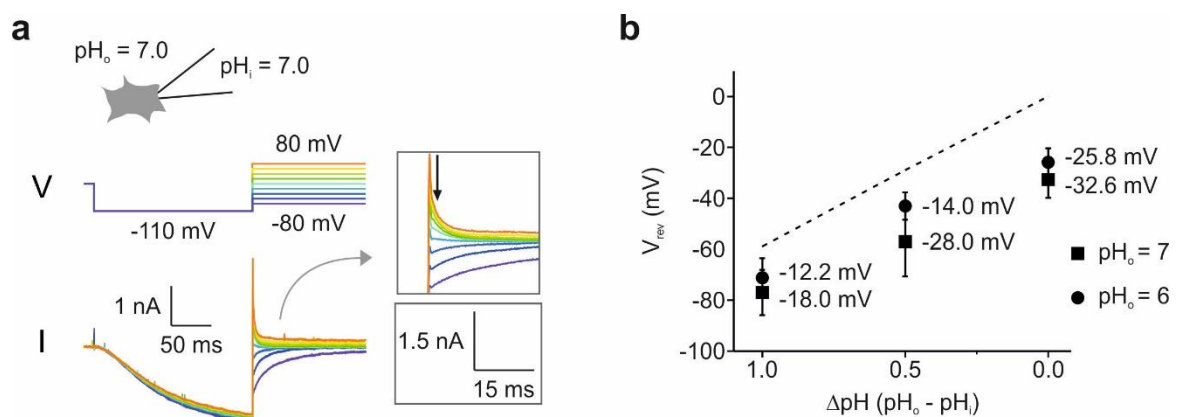


**Figure 3-9:  $V_{\text{rev}}$  of drHCNL1 approximately follows the Nernst potential for protons.** **a**, Whole-cell patch-clamp recording of a drHCNL1-expressing CHO cell to determine  $V_{\text{rev}}$ . After activation of drHCNL1 currents at -110 mV, various test voltage from -80 mV to +80 mV (color-coded) were applied. The point in time where tail currents were analyzed is indicated by an arrow. **b**,  $V_{\text{rev}}$  as a function of  $\Delta\text{pH}$  for  $\text{pH}_o = 7$  (squares) and  $\text{pH}_o = 6$  (circles) ( $\text{pH}_o = 7$ :  $\Delta\text{pH} = 1$ :  $V_{\text{rev}} = -77.0 \pm 8.9$  mV,  $\Delta\text{pH} = 0.5$ :  $V_{\text{rev}} = -57.0 \pm 13.8$  mV,  $\Delta\text{pH} = 0$ :  $V_{\text{rev}} = -32.6 \pm 7.2$  mV,  $n = 6$ ;  $\text{pH}_o = 6$ :  $\Delta\text{pH} = 1$ :  $V_{\text{rev}} = -71.2 \pm 7.7$  mV,  $\Delta\text{pH} = 0.5$ :  $V_{\text{rev}} = -43.0 \pm 5.4$  mV,  $\Delta\text{pH} = 0$ :  $V_{\text{rev}} = -25.8 \pm 5.4$  mV,  $n = 6$ ). Dashed line represents  $E_{\text{H}^+}$  and numbers indicate the deviation of the respective data point from  $E_{\text{H}^+}$ . Error bars denote standard deviation. Parts of this data set were already published in (56).

Even though we had established that the selectivity of drHCNCL1 for protons was very high, I still wanted to obtain some quantitative measure of its selectivity. In preliminary experiments that I had performed before Thérèse Wolfenstetter had established the optimal conditions to determine  $V_{rev}$ , I had seen shifts of  $V_{rev}$  upon addition of  $Na^+$  to the bath solution. This was likely due to the fact that I had performed my experiments at a higher pH ( $pH_i = pH_o = 7$ ). Because the proton concentration was lower in my experiments, the relative contribution of  $Na^+$  to  $V_{rev}$  was greater and could be quantified. Because I would be measuring at conditions where  $V_{rev}$  would not match calculated Nernst potential for protons even in the absence of any other ions, I chose to perform the experiment in CHO cells as I was more experienced in this method. I also chose to perform this experiment for  $Na^+$  only because drHNCL1, based on the data obtained by Thérèse Wolfenstetter, appeared to be highly selective for protons compared to all the tested ions, with no obvious differences. However, a more detailed quantification comparing these ions would certainly be interesting. Based on my previous measurements, I expected  $V_{rev}$  to be slightly negative under symmetrical pH conditions ( $\Delta pH = 0$ ) (see Figure 3-9b). In order to still calculate accurately, I measured  $V_{rev}$  before the addition of  $Na^+$  and corrected the  $V_{rev}$  measured upon the addition of  $Na^+$  by this value.  $V_{rev}$  can then be used to calculate the relative permeability of protons compared to Na by rearranging Eq. 3 to:

$$\frac{P_{H^+}}{P_{Na^+}} = \frac{[Na^+]_o}{e^{\frac{V_{rev}F}{RT}} [H^+]_i - [H^+]_o} \quad \text{Eq. 4}$$

The result is a permeability ratio  $\frac{P_{H^+}}{P_{Na^+}}$  of  $3.01 \times 10^6$ , i.e. drHNCL1 is approx. 3 million times more selective for protons than for  $Na^+$ .

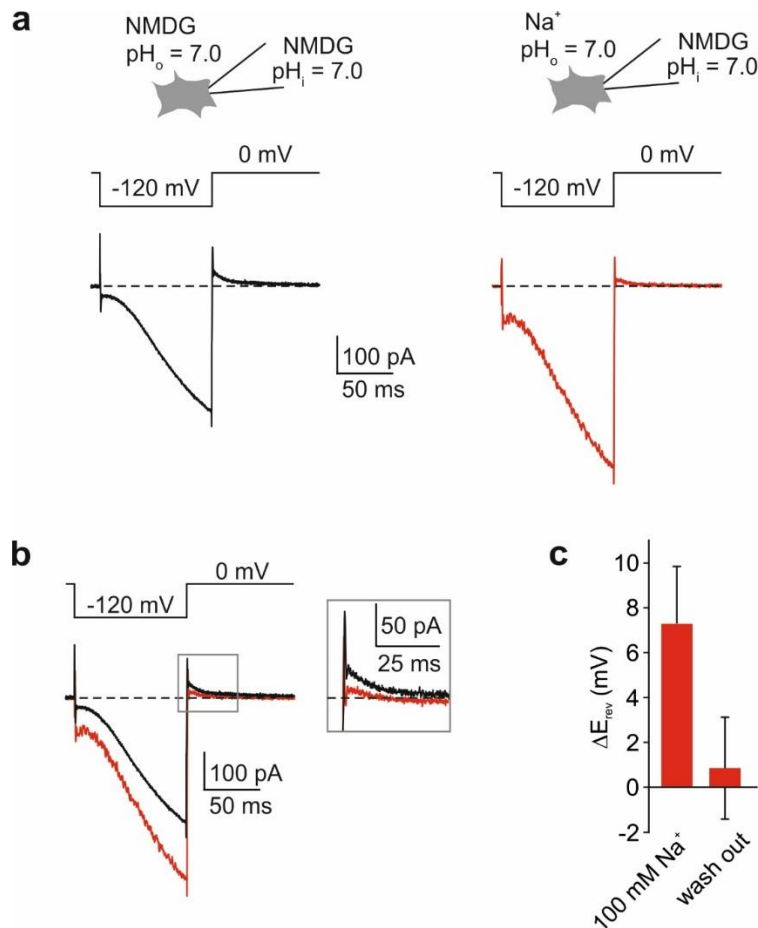


**Figure 3-10:  $V_{rev}$  of drHCNL1 shifts upon addition of  $Na^+$ .** **a**, Whole-cell patch-clamp recording of a drHCNL1-expressing CHO before (black) and after addition of 100 mM  $Na^+$  (red). **b**, Overlay of the two traces shown in (a). Inset shows magnified tail currents. Note the change in tail currents from clearly outward to almost 0 despite large current during activation. **c**, Change in  $V_{rev}$  upon addition of 100 mM  $Na^+$  and after wash-out. Error bars denote standard deviation.

Next, I wanted to use this value to compare drHCNL1 to  $H_v1$ , the only other voltage-gated proton channel that is currently known. As of yet, no exact value regarding the selectivity of  $H_v1$  has been published. During my master thesis, I used a fluorometric approach to compare drHCNL1 with  $H_v1$  directly. In this assay, drHCNL1 was 3-4 times less selective than  $H_v1$  (56). Based on the permeability ratio  $\frac{P_{H^+}}{P_{Na^+}}$  for drHCNL1, we estimate  $\frac{P_{H^+}}{P_{Na^+}}$  for  $H_v1$  to be approx.  $9 \times 10^6 - 1.2 \times 10^7$ .

## 3.4 Permeation pathway in drHCNL1

### 3.4.1 Sequence comparison of HCNL1 and classical HCN channels

In the previous chapter, I have demonstrated that HCNL1 is highly selective for protons. By contrast, classical HCN channels are moderately  $K^+/Na^+$  selective and do not conduct protons (Figure 3-7). Therefore, I examined which changes are responsible for this remarkable proton selectivity.

First I compared the amino-acid sequence of the prototypical pore region (Figure 3-11). In voltage-gated ion channels (with the exception of the depolarization-activated proton channel  $H_v1$ ), ions are conducted through the PD, in which a short sequence between S5 and S6 represents the selectivity filter of the pore (51,108,109). In  $K^+$  channels, this selectivity filter is formed by five amino acids; of these, the first two are different between the different channels, whereas the last three always consist of the sequence GYG. In HCN channels, the selectivity filter sequence is CIGYG and is highly conserved among different HCN channels. DrHCNL1 lacks the CIGYG motif, and the corresponding string of amino acids is not conserved among HCNL1 channels from different species (WPFLE in *D. rerio*, WISTK in *C. auratus* and *C. carpio*, WISTN in *S. anshuiensis*) (Figure 3-11). Mutations of the CIGYG motif in HCN channels result in non-conducting channels (49,50), suggesting that the HCNL1 pore might be corrupted and non-functional.

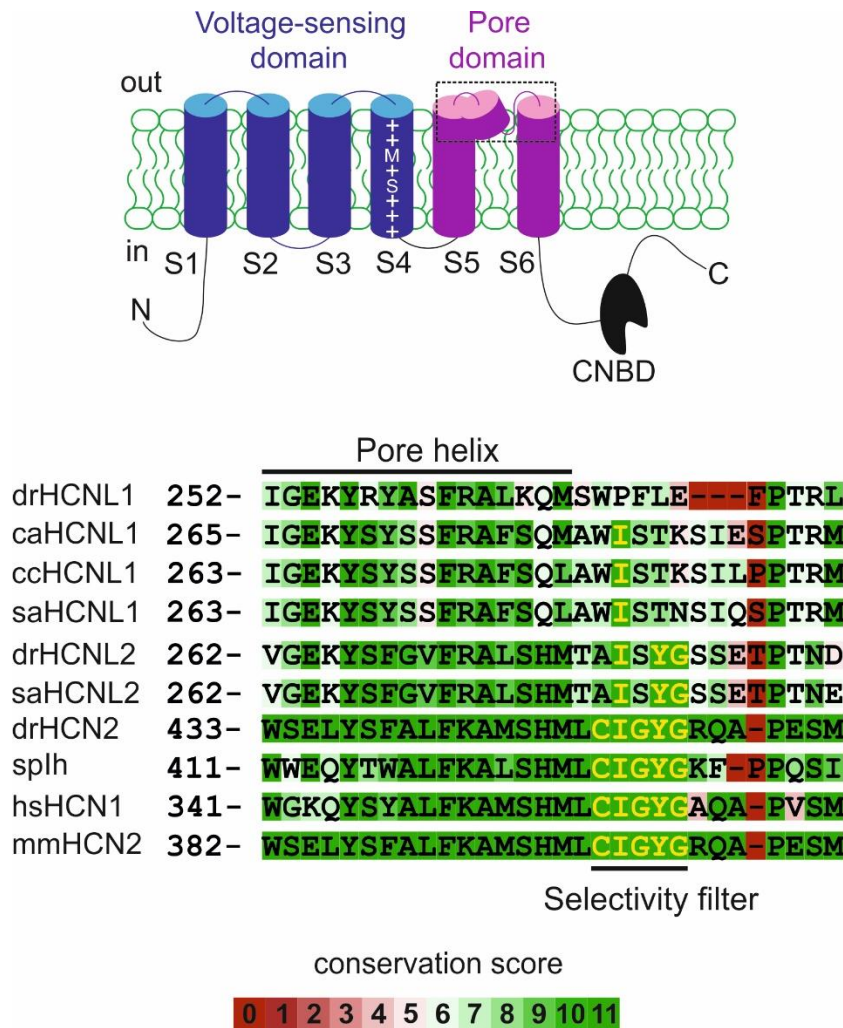


**Figure 3-11: Comparison of the PD of HCNL and classical HCN channels.** Sequence alignment of the PD of several HCNL and classical HCN channels. Sequences are sourced from NCBI (accession numbers see Figure 6-1). Sequences are underlaid with their conservation score in reference to hsHCN2 (95). Conserved amino acids of the selectivity filter are highlighted in yellow.

The second notable alteration is in the VSD (Figure 3-12). Here, the S4 segment is a highly conserved feature; it is conserved among the classical HCN channels (paralogously, i.e. HCN1-4) across different species (orthologously) and also remains largely unchanged in HCNL1 and HCNL2 channels. It features a string of up to eight regularly spaced Arg residues that is interrupted at the fifth position by a Ser residue. This interrupting Ser residue is also present in HCNL1/2. Strikingly, in HCNL1/2 channels, but not in classic HCN channels, the Arg string is additionally interrupted at the third position by a Met residue (M196 in drHCNL1) (Figure 3-12). In Na<sup>+</sup> and K<sup>+</sup> channels, mutations that introduce gaps in the regular spacing of the S4 Arg residues



Based on this sequence comparison, I hypothesized that the proton permeation pathway of drHCNL1 involves the VSD and not - like in typical voltage-gated ion channels - the PD. Alternatively, HCNL1 might entertain two pores, the VSD for protons and the classical pore region for other ions. I tested this hypothesis by the following three experimental approaches.

### **3.4.2 Blockers of VSD and PD**

First, I followed a pharmacological approach using two different blockers that target either the PD or the VSD (Figure 3-13). As a PD blocker, I used ZD7288, an open-channel blocker of classical HCN channels. The compound enters the pore in the open state from the intracellular side and thus blocking ion currents. Several hydrophobic amino-acid residues have been identified that are crucial for ZD7288 binding, all of which are conserved in drHCNL1 (Figure 3-13)(115).

As a blocker of the VSD, I used 5-chloro-2-guanidinobenzimidazole (ClGBI), a membrane-permeable congener of 2-guanidinobenzimidazole (2GBI). 2GBI is an open-channel blocker of H<sub>v</sub>1(116,117) that also occludes the open state of the VSD from the intracellular side.

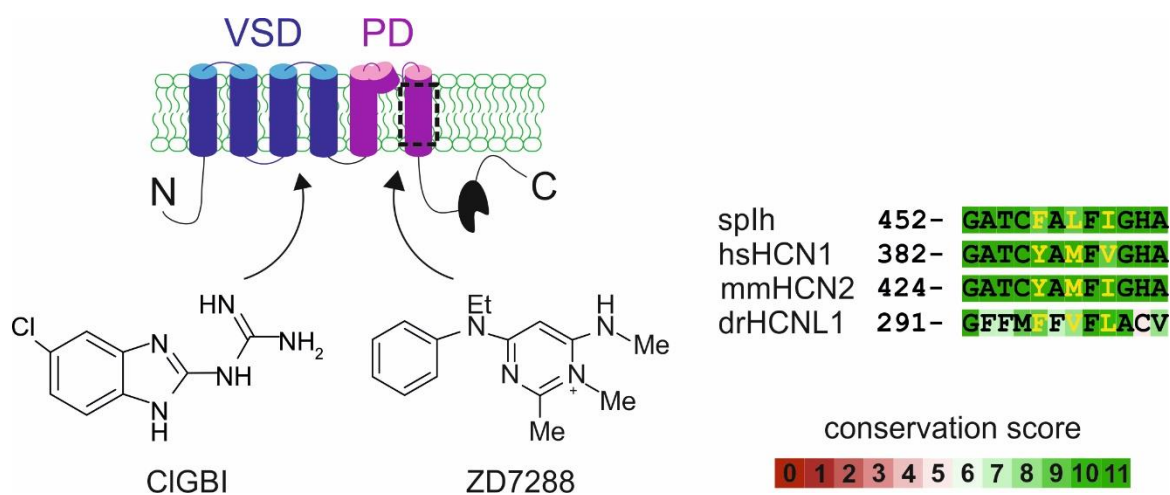


**Figure 3-13: Target sites of ClGBI and ZD7288.** Structures of the two compounds. The arrows indicate their respective site of binding and inhibition. The alignment on the right shows a section of S6 of several HCN channels and drHCNL1. Amino acids involved in binding of ZD7288 highlighted in yellow. Sequences are sourced from NCBI (accession numbers see Figure 6-1). Sequences are underlaid with their conservation score in reference to hsHCN2 (95).

MmHCN2, a classical HCN channel that conducts ions through its pore domain, was blocked by ZD7288 but not by ClGBI (Figure 3-14a). By contrast, drHCNL1 was blocked by ClGBI but not ZD7288, suggesting that drHCNL1 contains a pore in the VSD (Figure 3-14b). Thérèse Wolfenstetter studied the interaction of GBI compounds with drHCNL1 in more detail. She was able to show that both 2GBI and ClGBI blocked drHCNL1 currents in a dose-dependent fashion (57,58).

In  $H_v1$ , the mutation of a phenylalanine (Phe150) to alanine (Ala) in the gating-charge transfer center (GTC, see Chapter 1.3.1) increases the blocking efficacy of 2GBI (116), whereas the corresponding mutation F96A in drHCNL1 lowered the efficacy in experiments performed by Thérèse Wolfenstetter. This result suggests that in both channels, the gating-charge transfer center participates in the binding of 2GBI (57,58), but the effects are different. I suggest that GBI compounds block currents through drHCNL1 by occluding a proton permeation pathway in the VSD.

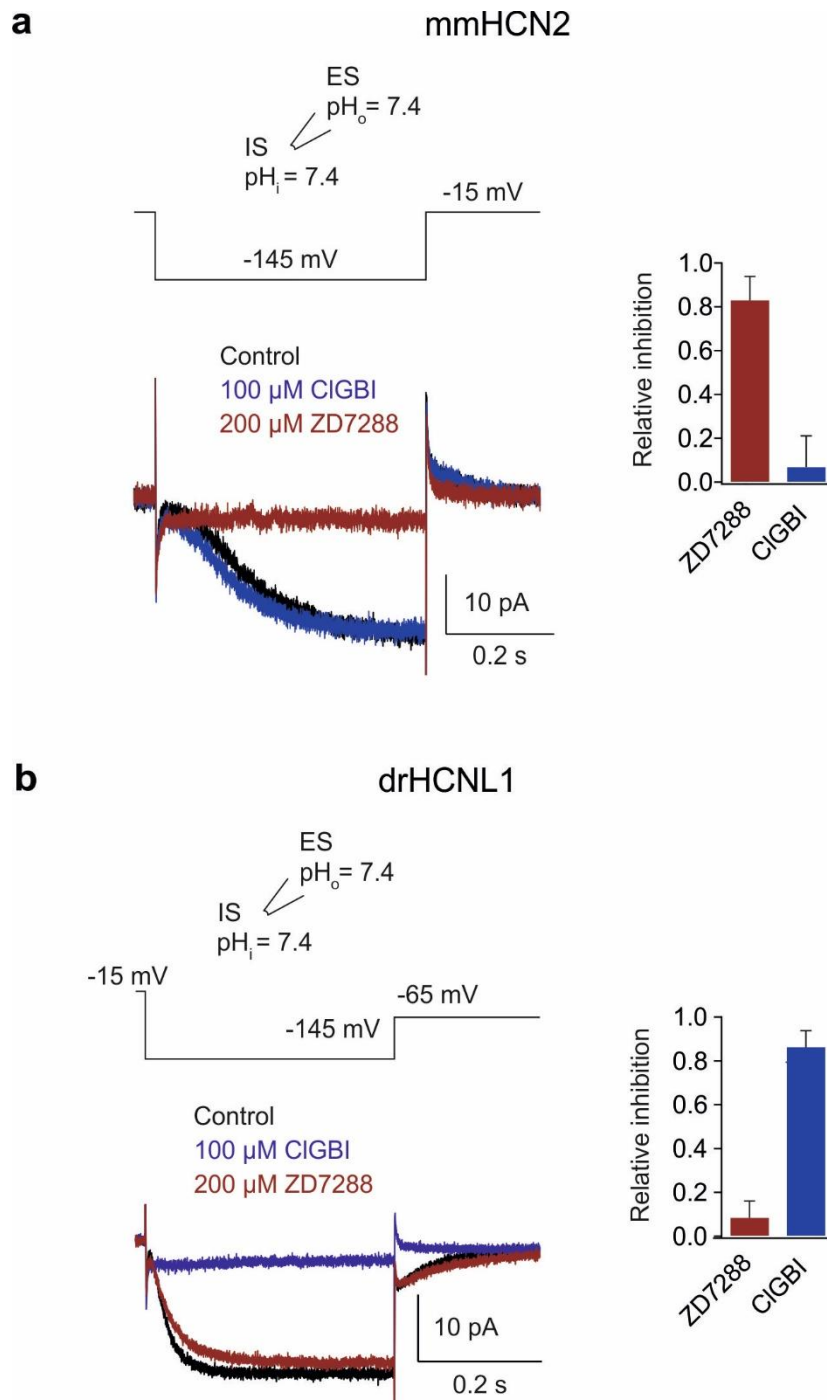


**Figure 3-14: Blockers of the VSD, but not of the PD, inhibit HCN1.** **a**, Excised inside-out patch-clamp recording from a mmHCN2-expressing HEK cell presence or absence of 100  $\mu\text{M}$  CIGBI (blue) or 200  $\mu\text{M}$  ZD7288 (dark red). Bar graph shows the mean relative inhibition in response to ZD7288 and CIGBI. Error bars denote standard deviation. **b**, Excised inside-out patch-clamp recording from a drHCN1-expressing CHO cell. Color-coding and bar graph like in (a).

### 3.4.3 Truncation and mutation of the PD

Second, I created a number of mutants to probe the function of the PD. Different mutants lacking the PD (either due to deletion of the PD or truncation before or within the PD) were not functional, neither when tested for proton conductance with “proton channel” solutions (Chapter 3.3.1) nor in physiological solutions (Figure 6-2). I also tested several chimeric constructs in which parts of the PD were replaced by sequences from classical HCN channels (in their wildtype state as well as containing previously characterized mutations abolishing currents through the pore). These were also non-functional (Figure 6-3).

Therefore, I chose a less invasive strategy: In HCN channels, replacing the canonical selectivity filter GYG by AAA creates non-conducting, dominant-negative channel mutants (49). In drHCNL1, the GYG motif is not conserved, and the amino-acids at the respective positions are FLE (positions 271-273, Figure 3-11). Whether these amino acids form a conducting pore is not known. Therefore, we introduced into drHCNL1 the AAA mutation in order to generate mutant (drHCNL1-AAA) that is congruous to the HCN-AAA mutant (Figure 3-15). This mutant should have a non-conducting pore in the PD; a potential pore in the VSD should not be affected by the mutation. The drHCNL1-AAA mutant was functional and produced currents similar to those of wildtype drHCNL1 in “proton channel” solution (Chapter 3.3.1). The large currents in the absence of alkali-metal ions indicates that this mutant channel also conducts protons. Because wildtype and mutant currents have similar properties, I also conclude that the mutation did not affect the proton pore of drHCNL1.

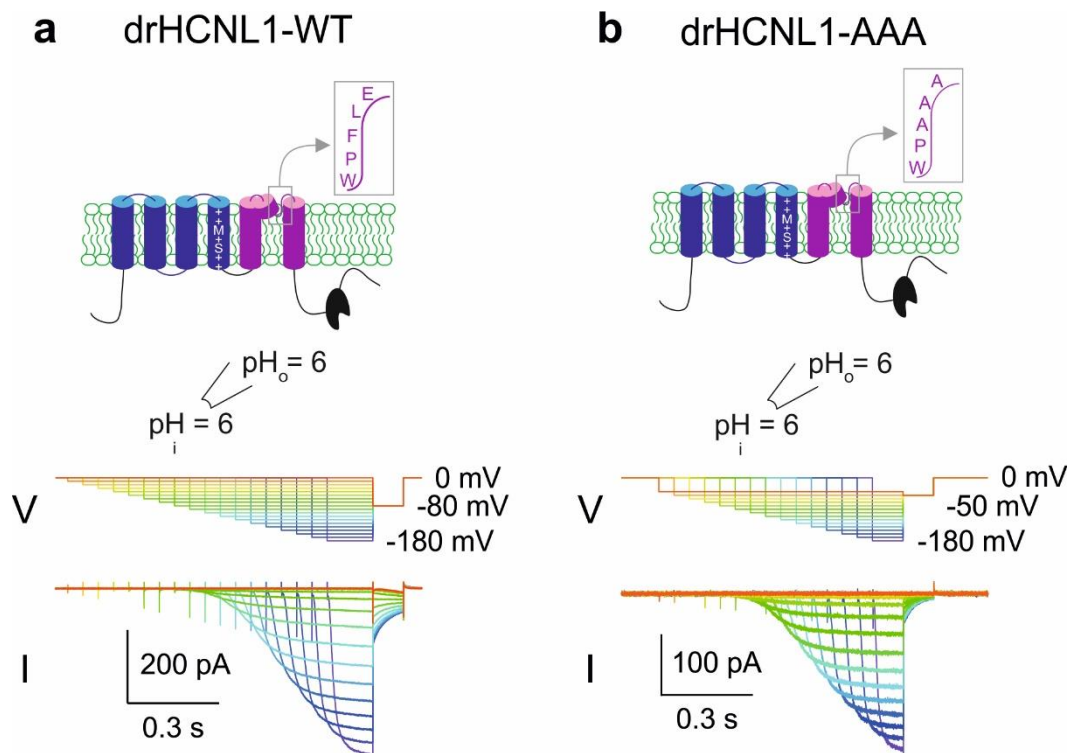


**Figure 3-15: DrHCNL1-AAA currents are similar to drHCNL1-WT currents.** **a**, Excised inside-out patch-clamp recording from *X. laevis* oocytes expressing drHCNL1 **b**, Excised inside-out patch-clamp recording from *X. laevis* oocytes expressing drHCNL1-AAA

Additionally, like for drHCNL1-WT, the reversal potential of drHCNL1-AAA closely followed the Nernst potential for protons and did not change upon the addition of several different alkali-metal ions (Figure 3-16). From these experiments I conclude the following: the AAA-mutation is functional and the selectivity for protons is preserved; therefore, the PD is not involved in the permeation of protons in drHCNL1.

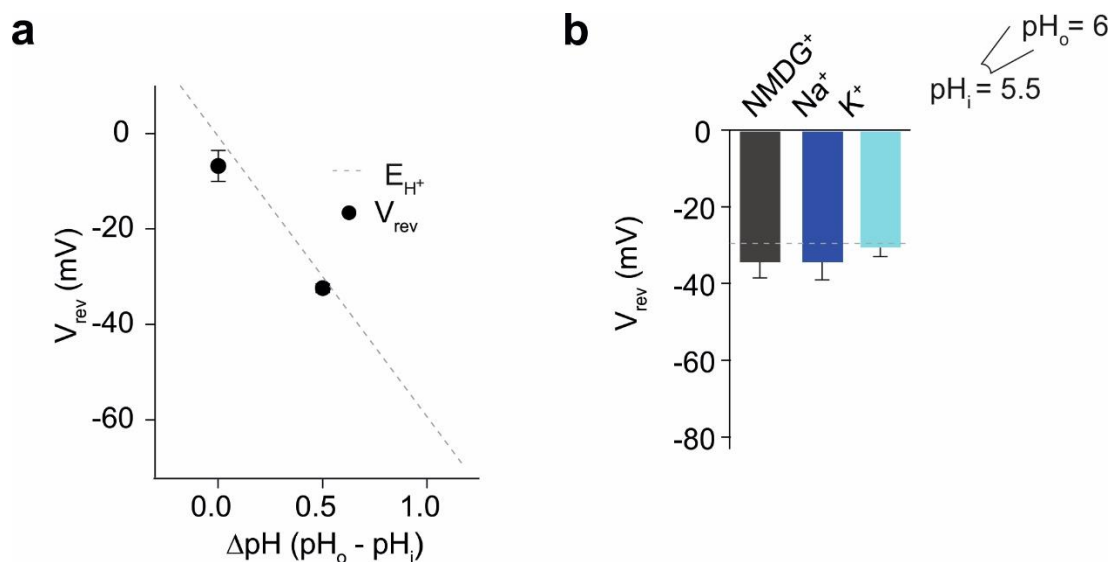


**Figure 3-16: DrHCNL1-AAA is also selective for protons.** **a**,  $V_{rev}$  of currents from HCNL1-AAA as a function of  $\Delta pH$  ( $\Delta pH = 0$ :  $V_{rev} = -6.8 \pm 3.3$  mV,  $n = 5$ ;  $\Delta pH = 0.5$ :  $V_{rev} = -32.4 \pm 0.9$  mV,  $n = 5$ ). Dashed line represents  $E_{H^+}$ . **b**, Effect of bath application of various cations (90 mM) on  $V_{rev}$  with  $pH_i = 5.5$  and  $pH_o = 6$  ( $E_{H^+} = -29.3$  mV), measured in excised inside-out patches from *X. laevis* oocytes expressing HCNL1-AAA (NMDG<sup>+</sup>:  $-34.6 \pm 3.9$  mV,  $n = 5$ ; Na<sup>+</sup>:  $-34.6 \pm 4.4$  mV,  $n = 5$ ; K<sup>+</sup>:  $-30.8 \pm 2.2$  mV,  $n = 5$ ). Error bars denote standard deviation.

### 3.4.4 Mutation of M169 in the S4 motif of the VSD

Third, I tested the hypothesis that the additional gap M169 in the string of regularly spaced Arg residues of the S4 segment created the proton permeation pathway. During my master thesis, I generated a mutant where M169 is replaced by an Arg (M169R) to remove the gap and to restore the charge distribution of classic HCN channels that do not transport ions via S4 (Figure 3-12)(56).

In inside-out patches of *X. laevis* oocytes, this mutant produced only small transient currents. The amplitude of these currents was much smaller than that of the currents we routinely obtain for wildtype drHCNL1 (Figure 3-17). Low expression of the mutant was not responsible for the small currents, because GFP-tagged variants of wildtype and M169R channels displayed similar expression levels in patch-clamp fluorometry (58).

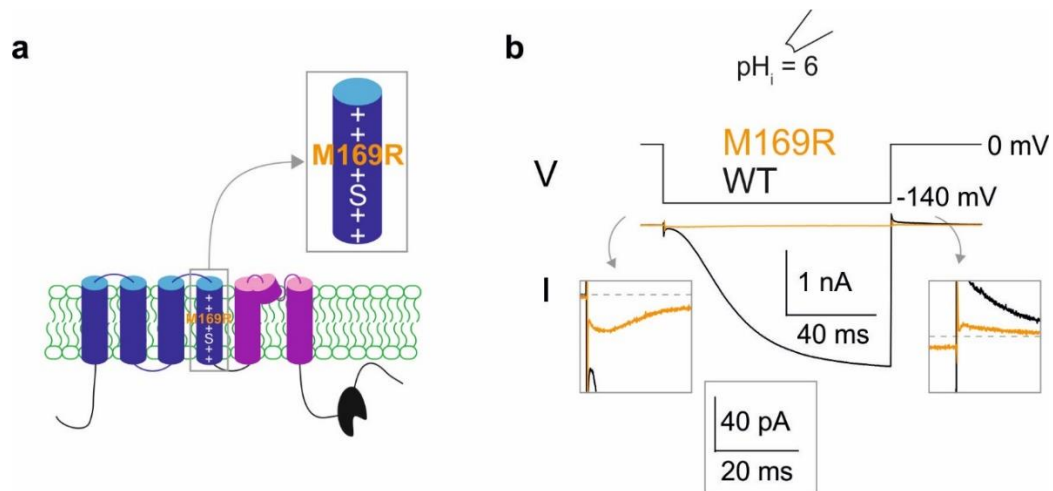


**Figure 3-17: Mutation of M169 to R greatly diminishes drHCNL1 current** **a**, Cartoon visualizing the position of the M169R mutation. **b**, Excised inside-out patch-clamp recordings from *X. laevis* oocytes expressing wildtype drHCNL1 (black) or mutant drHCNL1-M169R (orange). Insets show an amplified section of the recording at the beginning and the end of the activating voltage pulse where the M169R displays small, transient currents. This data was obtained by Thomas Berger.

Unfortunately, when the M169R mutant was expressed in *X. laevis* oocytes and measured in excised patches, we could not reliably measure currents that were large enough to analyze. However, when the M169R mutant was expressed in CHO cells, I was able to routinely measure currents in whole-cell recordings that were larger and thus suitable for analysis (Figure 3-18a). This provided an opportunity to investigate these currents in more detail. The transient nature of the currents could either reflect fast channel inactivation or it could be indicative of gating currents caused by S4 movement across the electrical field of the membrane (Chapter 1.3.1). To differentiate between these two possibilities, I studied the M169R mutant under symmetric ion conditions: when the channel is briefly activated at -130 mV to reach the peak current amplitude, and then  $V_m$  is stepped to various voltages from -80 mV to +80 mV, it is expected that ionic currents reverse direction at  $V_{rev} = 0$  mV, whereas gating currents should not reverse. Indeed, currents did not reverse at any voltage (Figure 3-18c), a behavior incompatible with ionic currents but consistent with *off* gating currents. Therefore, I conclude that, the M169R mutant is not conducting protons, and that the residual currents are gating currents.

### 3 Results

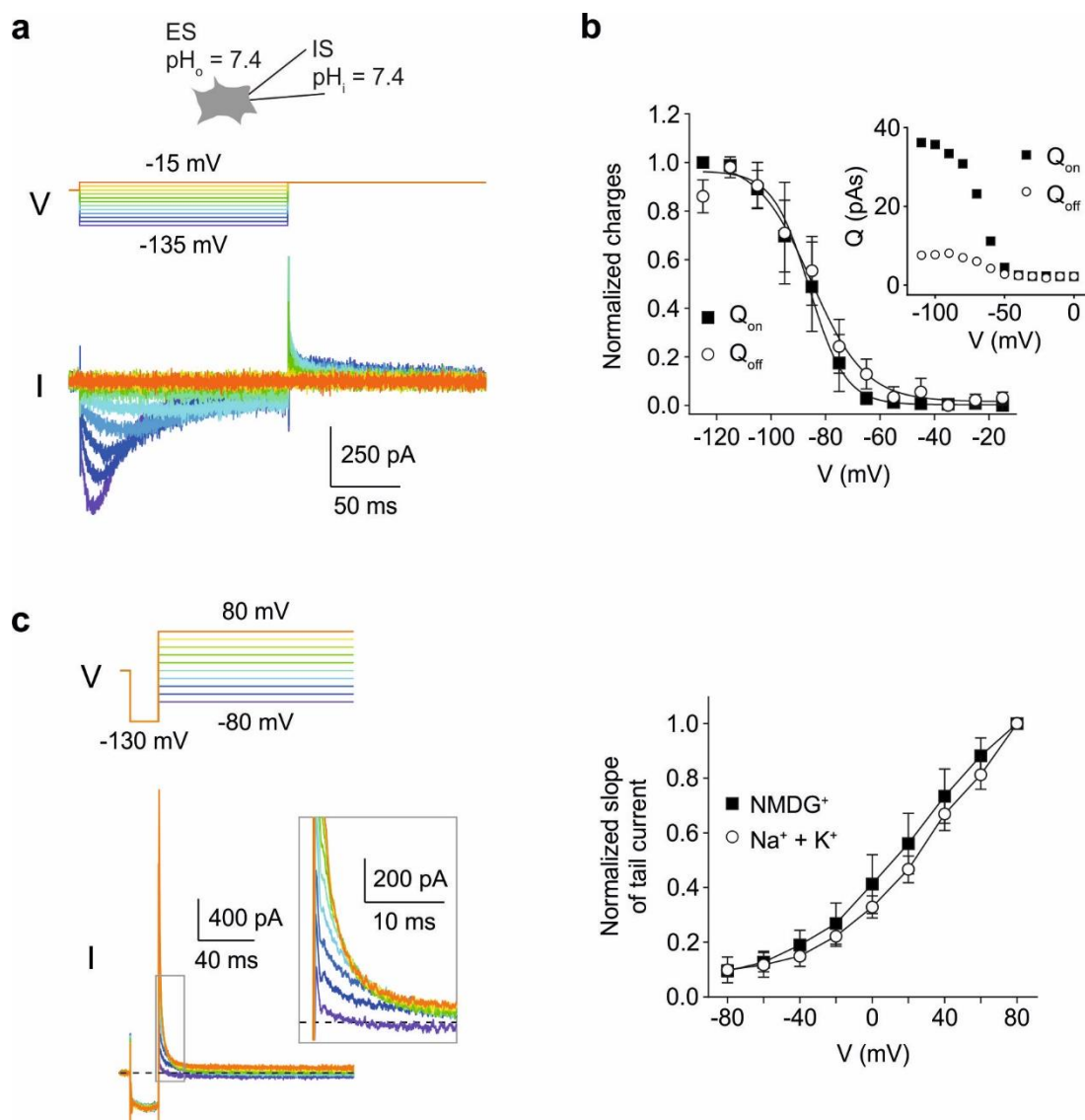


**Figure 3-18: drHCNL1-M169R only produces gating currents** **a**, Whole-cell patch-clamp recording of a CHO cell expressing drHCNL1-M169R. **b**, Normalized charge-voltage relationship (QV) of drHCNL1-M169R derived from (a) (*on*:  $V_{1/2} = -86.4 \pm 5.0$  mV,  $s = 6.7 \pm 0.5$  mV; *off*,  $V_{1/2} = -84.9 \pm 5.6$  mV,  $s = 10.0 \pm 1.6$  mV,  $n = 6$ ). Inset, QV of drHCNL1-M169R showing fourfold larger *on* than *off* currents. **c**, *Left*, whole-cell patch-clamp recording of a CHO cell expressing drHCNL1-M169R. Inset shows magnified tail currents. *Right*, Normalized slopes of drHCNL1-M169R tail currents as a function of the voltage, measured in symmetric NMDG<sup>+</sup>- or Na<sup>+</sup>/K<sup>+</sup>-based solutions. Error bars denote standard deviation

Indeed, the charge-voltage relationships, obtained by integrating *on*- and *off*-gating currents, saturated and their voltage dependence was similar (Figure 3-18b) - two characteristic features of gating currents (1.3.1). Curiously, *on*-gating charges of drHCN1 were much larger than *off*-gating charges. In H<sub>v</sub>1 and *Shaker* K<sup>+</sup> channels, a similar behavior was described and attributed to a phenomenon called “voltage-sensor immobilization” (37,38). During prolonged activation, the voltage sensor enters a more stable conformation from which it recovers only slowly. This immobilization results in an apparent loss of *off*-gating charges relative to *on*-gating charges. Voltage-sensor immobilization is initially small and increases during long stimulation times (37,38). Therefore, I recorded *on*- and *off*-gating currents of drHCN1 for different pulse lengths. For short stimulation times, *on*- and *off*-gating charges were similar (Figure 3-19). With longer stimulation times, the ratio between *off*- and *on*-gating charges decayed exponentially ( $\tau_{\text{decay}} = 50.6 \pm 8.3$  ms,  $n = 5$ , Figure 3-19), which is diagnostic for voltage-sensor immobilization.

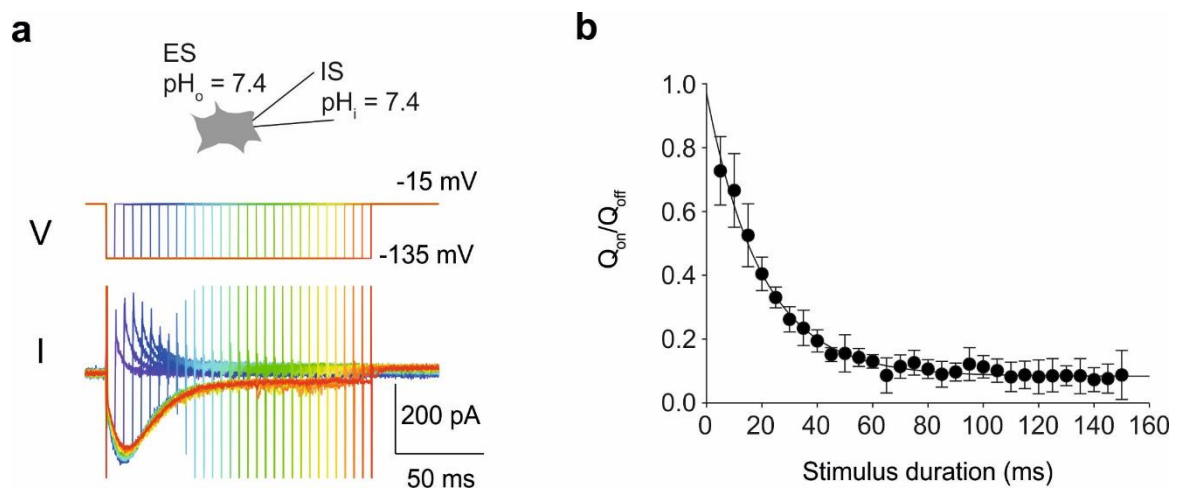


**Figure 3-19: Gating charge immobilization in drHCN1-M169R upon prolonged stimulation** **a**, Whole-cell patch-clamp recording of a CHO cell expressing drHCN1-M169R with increasingly long activation. Note that *off* current initially increase then decrease. **b**, Ratio  $Q_{\text{on}}/Q_{\text{off}}$  as a function of stimulus duration. Data fitted to exponential decay ( $\tau_{\text{decay}} = 50.6 \pm 8.3$  ms,  $n = 5$ ). Error bars denote standard deviation.

The importance of M169 is also supported by a second mutant: M169C (which was created and characterized by Thérèse Wolfenstetter)(57). Here, M169 is changed to cysteine, which can be chemically modified with 2-(trimethylammonium)ethyl methanethiosulfonate (MTSET). Activation of the M169C mutant produced proton currents that were blocked by extracellular MTSET modification, whereas the wildtype drHCNL1 channel was not affected by extracellular MTSET (57). Collectively, these results show that protons pass drHCNL1 via the VSD and M169 lines the proton-permeation pathway; furthermore, the ‘classical’ central pore region of HCNL1 does not pass protons or alkali metal ions.

### 3.5 Heterologous expression of drHCNL2

*D. rerio* has two HCNL channels and I also wanted to study the properties of drHCNL2. Unfortunately, drHCNL2 did not produce currents either in *X. laevis* oocytes or CHO cells. I wanted to determine the reason for the failure to get functional expression. A frequent reason is that, in a heterologous system, channel proteins get synthesized but not properly targeted to the membrane. For this purpose, I created sheets of plasma membrane from transfected CHO cells. Here, the cells are “unroofed” by a short ultrasound pulse, which removes all parts of the cell except the basal plasma membrane that is attached to a glass coverslip. Under normal incubation conditions (37°C), drHCNL1, but not drHCNL2, reached the plasma membrane (Figure 3-20). In the literature it is described that incubating transfected cells at lower temperatures (e.g. 29°C instead of 37 °C) enables proteins to reach the plasma membrane. However, this treatment was not effective for drHCNL2 (Figure 3-20).

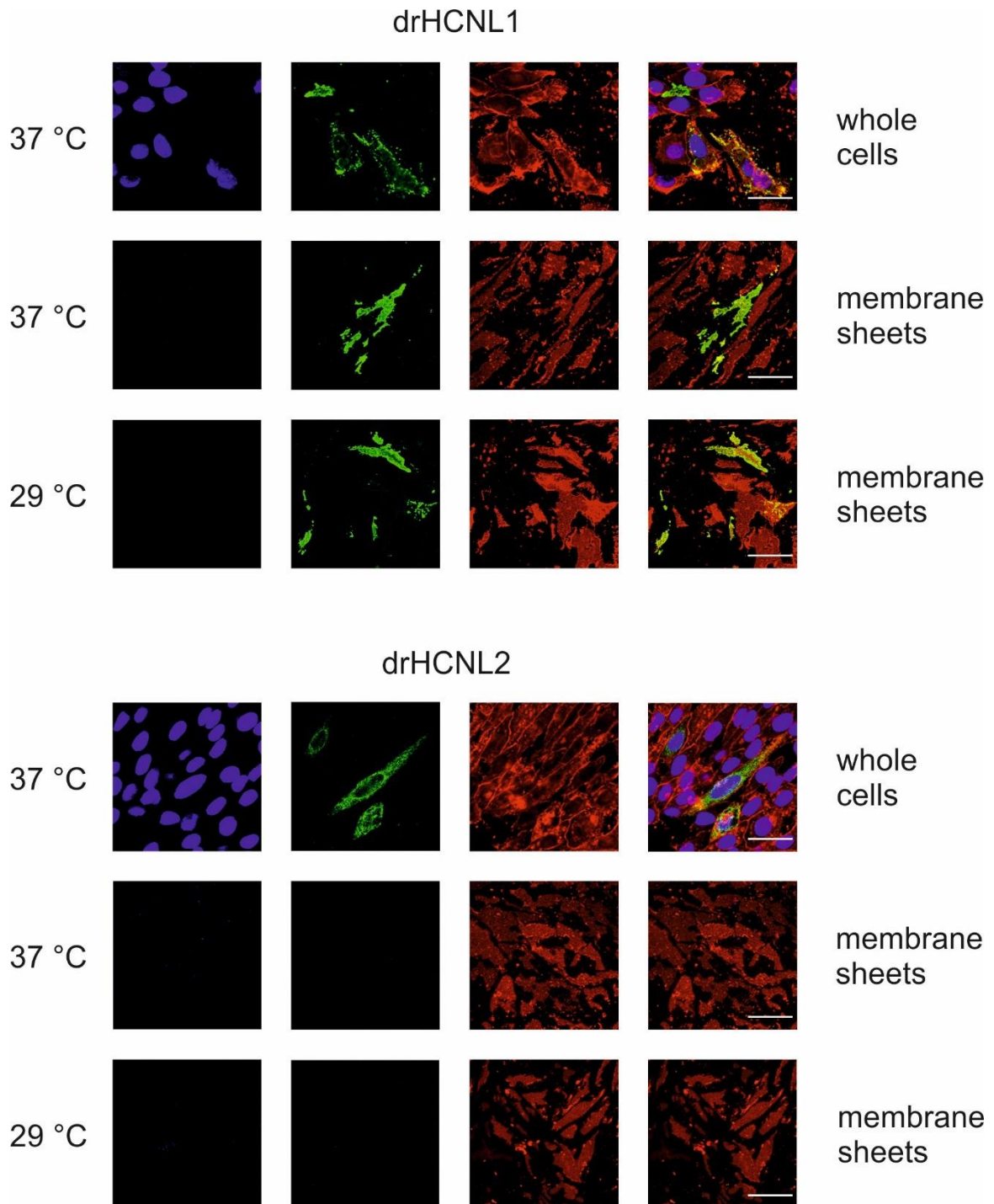


**Figure 3-20: Plasma membrane sheets of CHO cells expressing drHCNL1 or drHCNL2.** Immunocytochemical staining of CHO Cherry-CAAX cells transfected with either drHCNL1 or drHCNL2 (blue: DAPI, green: anti-HA antibody with A488, red: anti-mCherry antibody with Cy3, merge: blue, green and red channel merged). *Upper row:* Whole cells incubated at 37 °C. *Middle row:* Plasma membrane sheets of cells incubated at 37 °C. *Bottom row:* Plasma membrane sheets of cells incubated at 29 °C. Scale bars 50  $\mu$ m.

## 3.6 drHCN1 in zebrafish sperm

### 3.6.1 Electrophysiological recording from *D. rerio* sperm

Having characterized drHCN1 heterologously, I wanted to study it in its native sperm environment. Zebrafish sperm also express a  $K^+$  channel called drCNGK ( $K^+$ -selective cyclic-nucleotide gated channel) that might interfere with the recording of drHCN1 currents. CNGK can be blocked by  $Cs^+$  (18,19); thus, to isolate drHCN1 currents, I measured in solutions that contain  $Cs^+$  instead of  $K^+$  (Chapter 2.8.4). Using the whole-cell patch-clamp technique, I recorded hyperpolarization-activated currents from zebrafish sperm that were very similar to those of heterologously expressed drHCN1: they displayed a similar voltage-dependence ( $V_{1/2} = -105.3 \pm 11.4$  mV,  $s = 13.0 \pm 2.1$ ,  $n = 5$ ) that was also not sensitive to cyclic nucleotides (cAMP:  $V_{1/2} = -100.6 \pm 17.2$  mV,  $s = 11.0 \pm 2.6$  mV,  $n = 4$ ; cGMP:  $V_{1/2} = -110.0 \pm 6.6$  mV,  $s = 10.0 \pm 2.6$  mV,  $n = 3$ , Figure 3-21).

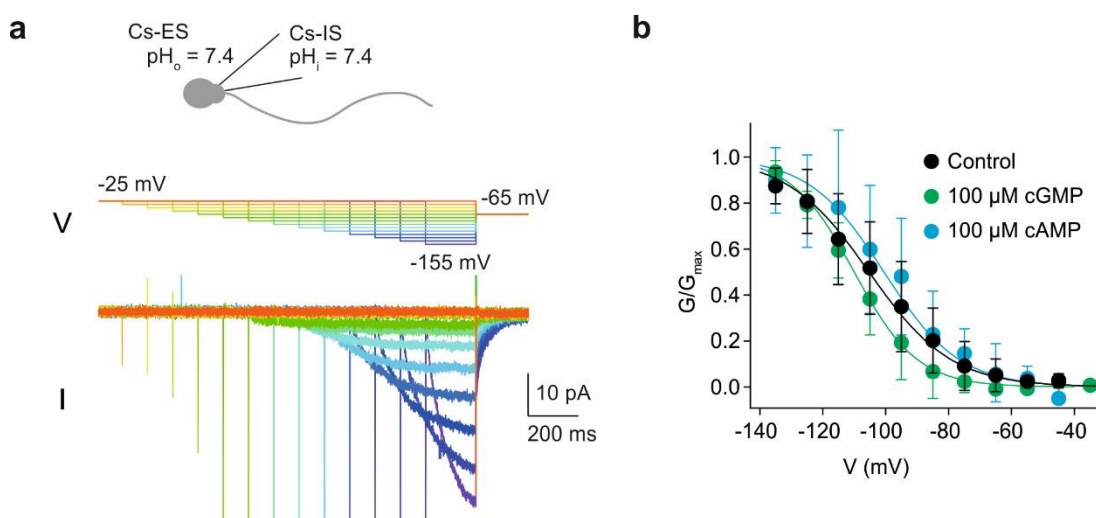


**Figure 3-21: Measurement of drHCN1 in zebrafish sperm.** **a**, Whole-cell patch-clamp recording of hyperpolarization-activated currents from zebrafish sperm in the presence of  $Cs^+$  to block CNGK. **b**, GVs derived from tail currents with or without 100  $\mu$ M cAMP or cGMP in the intracellular solution. Error bars denote standard deviation. Parts of this data set were obtained by Sylvia Fechner and Thomas Berger.

In order to test whether these are indeed proton currents, I used a pH-sensitive dye. Because BCECF has toxic effects on sperm of several species (118,119), I used the dye pHrodo Red, which is red-shifted. Because red-shifted dyes can be excited with light of longer wavelengths, they are seemingly less cytotoxic to cells (120–122). Upon activation of current by hyperpolarization, the fluorescence of pHrodo Red increased ( $\Delta F/F = 5.3 \times 10^{-3} \pm 1.9 \times 10^{-3} \text{ pA}^{-1} \text{ s}^{-1}$ ,  $n = 8$ , Figure 3-22 a), indicating acidification by proton flux into sperm. Finally, ClGBI (100  $\mu\text{M}$ ) - which inhibits drHCN1 (Chapter 0) - blocked the hyperpolarization-activated current in sperm (Figure 3-22b,  $73 \pm 9\%$ ,  $n = 4$ ). These results show that drHCN1 indeed mediates hyperpolarization-activated proton currents in zebrafish sperm.

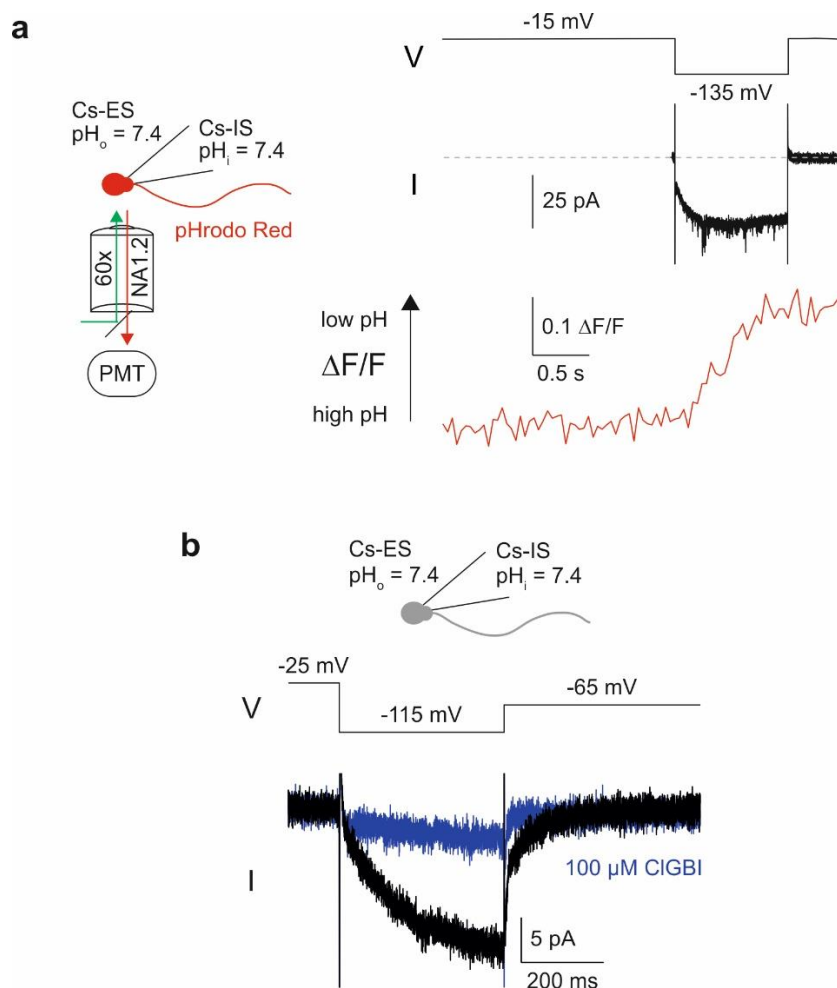


**Figure 3-22: DrHCN1 carries proton currents in sperm.** **a**, Whole-sperm patch-clamp fluorometry recording with the fluorescent pH-indicator pHrodo Red. Upon activation of drHCN1, the fluorescence increases indicating acidification. **c**, Block of hyperpolarization-activated current in zebrafish sperm by 100  $\mu\text{M}$  ClGBI ( $73 \pm 9\%$ ,  $n = 4$ ).

### 3.6.2 Detection of drHCNL1 in *D. rerio* tissue

To identify the drHCNL1 protein in zebrafish tissue and sperm, I used two different monoclonal antibodies, one directed against a C-terminal (anti-C<sub>term</sub>) and one against an N-terminal epitope (anti-N<sub>term</sub>). To test the specificity of the antibodies, I used a version of the drHCNL1 protein with a C-terminal HA-tag (drHCNL1-HA). In Western blots of oocytes injected with drHCNL1-HA, both antibodies stained the same band as an anti-HA antibody, whereas no band was detected in uninjected control oocytes (Figure 3 23a). The apparent molecular weight ( $M_w$ ) of this band was approx. 62 kDa, which matches the calculated  $M_w$  for drHCNL1-HA of 60.4 kDa (Figure 3 23a, black arrow). This result demonstrates that the antibodies are indeed specific for drHCNL1.

The antibodies also recognized a smear between 65-75 kDa (Figure 3-23a, red arrow). Upon treatment with peptide:N-glycosidase (PNGase) - an enzyme that deglycosylates proteins -, the smear collapsed into a single 62-kDa band, suggesting that drHCNL1 is glycosylated (Figure 3-23b).

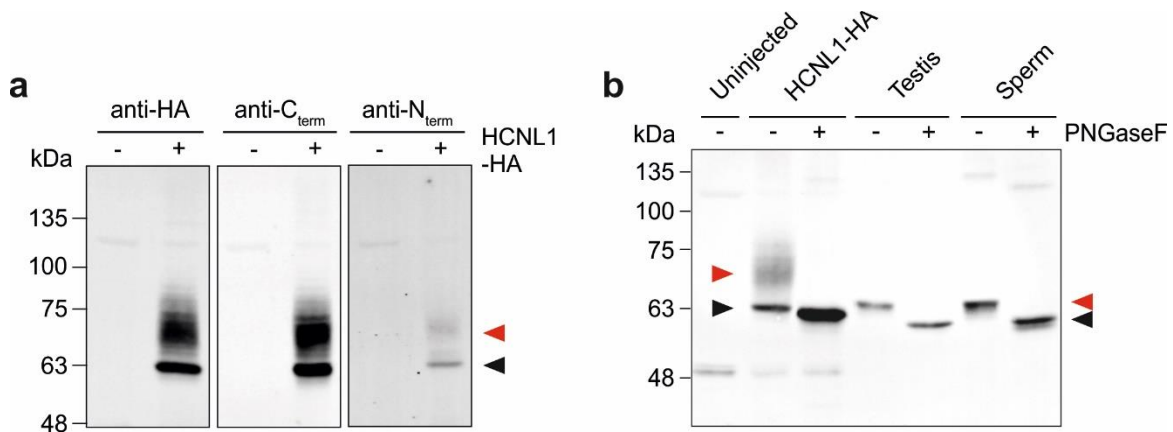


**Figure 3-23: Monoclonal antibodies recognize drHCNL1 in zebrafish tissue and sperm. a**, Western blot of uninjected *X. laevis* oocytes (-) or expressing drHCNL1-HA (+) stained with an HA antibody, an anti-C<sub>term</sub>, or anti-N<sub>term</sub> antibody against drHCNL1. Molecular weight standards are indicated on the left. Black arrow indicates a band of expected  $M_w$  (~62 kDa) for drHCNL1. Red arrow indicates a smear of glycosylated drHCNL1. **b**, Western blot of uninjected *X. laevis* oocytes, oocytes expressing HCNL1-HA, testis tissue, and sperm with or without treatment with PNGaseF stained with the anti-C<sub>term</sub> antibody. Red arrow indicates glycosylated drHCNL1 of higher molecular weight and black indicates deglycosylated drHCNL1.

When applied to protein extracts from various zebrafish tissues, the anti-C<sub>term</sub> antibody detected drHCNL1 protein in testis and in sperm (Figure 3-23b), but not in ovary, eyes, and brain (58). Because the drHCNL1 in *X. laevis* oocytes is glycosylated, I tested whether the native drHCNL1 in zebrafish sperm is also glycosylated. Applying PNGase to testis and sperm lowered the M<sub>w</sub> of drHCNL1, suggesting that native drHCNL1 is also glycosylated (Figure 3-23b).

Next, I studied the cellular distribution of HCNL1 in sperm by immunocytochemistry (ICC). I first tested the suitability of monoclonal antibodies on CHO cells. Cells expressing drHCNL1-HA and wildtype cells were mixed; the drHCNL1-HA-expressing cells will be stained by the anti-HA antibody, whereas the others will not. If the monoclonal antibodies are specific they should only stain those cells that are also stained by the anti-HA antibody. This expectation holds true for both monoclonal antibodies, indicating that they are indeed specific for drHCNL1 and suitable for ICC (Figure 3-24a,b). The sperm head was strongly stained, whereas the flagellum was only weakly recognized (Figure 3-24c,d), suggesting drHCNL1 is predominantly localized to the head. This result is also supported by electrophysiological recordings: the amplitudes of currents recorded from isolated sperm heads and from whole sperm were similar (58). This finding is remarkable as drCNGK, the only other ion channel identified in zebrafish sperm, is also localized to the head (18,19).

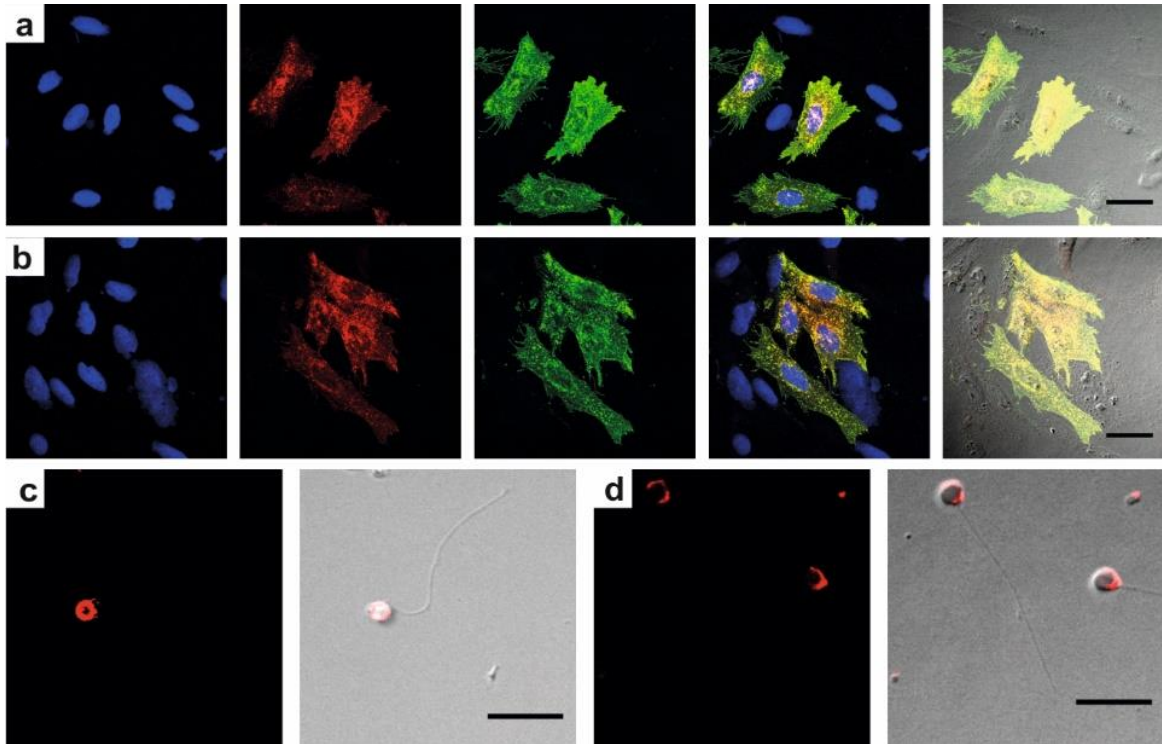


**Figure 3-24: drHCNL1 localizes to zebrafish heads.** **a, b**, Immunocytochemical staining of a mixture of control and zebrafish HCNL1-HA-expressing CHO cells (blue, DAPI; red in (a) row, anti-C<sub>term</sub> antibody with Cy3; red in (b) row, anti-N<sub>term</sub> antibody with Cy3; green, mouse anti-HA antibody with A488; merged fluorescence channels; Cy3 and A488 merged with bright field illumination). Scale bars 25  $\mu\text{m}$ . **c, d**, *Left*, Immunocytochemical staining of zebrafish sperm using the anti-C<sub>term</sub> (c) or the anti-N<sub>term</sub> (c) antibody. *Right*, same staining as in the left panels, overlaid with bright-field illumination. Scale bars 10  $\mu\text{m}$ .

Classical HCN channels are composed of four subunits that form a single pore (25,46), whereas Hv1 forms a dimer (123,124) with two proton pores (87) (Figure 3-25b). Given the high sequence similarity of drHCNL1 and HCN channels, it seems plausible that drHCNL1 also forms tetramers. An experimental approach to probe the multimerization of a protein is chemical cross-linking. For this purpose, a protein solution is incubated with a cross-linking agent. If the protein forms multimers, the subunits are chemically cross-linked. In Western blots of chemically cross-linked drHCNL1, protein bands were detected at approx. 60 kDa, 120 kDa, 180 kDa, and 240 kDa (Figure 3-25a). The apparent  $M_w$  of the different cross-linked species are multiples of the monomer, suggests a tetrameric organization. Because a tetramer has four VSDs, each drHCNL1 channel probably carries four pores (Figure 3-25b).

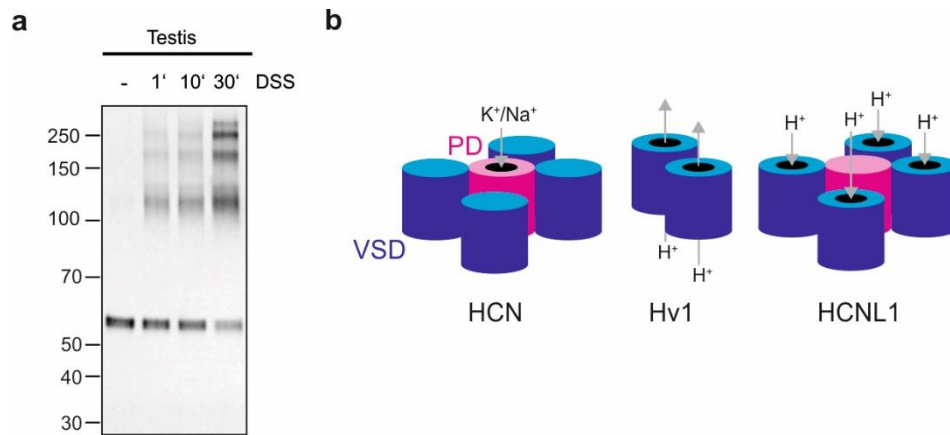


**Figure 3-25: DrHCNL1 forms tetramers.** **a**, Western blot of zebrafish testis incubated in the amino-specific crosslinker DSS for increasing times using the anti-C<sub>term</sub> drHCNL1 antibody. Western Blots were obtained by Sybille Wolf-Kümmeth. **b**, Cartoons illustrating the ion-permeation pathways in HCN, H<sub>v</sub>1, and HCNL1 channels.

### 3.6.3 pH-fluorometry in *D. rerio* sperm

Finally, I addressed the physiological role of HCNL1 in zebrafish sperm. Remarkably, the K<sup>+</sup>-selective drCNGK channel is pH-sensitive (18,19) and drHCNL1 carries protons. These properties of drCNGK and drHCNL1 predict a tight functional relationship (Figure 3-26a): The drCNGK channel is pH-dependent (its open probability is increased at higher pH<sub>i</sub> values) and controls the membrane potential in zebrafish sperm depending on the extracellular K<sup>+</sup> concentration (18,19). This has been demonstrated using the voltage-sensitive dye di-8-ANEPPS (18): When external K<sup>+</sup> is high, like in the seminal fluid of most freshwater fish species (125), the membrane potential is depolarized (Figure 3-26b); when the external K<sup>+</sup> is low, like in freshwater, the membrane potential is more hyperpolarized (Figure 3-26b)(18). Thus, hyperpolarization in freshwater by drCNGK activates drHCNL1. The proton influx through drHCNL1 in turn decreases pH<sub>i</sub> and thus lowers the open probability of drCNGK. This reciprocal interaction of the two channels creates a feedback-loop (Figure 3-26a).

I wanted to show directly that hyperpolarization by drCNGK activates drHCNL1. To this end, sperm were loaded with pHrodo Red to monitor proton influx through drHCNL1 and then superfused with a solution of very low K<sup>+</sup> concentration (40 μM)

### 3 Results

to mimic the  $K^+$  concentration of freshwater. Under these conditions, drCNGK should strongly hyperpolarize sperm and thus activate drHCNL1 and eventually result in proton influx and intracellular acidification. Indeed, when switching to the low- $K^+$  solution the fluorescence of pHrodo Red increased, indicating acidification ( $8.8 \pm 5.1\% \Delta F/F_0$ ,  $n = 22$ ) (Figure 3-26 c). The proton inward current both causes a depolarization and an acidification, which eventually downregulates drCNGK and prevents further hyperpolarization. Thus, the function of drHCNL1 in zebrafish sperm appears to be similar to that of classic HCN channels, i.e. to limit hyperpolarization and initiate recovery from it.

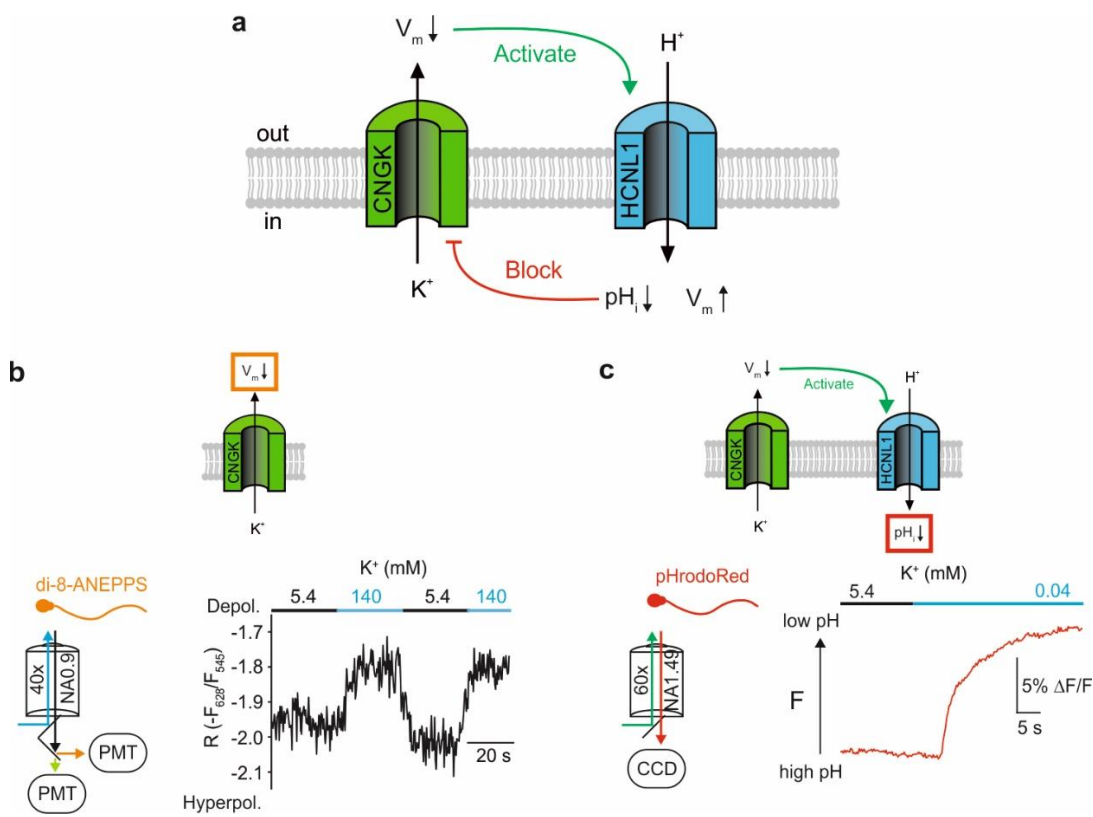


**Figure 3-26: Functional interplay of drCNGK and drHCNL1** **a**, Cartoon of the putative interplay between drCNGK and drHCNL1 channels. **b**, Fluorescence recording of zebrafish sperm loaded with the fluorescent voltage-sensitive dye di-8-ANEPPS, superfused with either regular ES (5.4 mM  $K^+$ , indicated by black bars) or with ES containing 140 mM  $K^+$  (indicated by blue bars). Adapted from (18). **c**, Fluorescence recording of a single zebrafish sperm cell loaded with the fluorescent pH-indicator pHrodo Red, superfused with regular ES (5.4 mM  $K^+$ , indicated by black bars), followed by wash-in of an ES containing 0.04 mM  $K^+$  (indicated by blue bars). Fluorescence increases, indicating intracellular acidification. The data in (b) was gathered by Sylvia Fechner and was already published in (18).

Upon spawning into freshwater, sperm are exposed to two stimuli that both appear to be involved in the activation of motility: a drop in the extracellular  $K^+$  concentration and a drop in osmolarity (referred to as hypoosmotic shock)(4). In the previous experiment, I have addressed only the former, i.e. the drop in  $K^+$  concentration with the osmolarity remaining constant. In our lab group, we also wanted to investigate whether drHCNL1 also plays a role when sperm experience a drop in osmolarity. For this purpose, Thomas Berger and Reinhard Seifert emulated the hypoosmotic shock by rapid mixing of zebrafish sperm in a stopped-flow device. Challenging sperm with a hypoosmotic shock triggered a decrease of  $pH_i$  (58). While it remains unknown by which mechanism this effect is mediated, the change in  $pH_i$  indicated that drHCNL1 could be involved.

## 4 Discussion

---

Three proton channels have been identified so far: H<sub>v</sub>1 and Otopetrin in eukaryotes (85,86,126), and M2 in the influenza virus (127,128); only H<sub>v</sub>1 is voltage-activated. HCNL1 is the founding member of a novel family of hyperpolarization-activated channels that are highly selective for protons.

Although the HCNL1 channel is highly homologous to classical HCN channels, two small modifications have completely changed its physiology. First, the PD of the channel carries amino acids that cannot form a functional pathway that conducts alkali ions. The central pore, which allows ion permeation in all other members of voltage-gated ion channels, is non-functional in HCNL1 and the crucial GYG motif is completely lacking (49,50). Second, the replacement of an arginine residue that is present in the S4 segment of all classic HCN channels by methionine (M169 in drHCNL1) endows HCNL1 with proton permeability.

How do protons pass through the VSD? It may not seem obvious that ions could pass through a protein domain other than the pore. After all, the pore domain features several specific structural properties designed to conduct ions. However, the VSD and the pore are actually similar in several respects. During gating, the charged amino acid residues in S4 must move in the membrane when the electric field is changing (34). To do so, the charged amino acids must cross the hydrophobic environment of the membrane, similar to the way ions flow through the pore. To solve this problem, the VSD has developed several structural features that are reminiscent of PD properties. The VSD adopts an hourglass shape with a central hydrophobic constriction site (HCS) formed by hydrophobic residues from S1-S3 (Figure 4-1)(34,42,45,129–131). The HCS separates the extracellular and the intracellular volume with aqueous clefts above and below (130,132,133). In order to pass from the extracellular to the intracellular side of the membrane, the basic amino acids in S4 must cross the HCS. This transition is facilitated by a specific binding site to which positively-charged amino acid residues can bind. In this binding site, formed by Phe above and Glu and Asp below, the bound amino acid is isolated from the extracellular and intracellular solvent (Figure

4-1)(45,130). As S4 moves, the Arg/Lys residues pass consecutively through the binding site, which likely serves as a catalytic center to lower the energy associated with the transfer of the gating charges (45,130). Therefore, it has also been referred to as the gating charge-transfer center (GTC). This mechanism is reminiscent of the selectivity filter of the pore: like the HCS, the selectivity filter is also the narrowest part of the pore (Figure 4-1)(51,130,134,135). Similar to the gating charges in the GTC, the conducted ions are also positioned precisely by amino-acid side chains that strip the ions of their hydration shell, and, thereby, catalyzing their transfer through the pore (130,134). In addition, both the HCS and the selectivity filter of the pore focus the electric field across the membrane over a very short distance. In the VSD, a major fraction of the electric field drops over the HCS that is only approx. 3-4 Å wide (41–44). Accordingly, gating charges do not have to pass the entire thickness of the membrane (~30 Å) but only the thickness of the HCS. Similarly, in the pore, 80% of the membrane voltage drops over the selectivity filter which is only 12 Å in length (136).

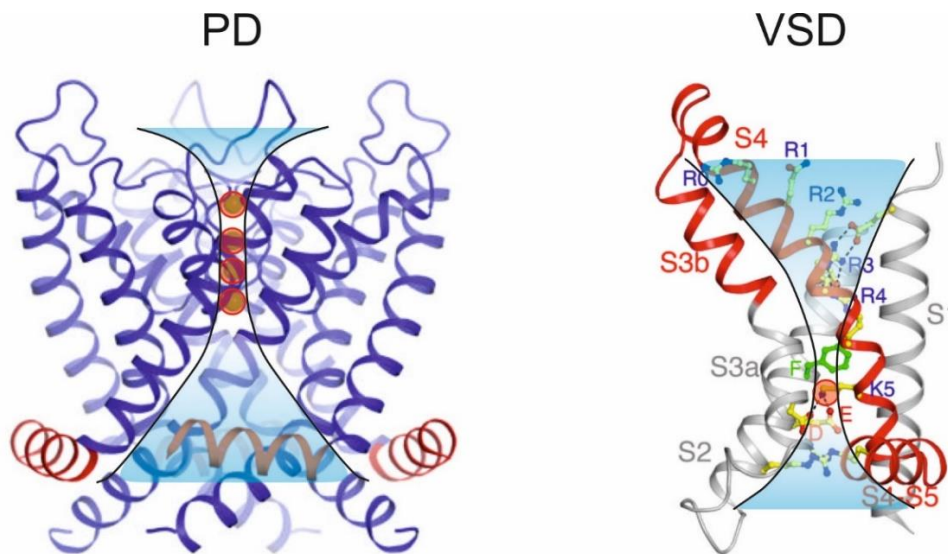


**Figure 4-1: Illustration comparing several key features of PD and VSD.** Ribbon representations depict a  $K_v$  channel chimera and are modified from (45). In the VSD, several important amino acid side chains are represented as stick model (regularly-spaced basic amino acids of S4 are labeled R0-K5) (45). Aqueous clefts (highlighted in blue) are separated by a narrow constriction that is inaccessible to water (white). This constriction contains binding sites (highlighted in red): four  $K^+$  binding sites in the PD ( $K^+$  ions are represented by green spheres) and one binding site for positively charged amino acid side-chains (occupied by a lysine side chain in the depicted conformation) in the VSD. In the PD, these binding sites are formed by carbonyl groups of the amino acids forming the selectivity filter sequence. In the VSD, the binding site is formed by a conserved phenylalanine in S2 (highlighted in green) and negatively charged amino acids in S2 and S3.

Normally, the GTC of the VSD is always occupied by one of the positively charged residues of S4 during gating, which prevents the passage of ions. However, mutations of Arg residues in S4 of  $K_v$ ,  $Na_v$ , and  $Ca_v$  channels can cause voltage-dependent currents to flow through the VSD, so-called gating-pore currents (110,111,137,138). Here, when S4 occupies certain positions during gating, no positive charge is located in the GTC, thus allowing ions to pass through the VSD. Some of these mutations have been identified in human voltage-gated channels that give rise to non-selective currents through the VSD and cause channelopathies (111,112,139). A similar mechanism may give rise to proton currents in drHCNL1. That said, gating-pore currents are typically unselective cation currents (139), whereas drHCNL1 is exquisitely proton selective. It is possible to introduce gating-pore proton currents by introducing a His residue in place of an Arg in S4 (138). Here, transient protonation of His allows selective shuttling of protons through the VSD. But given that drHCNL1 does not contain any His residues in that critical positions, the proton permeation and selectivity mechanism of HCNL1 must be fundamentally different.

Remarkably, introducing at position M169 an Arg residue that “fills the gap” in the string of regularly spaced Arg residues, abolishes proton permeation, and gating currents become apparent. Similarly, in  $H_v1$ , an Arg residue introduced at the fourth S4 position in register with the three other Arg residues, blocks proton permeation (87) and reveals gating currents (38,113). In this respect, HCNL1 and  $H_v1$  appear to share a similar mechanism of proton permeation.

This mechanism in  $H_v1$ , is not completely understood and is actively debated in the community. There are two competing theories (140,141). According to the first theory, protons are “shuttled” through the VSD by one or more titratable amino acids (140,142,143). Because the viral proton channel M2 uses four titratable His residues in its pore to conduct protons (144), it stands to reason that proton permeation in  $H_v1$  also involves titratable amino acids. The proposed mechanism is fundamentally different from that of other ion channels and more similar to the operating principle of proton pumps. These contain so-called “proton wires” which take advantage of the special properties of protons (145,146). In water, protons can move rapidly through the hydrogen-bonded network of water molecules by jumping from one water molecule to

its neighbor (this process is referred to as the Grotthus mechanism (147–149)). A linear chain of such hydrogen-bonded water molecules can be called a proton wire. Such wires also exist within proteins, where elements of the chain can also consist of protonatable amino acid side chains (145,146). This theory explains the extremely high proton selectivity of  $H_v1$  (no other ion has been shown to permeate), because protonatable amino acids can only shuttle protons. Another piece of evidence appears to support this theory: when  $H_v1$  is measured in  $D_2O$  (where the hydrogen of water is replaced by a deuterium), the conductance decreases by almost 50%, which is more than can be explained by the lower mobility of  $D^+$  ions (150). To test this hypothesis - hopping via amino acid side chains -, all titratable amino acids of  $H_v1$  were systematically neutralized but, surprisingly, none of these was required for proton conduction (151). This result suggests the first theory is likely not true. Further mutation studies identified the third arginine of S4 (R211) and an aspartate in S1 (D112) as the selectivity filter of  $H_v1$ ; replacing either with an uncharged amino acid resulted in a loss of selectivity (114,152).

As alternative theory, it was proposed that proton permeation in  $H_v1$  involves a pure “water wire” that does not involve protonation of any amino acid side chains (141,151). Within the channel, water molecules are stabilized to form a hydrogen-bonded chain over which protons traverse via the Grotthus mechanism. Charged amino acids interact with the water molecules and repel all other ions (114,152,153). While such a pore would obviously strongly favor protons, perfect selectivity seems unlikely. Although no other permeant ion has been identified so far, this could be due to technical limitations that prevent small changes in  $V_{rev}$  from being detected. In conclusion, neither of the two theories can be considered as definitively proven or disproven; however, the discovery of another ion channel, which possesses a similar but hyperpolarization-activated proton-permeation pathway, will give ample opportunities to gain insight into the requirements for proton pores in VSDs.

Recently, two papers appeared that show the movement of the VSD during hyperpolarization in HCN channels (47,48). These gave remarkable new insight into the gating of hyperpolarization-activated channel. Perhaps most surprising was the finding that the S4 helix “breaks” during the downward motion of activation and one segment moves parallel to the membrane. But, perhaps even more relevant to this

thesis, the work shows exactly which Arg in S4 occupied the GTC at any given time. In the depolarized state, R5 (which corresponds to R8 according to our numbering system) is positioned in the HCS. During the downward movement, the Arg residues pass the GTC one after the other; when this movement ends, R3 is positioned in the GTC. This places the serine residue in position 2 (S2, a gap within the Arg motif conserved among all HCN channels) opposite to the Phe, which forms the extracellular lid of the GTC (47,48). This finding was surprising to me. Given that my data underscore the importance of M169 (which correspond to R0 in the numbering system of the recent publications), I assumed that it would shift into the HCS during gating and thereby create a pore. But according to the new data, the methionine never came close to the critical Phe.

On the other hand, the new publications indicate the importance of the conserved serine. In HCN channels, it is positioned opposite the Phe of the GTC in the conformation at hyperpolarized potential. This is reminiscent of other mutations that cause gating pore currents, where, in certain conformations, no charge exists in the GTC. While there are currently no structures of H<sub>v</sub>1 in the open state, modelling approaches suggest that N4 occupies a similar position in the vicinity of the corresponding Phe (154).

Because I could not show any proton permeation through mmHCN2, which also contains the key Ser, it seems unlikely that the Ser alone is sufficient to induce a pore. The neutralization of an additional Arg by Met appears to be necessary. This is reminiscent of gating pore currents in *Shaker* where two adjacent positive charges must be neutralized to cause a gating pore current (137). In drHCNL1, we encounter two gaps as well, M169 and S175, which are not adjacent but separated by R172. Considering what we know from *Shaker*, no gating pore currents are expected in this situation. On the other hand, the ion selectivity of currents through double gaps in *Shaker* has been characterized for the first Arg position where a non-selective cation current has been observed that is common for most gating-pore currents. In drHCNL1 we observe a selective proton current. Moreover, H<sub>v</sub>1 is extremely selective for protons and contains no double gap. Possibly, M169 is required in drHCNL1 to form a hydrogen-bonded chain involving water molecules (and perhaps amino-acid side

groups) as a proton permeation pathway. In this context, serine could even be part of the chain, because it contains a hydroxyl group that can accept a proton.

The  $V_{rev}$  for proton currents is not affected by orders-of-magnitude higher concentrations of monovalent cations, indicating a more than a millionfold higher permeability for protons than for other ions. Indeed, the relative permeability of  $H^+$  vs.  $Na^+$  is  $3.01 \times 10^6$ , showing that the proton selectivities of HCNL1 and  $H_v1$  are of the same order of magnitude (155). This supports the hypothesis that drHCNL1 and  $H_v1$  likely conduct protons by a similar mechanism that distinguishes them from other, less selective proton channels such as M2 and Otopetrin. Channels that conduct ions through a classic PD typically have a much lower selectivity ( $P_{K^+}:P_{Na^+} = 1,000 - 10,000$  for  $K^+$  channels and  $P_{Na^+}:P_{K^+} = 100 - 500$  for  $Na^+$  channels (51,52,156,157)). Given the extremely low proton concentration in most physiological environments ( $10^{-7} - 10^{-7.5}$  M), this exquisite proton selectivity is essential for drHCNL1 to actually function as a proton-conducting channel.

The HCNL channel family consists of two groups: HCNL1 and HCNL2. Because only drHCNL1 could be functionally expressed, I can only hypothesize about the properties and function of HCNL2 channels. Their pore sequence is more conserved than that of HCNL1 channels and by and large resembles the canonical CIGYG motif of classic HCN (AISYG, QISYG, or ALSYG in three species) (Figure 6-1). All HCNL2 channels carry a Ser instead of the first Gly (SYG instead of GYG). The analogous Gly to Ser exchange renders the pore in  $K_v$  channels non-conducting (158), and a CISYG sequence in human HCN4 results in non-conducting, dominant-negative subunits (159). Therefore, the HCNL2 pore is probably non-functional as well. However, all HCNL2 channels carry the characteristic Met in S4, which is crucial for proton conduction in drHCNL1. Therefore, HCNL2 may also conduct protons via the same VSD pathway. In mice, the Otopetrin proton channel OTOP1 is required for the development of otoconia, small calcium carbonate-based crystals (126). Hundreds of these crystals are embedded in a protein scaffold to form an otoconial matrix. Because of its mass, the otoconial matrix can deflect mechanosensitive hair cells in the inner ear, thereby enabling the perception of gravity and acceleration (160). In zebrafish, HCNL2 transcripts are enriched in hair cells and in the inner ear (161). In contrast to the many,

small otoconia of mammals, fish possess a single large otolith in each otolithic organ (162). HCNL2 could have an analogous function to OTOP1 in mammals (i.e. a proton channel required for otolith formation). But it could also play a role in the function of sensory hair cells.

Finally, I will discuss the physiological role of drHCNL1 in zebrafish sperm. Across phyla,  $\text{Ca}^{2+}$  plays a central role in sperm motility (16). The sperm-specific  $\text{Ca}^{2+}$  channel CatSper mediates  $\text{Ca}^{2+}$  influx in many sperm, from marine invertebrates to humans (1,16) - but not all species. Cai et al showed that birds, amphibians, and teleost fish apparently lack CatSper channels (163). The channel(s) or mechanisms that promote  $\text{Ca}^{2+}$  influx into these sperm species are not known.

In sea urchin sperm, a chemoattractant secreted by the egg binds to a receptor guanylate cyclase. The synthesized cGMP opens a CNGK channel that hyperpolarizes the cell and in turn activates two other proteins: a sodium-proton exchanger (sNHE) that alkalizes sperm, and an HCN channel that depolarizes sperm. The alkalization shifts the voltage-dependence of CatSper to more negative values and thus CatSper is activated upon recovery from depolarization (164,165).

There are two components of the sea urchin signaling cascade that also exist in zebrafish sperm: drCNGK and drHCNL1 (as an analogue for HCN). At first glance, the properties of both channels seem to differ considerably from their sea urchin orthologues or paralogues. However, these differences might enable the two channels to preserve their signaling functions in the freshwater environment, and the interplay of drCNGK and drHCNL1 may lead to the activation of an unknown voltage-gated  $\text{Ca}^{2+}$  channel. In sea urchins, both CNGK and HCN are controlled by cyclic nucleotides (CNGK by cGMP (164,166) and HCN by cAMP (32)). In zebrafish, however, both channels are insensitive to cyclic nucleotides despite the conserved CNBD. Instead, drCNGK is controlled by  $\text{pH}_i$  (18,19). Additionally, drHCNL1 conducts protons instead of  $\text{Na}^+$  or  $\text{K}^+$  thus maintaining its ability to depolarize cells upon hyperpolarization despite the low concentration of  $\text{Na}^+$  and  $\text{K}^+$  in freshwater. Because of these variations, drHCNL1 counteracts hyperpolarization in two different ways: it carries an inward proton current (depolarizing the cell), and the resulting

acidification closes the alkaline-activated drCNGK channels (18,19)(preventing further hyperpolarization). The proton conductance of drHCNL1 and the  $\text{pH}_i$  sensitivity of drCNGK suggest that, instead of cyclic nucleotides, protons serve as cellular messengers in sperm of zebrafish. Both recovery after hyperpolarization and a change in  $\text{pH}_i$  are reminiscent of the mechanisms that open CatSper in sea urchin sperm (16,165). In zebrafish sperm, the release of caged calcium results in changes in the motility pattern, suggesting that  $\text{Ca}^{2+}$  may play a role in directed swimming towards the egg and/or the micropyle (19). Perhaps drHCNL1 serves to activate a (still unknown)  $\text{Ca}^{2+}$  channel that might play a role similar to that of CatSper in sea urchin sperm.

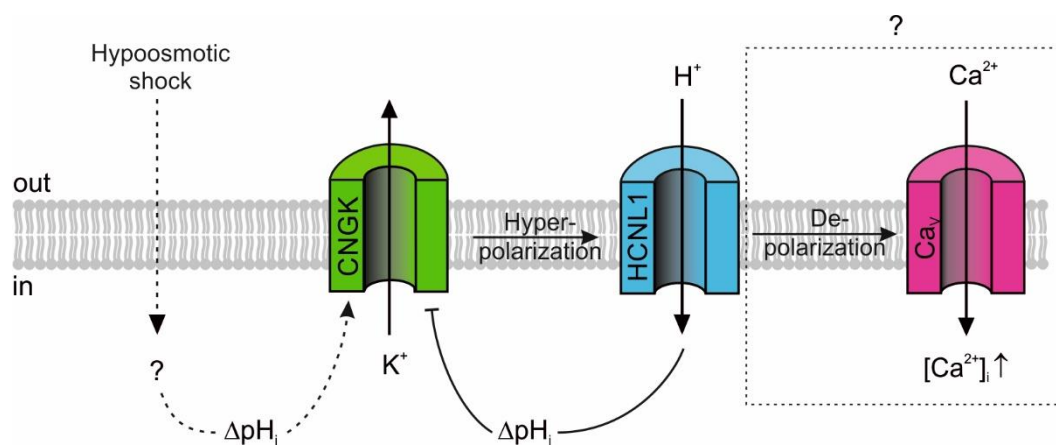


**Figure 4-2: Hypothesized signaling cascade of zebrafish sperm.** In freshwater, drCNGK hyperpolarizes the cell and activates drHCNL1, which in turn lowers  $\text{pH}_i$  and blocks drCNGK. The cascade could begin spontaneously upon release of the sperm if drCNGK is already open. Alternatively, the hypoosmotic shock cause activation of drCNGK via unknown signaling components upstream of drCNGK. The depolarization of drHCNL1 could activate a so far unknown voltage-gated  $\text{Ca}^{2+}$  channel, analogous to CatSper. Modified from (56).

Is there evidence for such a  $\text{Ca}^{2+}$  channel? Whereas teleost fish were previously believed to lack CatSper channels, recently, using genomics and immunological methods, evidence has emerged suggesting that some species may contain CatSper (or a very similar CatSper-like protein) (14,167,168). Furthermore, Yamanigachi and coworkers analyzed the swimming behavior of numerous fish sperm; they showed that extracellular  $\text{Ca}^{2+}$  is necessary for the final fusion of the sperm with the egg in all species. In addition, in some species sperm also lost the ability to locate the micropyle when extracellular  $\text{Ca}^{2+}$  was absent (14). Interestingly, in those species, evidence for a

CatSper channel was found. By contrast, in sperm species that can enter the micropyle even in the absence of extracellular  $\text{Ca}^{2+}$ , antibodies did not recognize CatSper proteins, and a genomic search yielded no results (Figure 4-3)(14,167,168).

These species lacking CatSper belong to the superorder *Ostariophysi*, the second largest superorder of teleost fishes encompassing about 28% of all species and 68% of freshwater species; almost all *Ostariophysi* species (~98.5%) live in freshwater (169) and *Danio rerio* is one of them (Figure 4-3). These findings, in particular the fact that sperm are motile and enter the micropyle even in the absence of extracellular  $\text{Ca}^{2+}$ , suggest that  $\text{Ca}^{2+}$  regulation in *Ostariophysi* is different. Considering that the superordinate clade of *Otomorpha* splits into the orders *Clupei*, *Alepocephali* (both encompassing only marine species) and *Ostariophysi* (containing almost exclusively freshwater species), it is possible that this independence from extracellular  $\text{Ca}^{2+}$  is an adaptation to the freshwater environment (169). However, there is evidence that sperm of *Cyprinus carpio* (that belongs to the *Ostariophysi* superorder) do not activate in the absence of extracellular  $\text{Ca}^{2+}$  (170).

A mechanism to elevate cytosolic  $\text{Ca}^{2+}$  in these species, is  $\text{Ca}^{2+}$  release from intracellular stores. Although sperm lack an endoplasmic reticulum (which acts as an intracellular  $\text{Ca}^{2+}$  store in most other cells), sperm may possess a different  $\text{Ca}^{2+}$  store - the redundant nuclear envelope (RNE) (171,172). It consists of membrane vesicles originating from excess nuclear envelope that is shed when the nucleus is condensed during spermiogenesis. In contrast to other excess organelles, the RNE is not discarded and is probably not - as the name suggests - redundant, but required for function. There is evidence that the RNE is involved in  $\text{Ca}^{2+}$  release during sperm hyperactivation (171–173). Although an analogous structure has not yet been identified in fish sperm, a cytoplasmic region exists where an RNE could be located (174). Alternatively, mitochondria may serve as intracellular  $\text{Ca}^{2+}$  stores (175).

So far, HCNL1 channels have been only identified in several species of the *Cyprinidae* family (cyprinids). Therefore, it is not clear whether the presence of HCNL1 comes along with independence of motility from extracellular  $\text{Ca}^{2+}$  in general or whether it is unique to cyprinids. In summary, zebrafish sperm might lack voltage-gated  $\text{Ca}^{2+}$

channels, and motility is regulated by release of  $\text{Ca}^{2+}$  from intracellular stores. I speculate that drHCN1 could trigger the release either directly (e.g. by changes in  $\text{pH}_i$ ) or indirectly (via other unknown proteins).

Nevertheless, differences in sperm physiology exist among cyprinids. Whereas zebrafish sperm acidify upon activation (Figure 3-26), sperm of *Cyprinus carpio* have been shown to alkalize (176).

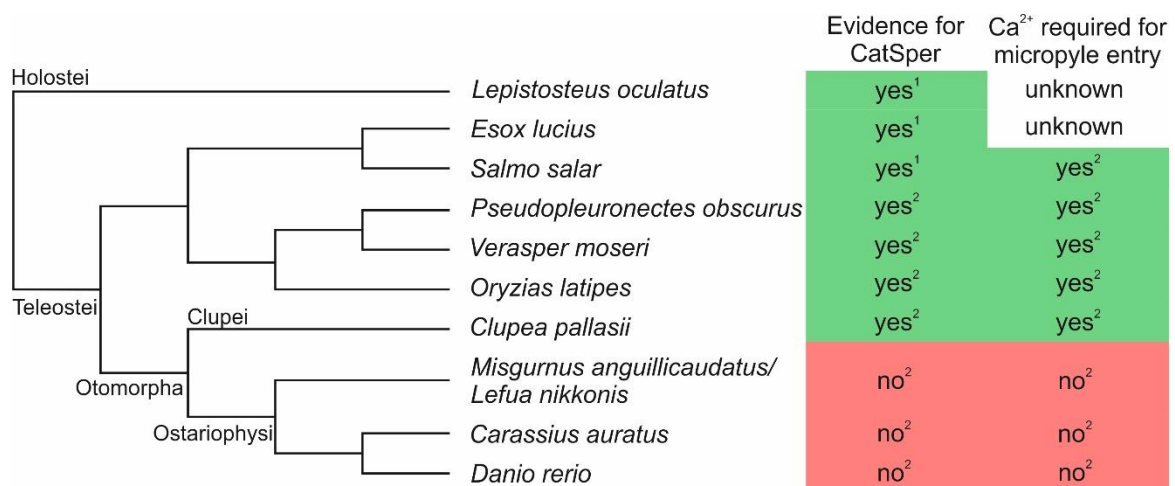


**Figure 4-3: Comparison of the properties of several fish sperm.** Simplified taxonomy tree of nine teleost fish (northern pike (*Esox lucius*), salmon (*Salmo salar*), black flounder (*Pseudopleuronectes obscurus*), barfin flounder (*Verasper moseri*), medaka (*Oryzias latipes*), Pacific herring (*Clupea pallasii*), loach (*Misgurnus anguillicaudatus* and *Lefua nikkonis*), goldfish (*Carassius auratus*) and zebrafish (*Danio rerio*)) and spotted gar (*Lepistosteus oculatus*). The branch length does not represent evolutionary rate. The taxonomy tree was created using the NCBI Taxonomy Common Tree tool (177). Properties of the sperm of the respective species. Indices indicate source publications (1: (167), 2: (14)).

When comparing sperm from different species, a common theme emerges: a number of seemingly similar signaling molecules can be identified across different species. However, closer inspection revealed that these signaling molecules differ drastically in their biophysical properties (16). This also holds for zebrafish sperm when compared to other sperm from mammals, sea urchin (16) but also other fish species like herring, medaka (14), and even carp (176). Further research is needed to understand these differences and to elucidate the entire signaling cascade in zebrafish sperm.

## 5 References

---

1. Wachten D, Jikeli JF, Kaupp UB. Sperm Sensory Signaling. *Cold Spring Harb Perspect Biol.* 2017 Jul;9(7).
2. Kholodnyy V, Gadêlha H, Cosson J, Boryshpolets S. How do freshwater fish sperm find the egg? The physicochemical factors guiding the gamete encounters of externally fertilizing freshwater fish. *Rev Aquac.* 2019 Aug 13;
3. Liu K, Petree C, Requena T, Varshney P, Varshney GK. Expanding the CRISPR Toolbox in Zebrafish for Studying Development and Disease. *Front Cell Dev Biol.* 2019 Mar 4;7.
4. Takai H, Morisawa M. Change in intracellular K<sup>+</sup> concentration caused by external osmolality change regulates sperm motility of marine and freshwater teleosts. *J Cell Sci.* 1995 Mar 1;108(3):1175–81.
5. Cosson J. Fish Sperm Physiology: Structure, Factors Regulating Motility, and Motility Evaluation. *Biol Res Aquat Sci.* 2019 Mar 29;
6. Jamieson BGM, Leung LK-P. Chapter 5: Introduction to fish spermatozoa. The significance of the micropyle in fertilization. In: *Fish Evolution and Systematics: Evidence from Spermatozoa: With a Survey of Lophophorate, Echinoderm and Protochordate Sperm and an Account of Gamete Cryopreservation.* Cambridge University Press; 1991. p. 56–72.
7. Wilson-Leedy JG, Kanuga MK, Ingermann RL. Influence of osmolality and ions on the activation and characteristics of zebrafish sperm motility. *Theriogenology.* 2009 Apr 15;71(7):1054–62.
8. Hart NH. Fertilization in teleost fishes: mechanisms of sperm-egg interactions. *Int Rev Cytol.* 1990;121:1–66.
9. Lee KW, Webb SE, Miller AL. A Wave of Free Cytosolic Calcium Traverses Zebrafish Eggs on Activation. *Dev Biol.* 1999 Oct 1;214(1):168–80.
10. Hart NH, Yu SF. Cortical granule exocytosis and cell surface reorganization in eggs of *Brachydanio*. *J Exp Zool.* 1980 Jul;213(1):137–59.
11. Darrow KO, Harris WA. Characterization and development of courtship in zebrafish, *Danio rerio*. *Zebrafish.* 2004;1(1):40–5.
12. Kashikar ND, Alvarez L, Seifert R, Gregor I, Jäckle O, Beyermann M, et al. Temporal sampling, resetting, and adaptation orchestrate gradient sensing in sperm. *J Cell Biol.* 2012 Sep 17;198(6):1075–91.

13. Yanagimachi R, Cherr G, Matsubara T, Andoh T, Harumi T, Vines C, et al. Sperm Attractant in the Micropyle Region of Fish and Insect Eggs. *Biol Reprod.* 2013 Feb 1;88(2).
14. Yanagimachi R, Harumi T, Matsubara H, Yan W, Yuan S, Hirohashi N, et al. Chemical and physical guidance of fish spermatozoa into the egg through the micropyle. *Biol Reprod.* 2017 Apr 1;96(4):780–99.
15. Yanagimachi R, Cherr GN, Pillai MC, Baldwin JD. Factors Controlling Sperm Entry into the Micropyles of Salmonid and Herring Eggs. *Dev Growth Differ.* 1992;34(4):447–61.
16. Kaupp UB, Strünker T. Signaling in Sperm: More Different than Similar. *Trends Cell Biol.* 2017 Feb 1;27(2):101–9.
17. Windler F, Bönigk W, Körschen HG, Grahn E, Strünker T, Seifert R, et al. The solute carrier SLC9C1 is a Na<sup>+</sup>/H<sup>+</sup>-exchanger gated by an S4-type voltage-sensor and cyclic-nucleotide binding. *Nat Commun.* 2018 18;9(1):2809.
18. Fechner S. Charakterisierung K<sup>+</sup>-selektiver zyklisch Nukleotid-gesteuerter Ionenkanäle aus *Danio rerio* und *Branchiostoma floridae*. [Bonn]: Rheinische Friedrich-Wilhelms-Universität Bonn; 2012.
19. Fechner S, Alvarez L, Bönigk W, Müller A, Berger TK, Pascal R, et al. A K<sup>+</sup>-selective CNG channel orchestrates Ca<sup>2+</sup> signalling in zebrafish sperm. Aldrich R, editor. *eLife.* 2015 Dec 9;4:e07624.
20. Brown HF, DiFrancesco D, Noble SJ. How does adrenaline accelerate the heart? *Nature.* 1979 Jul;280(5719):235–6.
21. Yanagihara K, Irisawa H. Inward current activated during hyperpolarization in the rabbit sinoatrial node cell. *Pflugers Arch.* 1980 May;385(1):11–9.
22. Pape H-C. Queer Current and Pacemaker: The Hyperpolarization-Activated Cation Current in Neurons. *Annu Rev Physiol.* 1996 Oct 1;58(1):299–327.
23. DiFrancesco D. Pacemaker Mechanisms in Cardiac Tissue. *Annu Rev Physiol.* 1993;55(1):455–72.
24. Kaupp UB, Seifert R. Molecular Diversity of Pacemaker Ion Channels. *Annu Rev Physiol.* 2001;63(1):235–57.
25. Robinson RB, Siegelbaum SA. Hyperpolarization-Activated Cation Currents: From Molecules to Physiological Function. *Annu Rev Physiol.* 2003;65(1):453–80.
26. Biel M, Wahl-Schott CA, Michalakis S, Zong X. Hyperpolarization-activated cation channels: from genes to function. *Physiol Rev.* 2009;89(3):847–85.

27. Gauss R, Seifert R. Pacemaker oscillations in heart and brain: a key role for hyperpolarization-activated cation channels. *Chronobiol Int.* 2000 Jul;17(4):453–69.
28. Sartiani L, Mannaioni G, Masi A, Romanelli MN, Cerbai E. The Hyperpolarization-Activated Cyclic Nucleotide–Gated Channels: from Biophysics to Pharmacology of a Unique Family of Ion Channels. *Pharmacol Rev.* 2017 Oct 1;69(4):354–95.
29. DiFrancesco D, Ferroni A, Mazzanti M, Tromba C. Properties of the hyperpolarizing-activated current (if) in cells isolated from the rabbit sino-atrial node. *J Physiol.* 1986 Aug;377:61–88.
30. Ludwig A, Zong X, Jeglitsch M, Hofmann F, Biel M. A family of hyperpolarization-activated mammalian cation channels. *Nature.* 1998 Jun;393(6685):587–91.
31. Santoro B, Liu DT, Yao H, Bartsch D, Kandel ER, Siegelbaum SA, et al. Identification of a gene encoding a hyperpolarization-activated pacemaker channel of brain. *Cell.* 1998 May 29;93(5):717–29.
32. Gauss R, Seifert R, Kaupp UB. Molecular identification of a hyperpolarization-activated channel in sea urchin sperm. *Nature.* 1998 Jun 11;393(6685):583–7.
33. Bezanilla F. How membrane proteins sense voltage. *Nat Rev Mol Cell Biol.* 2008 Apr;9(4):323–32.
34. Bezanilla F. Gating currents. *J Gen Physiol.* 2018 Jul 2;150(7):911–32.
35. White MM, Bezanilla F. Activation of squid axon K<sup>+</sup> channels. Ionic and gating current studies. *J Gen Physiol.* 1985 Apr 1;85(4):539–54.
36. Kitaguchi T, Sukhareva M, Swartz KJ. Stabilizing the Closed S6 Gate in the Shaker K<sup>v</sup> Channel Through Modification of a Hydrophobic Seal. *J Gen Physiol.* 2004 Oct 1;124(4):319–32.
37. Bezanilla F, Perozo E, Papazian DM, Stefani E. Molecular basis of gating charge immobilization in Shaker potassium channels. *Science.* 1991 Nov 1;254(5032):679–83.
38. Carmona EM, Larsson HP, Neely A, Alvarez O, Latorre R, Gonzalez C. Gating charge displacement in a monomeric voltage-gated proton (Hv1) channel. *Proc Natl Acad Sci U S A.* 2018 11;115(37):9240–5.
39. Villalba-Galea CA, Sandtner W, Starace DM, Bezanilla F. S4-based voltage sensors have three major conformations. *Proc Natl Acad Sci U S A.* 2008 Nov 18;105(46):17600–7.
40. Schoppa NE, McCormack K, Tanouye MA, Sigworth FJ. The size of gating charge in wild-type and mutant Shaker potassium channels. *Science.* 1992 Mar 27;255(5052):1712–5.

41. Starace DM, Bezanilla F. A proton pore in a potassium channel voltage sensor reveals a focused electric field. *Nature*. 2004 Feb;427(6974):548–53.
42. Islas LD, Sigworth FJ. Electrostatics and the Gating Pore of Shaker Potassium Channels. *J Gen Physiol*. 2001 Jan 1;117(1):69–90.
43. Ahern CA, Horn R. Focused Electric Field across the Voltage Sensor of Potassium Channels. *Neuron*. 2005 Oct 6;48(1):25–9.
44. Asamoah OK, Wuskell JP, Loew LM, Bezanilla F. A Fluorometric Approach to Local Electric Field Measurements in a Voltage-Gated Ion Channel. *Neuron*. 2003 Jan 9;37(1):85–98.
45. Tao X, Lee A, Limapichat W, Dougherty DA, MacKinnon R. A Gating Charge Transfer Center in Voltage Sensors. *Science*. 2010 Apr 2;328(5974):67–73.
46. Lee C-H, MacKinnon R. Structures of the Human HCN1 Hyperpolarization-Activated Channel. *Cell*. 2017 Jan 12;168(1):111–120.e11.
47. Lee C-H, MacKinnon R. Voltage Sensor Movements during Hyperpolarization in the HCN Channel. *Cell*. 2019 Dec 12;179(7):1582–1589.e7.
48. Kasimova MA, Tewari D, Cowgill JB, Ursuleaz WC, Lin JL, Delemotte L, et al. Helix breaking transition in the S4 of HCN channel is critical for hyperpolarization-dependent gating. Aldrich RW, editor. *eLife*. 2019 Nov 27;8:e53400.
49. Xue T, Eduardo M, Li RA. Dominant-Negative Suppression of HCN1- and HCN2-Encoded Pacemaker Currents by an Engineered HCN1 Construct. *Circ Res*. 2002 Jun 28;90(12):1267–73.
50. Er F, Larbig R, Ludwig A, Biel M, Hofmann F, Beuckelmann DJ, et al. Dominant-negative suppression of HCN channels markedly reduces the native pacemaker current  $I(f)$  and undermines spontaneous beating of neonatal cardiomyocytes. *Circulation*. 2003 Jan 28;107(3):485–9.
51. Doyle DA, Cabral JM, Pfuetzner RA, Kuo A, Gulbis JM, Cohen SL, et al. The Structure of the Potassium Channel: Molecular Basis of  $K^+$  Conduction and Selectivity. *Science*. 1998 Apr 3;280(5360):69–77.
52. Hille B. Selective Permeability: Independence. In: *Ion channels of excitable membranes*. 3. ed. Sunderland, Mass: Sinauer; 2001. p. 441–70.
53. Derebe MG, Sauer DB, Zeng W, Alam A, Shi N, Jiang Y. Tuning the ion selectivity of tetrameric cation channels by changing the number of ion binding sites. *Proc Natl Acad Sci*. 2011 Jan 11;108(2):598–602.
54. Craven KB, Zagotta WN. CNG and HCN channels: two peas, one pod. *Annu Rev Physiol*. 2006;68:375–401.

55. Wainger BJ, DeGennaro M, Santoro B, Siegelbaum SA, Tibbs GR. Molecular mechanism of cAMP modulation of HCN pacemaker channels. *Nature*. 2001 Jun 14;411(6839):805–10.
56. Wobig L. HCNL1: a hyperpolarization-activated, highly-selective proton channel in the sperm of the zebrafish *Danio rerio*. [Bonn]: Rheinische Friedrich-Wilhelms-Universität Bonn; 2016.
57. Wolfenstetter T. Characterization of the Hyperpolarization-Activated Proton Channel HCNL1. [Köln]: Universität zu Köln; 2019.
58. Wobig L, Wolfenstetter T, Fechner S, Bönigk W, Körschen HG, Jikeli JF, et al. A family of hyperpolarization-activated channels selective for protons. *Proc Natl Acad Sci*. 2020 May 28;
59. Liman ER, Tytgat J, Hess P. Subunit stoichiometry of a mammalian K<sup>+</sup> channel determined by construction of multimeric cDNAs. *Neuron*. 1992 Nov 1;9(5):861–71.
60. Bimboim HC, Doly J. A rapid alkaline extraction procedure for screening recombinant plasmid DNA. *Nucleic Acids Res*. 1979 Nov 24;7(6):1513–23.
61. Mullis K, Faloona F, Scharf S, Saiki R, Horn G, Erlich H. Specific enzymatic amplification of DNA in vitro: the polymerase chain reaction. *Cold Spring Harb Symp Quant Biol*. 1986;51 Pt 1:263–73.
62. Dalby B, Cates S, Harris A, Ohki EC, Tilkins ML, Price PJ, et al. Advanced transfection with Lipofectamine 2000 reagent: primary neurons, siRNA, and high-throughput applications. *Methods*. 2004 Jun 1;33(2):95–103.
63. Rosazza C, Haberl Meglic S, Zumbusch A, Rols M-P, Miklavcic D. Gene Electrotransfer: A Mechanistic Perspective. *Curr Gene Ther*. 2016 Apr 15;16(2):98–129.
64. Wong T-K, Neumann E. Electric field mediated gene transfer. *Biochem Biophys Res Commun*. 1982 Jul 30;107(2):584–7.
65. Boussif O, Lezoualc'h F, Zanta MA, Mergny MD, Scherman D, Demeneix B, et al. A versatile vector for gene and oligonucleotide transfer into cells in culture and in vivo: polyethylenimine. *Proc Natl Acad Sci*. 1995 Aug 1;92(16):7297–301.
66. Sonawane ND, Szoka FC, Verkman AS. Chloride Accumulation and Swelling in Endosomes Enhances DNA Transfer by Polyamine-DNA Polyplexes. *J Biol Chem*. 2003 Jul 11;278(45):44826–31.
67. Casey PJ, Solski PA, Der CJ, Buss JE. p21ras is modified by a farnesyl isoprenoid. *Proc Natl Acad Sci U S A*. 1989 Nov;86(21):8323–7.

68. Hancock JF, Magee AI, Childs JE, Marshall CJ. All ras proteins are polyisoprenylated but only some are palmitoylated. *Cell*. 1989 Jun 30;57(7):1167–77.
69. Wagman GH, Testa RT, Marquez JA, Weinstein MJ. Antibiotic G-418, a New Micromonospora-Produced Aminoglycoside with Activity Against Protozoa and Helminths: Fermentation, Isolation, and Preliminary Characterization. *Antimicrob Agents Chemother*. 1974 Aug;6(2):144–9.
70. Colbère-Garapin F, Horodniceanu F, Kourilsky P, Garapin AC. A new dominant hybrid selective marker for higher eukaryotic cells. *J Mol Biol*. 1981 Jul 25;150(1):1–14.
71. Bradford MM. A rapid and sensitive method for the quantitation of microgram quantities of protein utilizing the principle of protein-dye binding. *Anal Biochem*. 1976 May 7;72(1):248–54.
72. Smith PK, Krohn RI, Hermanson GT, Mallia AK, Gartner FH, Provenzano MD, et al. Measurement of protein using bicinchoninic acid. *Anal Biochem*. 1985 Oct 1;150(1):76–85.
73. Laemmli UK. Cleavage of Structural Proteins during the Assembly of the Head of Bacteriophage T4. *Nature*. 1970 Aug;227(5259):680–5.
74. Towbin H, Staehelin T, Gordon J. Electrophoretic transfer of proteins from polyacrylamide gels to nitrocellulose sheets: procedure and some applications. *Proc Natl Acad Sci U S A*. 1979 Sep;76(9):4350–4.
75. Burnette WN. “Western Blotting”: Electrophoretic transfer of proteins from sodium dodecyl sulfate-polyacrylamide gels to unmodified nitrocellulose and radiographic detection with antibody and radioiodinated protein A. *Anal Biochem*. 1981 Apr 1;112(2):195–203.
76. Coons AH, Creech HJ, Jones RN, Berliner E. The Demonstration of Pneumococcal Antigen in Tissues by the Use of Fluorescent Antibody. *J Immunol*. 1942 Nov 1;45(3):159–70.
77. Zilly FE, Halemani ND, Walrafen D, Spitta L, Schreiber A, Jahn R, et al. Ca<sup>2+</sup> induces clustering of membrane proteins in the plasma membrane via electrostatic interactions. *EMBO J*. 2011 Apr 6;30(7):1209–20.
78. Hille B. Voltage-gated Calcium Channels. In: *Ion channels of excitable membranes*. 3. ed. Sunderland, Mass: Sinauer; 2001. p. 95–130.
79. Hille B. Classical biophysics of the giant squid axon. In: *Ion channels of excitable membranes*. 3. ed. Sunderland, Mass: Sinauer; 2001. p. 25–60.

80. Hamill OP, Marty A, Neher E, Sakmann B, Sigworth FJ. Improved patch-clamp techniques for high-resolution current recording from cells and cell-free membrane patches. *Pflüg Arch*. 1981 Aug 1;391(2):85–100.
81. Molleman A. Basic Theoretical Principles. In: Patch clamping: an introductory guide to patch clamp electrophysiology. New York: J. Wiley; 2003. p. 5–42.
82. Halliwell JV, Whitaker MJ, Ogden D. Voltage clamp techniques. In: Ogden D, editor. *Microelectrode techniques: the Plymouth workshop handbook*. Cambridge: Company of Biologists; 1994. p. 17–35.
83. Kruh J. Effects of sodium butyrate, a new pharmacological agent, on cells in culture. *Mol Cell Biochem*. 1981 May 1;42(2):65–82.
84. Palermo DP, DeGraaf ME, Marotti KR, Rehberg E, Post LE. Production of analytical quantities of recombinant proteins in Chinese hamster ovary cells using sodium butyrate to elevate gene expression. *J Biotechnol*. 1991 Jun 1;19(1):35–47.
85. Ramsey IS, Moran MM, Chong JA, Clapham DE. A voltage-gated proton-selective channel lacking the pore domain. *Nature*. 2006 Apr;440(7088):1213–6.
86. Sasaki M, Takagi M, Okamura Y. A Voltage Sensor-Domain Protein Is a Voltage-Gated Proton Channel. *Science*. 2006 Apr 28;312(5773):589–92.
87. Tombola F, Ulbrich MH, Isacoff EY. The Voltage-Gated Proton Channel Hv1 Has Two Pores, Each Controlled by One Voltage Sensor. *Neuron*. 2008 May 22;58(4):546–56.
88. Armstrong CM, Bezanilla F. Currents Related to Movement of the Gating Particles of the Sodium Channels. *Nature*. 1973 Apr;242(5398):459–61.
89. Armstrong CM, Bezanilla F. Charge Movement Associated with the Opening and Closing of the Activation Gates of the Na Channels. *J Gen Physiol*. 1974 May 1;63(5):533–52.
90. Bright GR, Fisher GW, Rogowska J, Taylor DL. Chapter 6 Fluorescence Ratio Imaging Microscopy. In: Taylor DL, Wang Y-L, editors. *Methods in Cell Biology*. Academic Press; 1989. p. 157–92.
91. Hilgemann DW. The Giant Membrane Patch. In: Sakmann B, Neher E, editors. *Single-Channel Recording*. Boston, MA: Springer US; 1995. p. 307–27.
92. Dempster J. A new version of the Strathclyde Electrophysiology software package running within the Microsoft Windows environment. *J Physiol*. 1997 Nov;504(Suppl.):P57–P57.
93. Barry PH. JPCalc, a software package for calculating liquid junction potential corrections in patch-clamp, intracellular, epithelial and bilayer measurements and for correcting junction potential measurements. *J Neurosci Methods*. 1994 Jan 1;51(1):107–16.

94. Jaworski GHM, Talling JF, Heaney SI. Potassium dependence and phytoplankton ecology: an experimental study. *Freshw Biol.* 2003;48(5):833–40.
95. Livingstone CD, Barton GJ. Protein sequence alignments: a strategy for the hierarchical analysis of residue conservation. *Bioinformatics.* 1993 Dec 1;9(6):745–56.
96. Ludwig A, Zong X, Stieber J, Hullin R, Hofmann F, Biel M. Two pacemaker channels from human heart with profoundly different activation kinetics. *EMBO J.* 1999 May 4;18(9):2323–9.
97. Cukkemane A, Seifert R, Kaupp UB. Cooperative and uncooperative cyclic-nucleotide-gated ion channels. *Trends Biochem Sci.* 2011 Jan 1;36(1):55–64.
98. Zagotta WN, Olivier NB, Black KD, Young EC, Olson R, Gouaux E. Structural basis for modulation and agonist specificity of HCN pacemaker channels. *Nature.* 2003 Sep 11;425(6954):200–5.
99. Tibbs GR, Liu DT, Leybold BG, Siegelbaum SA. A State-independent Interaction between Ligand and a Conserved Arginine Residue in Cyclic Nucleotide-gated Channels Reveals a Functional Polarity of the Cyclic Nucleotide Binding Site. *J Biol Chem.* 1998 Feb 20;273(8):4497–505.
100. Bubis J, Neitzel JJ, Saraswat LD, Taylor SS. A point mutation abolishes binding of cAMP to site A in the regulatory subunit of cAMP-dependent protein kinase. *J Biol Chem.* 1988 Jul 15;263(20):9668–73.
101. Harzheim D, Pfeiffer KH, Fabritz L, Kremmer E, Buch T, Waisman A, et al. Cardiac pacemaker function of HCN4 channels in mice is confined to embryonic development and requires cyclic AMP. *EMBO J.* 2008 Feb 20;27(4):692–703.
102. Zheng J, Sigworth FJ. Selectivity Changes during Activation of Mutant Shaker Potassium Channels. *J Gen Physiol.* 1997 Aug 1;110(2):101–17.
103. Hanke W, Boheim G. The lowest conductance state of the alamethicin pore. *Biochim Biophys Acta BBA - Biomembr.* 1980 Mar 13;596(3):456–62.
104. Schneggenburger R, Ascher P. Coupling of Permeation and Gating in an NMDA-Channel Pore Mutant. *Neuron.* 1997 Jan 1;18(1):167–77.
105. De-la-Rosa V, Suárez-Delgado E, Rangel-Yescas GE, Islas LD. Currents through Hv1 channels deplete protons in their vicinity. *J Gen Physiol.* 2016 Feb 1;147(2):127–36.
106. Goldman DE. Potential, impedance, and rectification in membranes. *J Gen Physiol.* 1943 Sep 20;27(1):37–60.
107. Hodgkin AL, Katz B. The effect of sodium ions on the electrical activity of the giant axon of the squid. *J Physiol.* 1949;108(1):37–77.

108. Payandeh J, Scheuer T, Zheng N, Catterall WA. The crystal structure of a voltage-gated sodium channel. *Nature*. 2011 Jul 10;475(7356):353–8.
109. Jiang Y, Lee A, Chen J, Ruta V, Cadene M, Chait BT, et al. X-ray structure of a voltage-dependent K<sup>+</sup> channel. *Nature*. 2003 May;423(6935):33–41.
110. Tombola F, Pathak MM, Isacoff EY. Voltage-Sensing Arginines in a Potassium Channel Permeate and Occlude Cation-Selective Pores. *Neuron*. 2005 Feb 3;45(3):379–88.
111. Sokolov S, Scheuer T, Catterall WA. Gating pore current in an inherited ion channelopathy. *Nature*. 2007 Mar;446(7131):76–8.
112. Jurkat-Rott K, Groome JR, Lehmann-Horn F. Pathophysiological Role of Omega Pore Current in Channelopathies. *Front Pharmacol*. 2012;3.
113. De La Rosa V, Ramsey IS. Gating Currents in the Hv1 Proton Channel. *Biophys J*. 2018 Jun 19;114(12):2844–54.
114. Berger TK, Isacoff EY. The Pore of the Voltage-Gated Proton Channel. *Neuron*. 2011 Dec 22;72(6):991–1000.
115. Shin KS, Rothberg BS, Yellen G. Blocker State Dependence and Trapping in Hyperpolarization-Activated Cation Channels: Evidence for an Intracellular Activation Gate. *J Gen Physiol*. 2001 Feb 1;117(2):91–102.
116. Hong L, Pathak MM, Kim IH, Ta D, Tombola F. Voltage-Sensing Domain of Voltage-Gated Proton Channel Hv1 Shares Mechanism of Block with Pore Domains. *Neuron*. 2013 Jan 23;77(2):274–87.
117. Hong L, Kim IH, Tombola F. Molecular determinants of Hv1 proton channel inhibition by guanidine derivatives. *Proc Natl Acad Sci U S A*. 2014 Jul 8;111(27):9971–6.
118. Chávez JC, Darszon A, Treviño CL, Nishigaki T. Quantitative Intracellular pH Determinations in Single Live Mammalian Spermatozoa Using the Ratiometric Dye SNARF-5F. *Front Cell Dev Biol*. 2020 Jan 17;7.
119. Nishigaki T, Wood CD, Shiba K, Baba SA, Darszon A. Stroboscopic illumination using light-emitting diodes reduces phototoxicity in fluorescence cell imaging. *BioTechniques*. 2006 Aug;41(2):191–7.
120. Icha J, Weber M, Waters JC, Norden C. Phototoxicity in live fluorescence microscopy, and how to avoid it. *BioEssays*. 2017;39(8):1700003.
121. Dixit R, Cyr R. Cell damage and reactive oxygen species production induced by fluorescence microscopy: effect on mitosis and guidelines for non-invasive fluorescence microscopy. *Plant J*. 2003;36(2):280–90.

122. Gorgidze LA, Oshemkova SA, Vorobjev IA. Blue light inhibits mitosis in tissue culture cells. *Biosci Rep.* 1998 Aug;18(4):215–24.
123. Lee S-Y, Letts JA, MacKinnon R. Dimeric subunit stoichiometry of the human voltage-dependent proton channel Hv1. *Proc Natl Acad Sci.* 2008 Jun 3;105(22):7692–5.
124. Koch HP, Kurokawa T, Okochi Y, Sasaki M, Okamura Y, Larsson HP. Multimeric nature of voltage-gated proton channels. *Proc Natl Acad Sci.* 2008 Jul 1;105(26):9111–6.
125. Alavi SMH, Cosson J. Sperm motility in fishes. (II) Effects of ions and osmolality: A review. *Cell Biol Int.* 2006;30(1):1–14.
126. Tu Y-H, Cooper AJ, Teng B, Chang RB, Artiga DJ, Turner HN, et al. An evolutionarily conserved gene family encodes proton-selective ion channels. *Science.* 2018 02;359(6379):1047–50.
127. Chizhnikov IV, Geraghty FM, Ogden DC, Hayhurst A, Antoniou M, Hay AJ. Selective proton permeability and pH regulation of the influenza virus M2 channel expressed in mouse erythroleukaemia cells. *J Physiol.* 1996 Jul 15;494 ( Pt 2):329–36.
128. Shimbo K, Brassard DL, Lamb RA, Pinto LH. Ion selectivity and activation of the M2 ion channel of influenza virus. *Biophys J.* 1996 Mar;70(3):1335–46.
129. Goldstein SAN. A Structural Vignette Common to Voltage Sensors and Conduction Pores: Canaliculi. *Neuron.* 1996 Apr 1;16(4):717–22.
130. Shen H, Zhou Q, Pan X, Li Z, Wu J, Yan N. Structure of a eukaryotic voltage-gated sodium channel at near-atomic resolution. *Science.* 2017 03;355(6328).
131. Campos FV, Chanda B, Roux B, Bezanilla F. Two atomic constraints unambiguously position the S4 segment relative to S1 and S2 segments in the closed state of Shaker K channel. *Proc Natl Acad Sci U S A.* 2007 May 8;104(19):7904–9.
132. Long SB, Campbell EB, MacKinnon R. Crystal Structure of a Mammalian Voltage-Dependent Shaker Family K<sup>+</sup> Channel. *Science.* 2005 Aug 5;309(5736):897–903.
133. Long SB, Tao X, Campbell EB, MacKinnon R. Atomic structure of a voltage-dependent K<sup>+</sup> channel in a lipid membrane-like environment. *Nature.* 2007 Nov;450(7168):376–82.
134. Zhou Y, Morais-Cabral JH, Kaufman A, MacKinnon R. Chemistry of ion coordination and hydration revealed by a K<sup>+</sup> channel–Fab complex at 2.0 Å resolution. *Nature.* 2001 Nov;414(6859):43–8.
135. Naranjo D, Moldenhauer H, Pincuntureo M, Díaz-Franulic I. Pore size matters for potassium channel conductance. *J Gen Physiol.* 2016 Oct 1;148(4):277–91.

136. Yellen G, Jurman ME, Abramson T, MacKinnon R. Mutations affecting internal TEA blockade identify the probable pore-forming region of a K<sup>+</sup> channel. *Science*. 1991 Feb 22;251(4996):939–42.
137. Gamal El-Din TM, Heldstab H, Lehmann C, Greeff NG. Double gaps along Shaker S4 demonstrate omega currents at three different closed states. *Channels Austin Tex*. 2010 Apr;4(2):93–100.
138. Starace DM, Stefani E, Bezanilla F. Voltage-Dependent Proton Transport by the Voltage Sensor of the Shaker K<sup>+</sup> Channel. *Neuron*. 1997 Dec 1;19(6):1319–27.
139. Moreau A, Gosselin-Badaroudine P, Chahine M. Biophysics, pathophysiology, and pharmacology of ion channel gating pores. *Front Pharmacol*. 2014 Apr 3;5.
140. DeCoursey TE. CrossTalk proposal: Proton permeation through HV1 requires transient protonation of a conserved aspartate in the S1 transmembrane helix. *J Physiol*. 2017;595(22):6793–5.
141. Bennett AL, Ramsey IS. CrossTalk opposing view: proton transfer in Hv1 utilizes a water wire, and does not require transient protonation of a conserved aspartate in the S1 transmembrane helix. *J Physiol*. 2017;595(22):6797–9.
142. DeCoursey TE. Voltage-gated Proton Channels. *Compr Physiol*. 2012 Apr;2(2):1355–85.
143. Dudev T, Musset B, Morgan D, Cherny VV, Smith SME, Mazmanian K, et al. Selectivity Mechanism of the Voltage-gated Proton Channel, HV1. *Sci Rep*. 2015 May 8;5.
144. Acharya R, Carnevale V, Fiorin G, Levine BG, Polishchuk AL, Balannik V, et al. Structure and mechanism of proton transport through the transmembrane tetrameric M2 protein bundle of the influenza A virus. *Proc Natl Acad Sci U S A*. 2010 Aug 24;107(34):15075–80.
145. Nagle JF, Morowitz HJ. Molecular mechanisms for proton transport in membranes. *Proc Natl Acad Sci U S A*. 1978 Jan;75(1):298–302.
146. Buch-Pedersen MJ, Pedersen BP, Veierskov B, Nissen P, Palmgren MG. Protons and how they are transported by proton pumps. *Pflugers Arch*. 2009 Jan;457(3):573–9.
147. Agmon N. The Grotthuss mechanism. *Chem Phys Lett*. 1995 Oct 13;244(5):456–62.
148. Cukierman S. Et tu, Grotthuss! and other unfinished stories. *Biochim Biophys Acta BBA - Bioenerg*. 2006 Aug 1;1757(8):876–85.
149. de Grotthuss T. Sur la décomposition de l'eau et des corps qu'elle tient en dissolution à l'aide de l'électricité galvanique. *Ann Chim*. 1806;(LVIII):54–74.

150. DeCoursey TE, Cherny VV. Deuterium isotope effects on permeation and gating of proton channels in rat alveolar epithelium. *J Gen Physiol.* 1997 Apr;109(4):415–34.
151. Ramsey IS, Mokrab Y, Carvacho I, Sands ZA, Sansom MSP, Clapham DE. An aqueous H<sup>+</sup> permeation pathway in the voltage-gated proton channel Hv1. *Nat Struct Mol Biol.* 2010 Jul;17(7):869–75.
152. Musset B, Smith SME, Rajan S, Morgan D, Cherny VV, Decoursey TE. Aspartate 112 is the selectivity filter of the human voltage-gated proton channel. *Nature.* 2011 Oct 23;480(7376):273–7.
153. Chamberlin A, Qiu F, Wang Y, Noskov SY, Larsson HP. Mapping the gating and permeation pathways in the voltage-gated proton channel Hv1. *J Mol Biol.* 2015 Jan 16;427(1):131–45.
154. Chamberlin A, Qiu F, Rebolledo S, Wang Y, Noskov SY, Larsson HP. Hydrophobic plug functions as a gate in voltage-gated proton channels. *Proc Natl Acad Sci U S A.* 2014 Jan 14;111(2):E273–282.
155. DeCoursey TE. The Voltage-Gated Proton Channel: A Riddle, Wrapped in a Mystery, inside an Enigma. *Biochemistry.* 2015 Jun 2;54(21):3250–68.
156. Kellenberger S, Auberson M, Gautschi I, Schneeberger E, Schild L. Permeability properties of ENaC selectivity filter mutants. *J Gen Physiol.* 2001 Dec;118(6):679–92.
157. Palmer LG. Ion selectivity of the apical membrane Na channel in the toad urinary bladder. *J Membr Biol.* 1982;67(2):91–8.
158. Marguet SL, Le-Schulte VTQ, Merseburg A, Neu A, Eichler R, Jakovcevski I, et al. Treatment during a vulnerable developmental period rescues a genetic epilepsy. *Nat Med.* 2015 Dec;21(12):1436–44.
159. Schlusche AK. The role of HCN channels in the prenatal development of the cerebral cortex in the mouse (*Mus musculus*, Linnaeus 1758). [Köln]: Universität zu Köln; 2016.
160. Carlström D. A crystallographic study of vertebrate otoliths. *Biol Bull.* 1963 Dec 1;125(3):441–63.
161. Erickson T, Nicolson T. Identification of sensory hair-cell transcripts by thiouracil-tagging in zebrafish. *BMC Genomics.* 2015 Oct 23;16.
162. Campana SE. Chemistry and composition of fish otoliths: pathways, mechanisms and applications. *Mar Ecol Prog Ser.* 1999 Nov 3;188:263–97.

163. Cai X, Clapham DE. Evolutionary Genomics Reveals Lineage-Specific Gene Loss and Rapid Evolution of a Sperm-Specific Ion Channel Complex: CatSper and CatSper $\beta$ . *PLOS ONE*. 2008 Oct 30;3(10):e3569.
164. Strünker T, Weyand I, Bönigk W, Van Q, Loogen A, Brown JE, et al. A K<sup>+</sup>-selective cGMP-gated ion channel controls chemosensation of sperm. *Nat Cell Biol*. 2006 Oct;8(10):1149–54.
165. Seifert R, Flick M, Bönigk W, Alvarez L, Trötschel C, Poetsch A, et al. The CatSper channel controls chemosensation in sea urchin sperm. *EMBO J*. 2015 Feb 3;34(3):379–92.
166. Bönigk W, Loogen A, Seifert R, Kashikar N, Klemm C, Krause E, et al. An Atypical CNG Channel Activated by a Single cGMP Molecule Controls Sperm Chemotaxis. *Sci Signal*. 2009 Oct 27;2(94):ra68–ra68.
167. Romero F, Nishigaki T. Comparative genomic analysis suggests that the sperm-specific sodium/proton exchanger and soluble adenylyl cyclase are key regulators of CatSper among the Metazoa. *Zool Lett*. 2019 Jul 26;5.
168. Lissabet JFB, Herrera Belén L, Lee-Estevez M, Risopatrón J, Valdebenito I, Figueroa E, et al. The CatSper channel is present and plays a key role in sperm motility of the Atlantic salmon (*Salmo salar*). *Comp Biochem Physiol A Mol Integr Physiol*. 2020 Mar 1;241:110634.
169. Nelson JS. *Fishes of the World*. Wiley; 2006. 632 p.
170. Krasznai Z, Márián T, Izumi H, Damjanovich S, Balkay L, Trón L, et al. Membrane hyperpolarization removes inactivation of Ca<sup>2+</sup> channels, leading to Ca<sup>2+</sup> influx and subsequent initiation of sperm motility in the common carp. *Proc Natl Acad Sci U S A*. 2000 Feb 29;97(5):2052–7.
171. Ho H-C, Suarez SS. Characterization of the Intracellular Calcium Store at the Base of the Sperm Flagellum That Regulates Hyperactivated Motility. *Biol Reprod*. 2003 May 1;68(5):1590–6.
172. Suarez SS. Control of hyperactivation in sperm. *Hum Reprod Update*. 2008 Nov 1;14(6):647–57.
173. Harper CV, Publicover SJ. Reassessing the role of progesterone in fertilization-compartmentalized calcium signalling in human spermatozoa? *Hum Reprod Oxf Engl*. 2005 Oct;20(10):2675–80.
174. Verma DK, Routray P, Dash C, Dasgupta S, Jena JK. Physical and Biochemical Characteristics of Semen and Ultrastructure of Spermatozoa in Six Carp Species. *Turk J Fish Aquat Sci*. 2009 Jan 1;9(1):67–76.

175. Walsh C, Barrow S, Voronina S, Chvanov M, Petersen OH, Tepikin A. Modulation of calcium signalling by mitochondria. *Biochim Biophys Acta*. 2009 Nov;1787(11):1374–82.
176. Krasznai Z, Márián T, Balkay L, Gáspár R, Trón L. Potassium channels regulate hypo-osmotic shock-induced motility of common carp (*Cyprinus carpio*) sperm. *Aquaculture*. 1995 Jan 1;129(1):123–8.
177. Common Taxonomy Tree [Internet]. Available from: <https://www.ncbi.nlm.nih.gov/Taxonomy/CommonTree/wwwcmt.cgi>

# 6 Appendix

Type	Name	Accession	Species	S4 sequence	Pore sequence
HCN	hsHCN1	O60741	<i>Homo sapiens</i>	RALRIVRF <sup>S</sup> FTKIL <sup>S</sup> LLRLLRLSRLIRY	CIGYG
	hsHCN2	NP_001185	<i>Homo sapiens</i>	RALRIVRF <sup>S</sup> FTKIL <sup>S</sup> LLRLLRLSRLIRY	CIGYG
	mmHCN2	NP_032252	<i>Mus musculus</i>	RALRIVRF <sup>S</sup> FTKIL <sup>S</sup> LLRLLRLSRLIRY	CIGYG
	splh	NP_999729	<i>Strongylocentrotus purpuratus</i>	RALKILRF <sup>S</sup> AKLL <sup>S</sup> LLRLLRLSRLMRF	CIGYG
	drHCN2	XP_685414	<i>Danio rerio</i>	RALRIVRF <sup>S</sup> FTKIL <sup>S</sup> LLRLLRLSRLIRY	CIGYG
HCNL1	drHCN1	XP_002662296	<i>Danio rerio</i>	KMVRILMF <sup>S</sup> ARFL <sup>S</sup> MI <sup>S</sup> RLLRVPKLLRF	WPFLE
	agHCN1	ROL49041	<i>Anabarrilius grahami</i>	KMVRILMF <sup>S</sup> V <sup>S</sup> RL <sup>S</sup> LI <sup>S</sup> RLLRVPKLLRF	WRSTE
	ccHCN1	KTF78698	<i>Cyprinus carpio</i>	KLVRILMF <sup>S</sup> ARIL <sup>S</sup> LI <sup>S</sup> RLLRVSRLVRF	WISTK
	caHCN1	XP_026142770	<i>Carassius auratus</i>	KLVRILMF <sup>S</sup> V <sup>S</sup> RIF <sup>S</sup> MI <sup>S</sup> RLLRVPKLLRF	WISTK
	lrHCN1	RXN35273	<i>Labeo rohita</i>	KLVRILMF <sup>S</sup> ARIF <sup>S</sup> MI <sup>S</sup> RLLRVPKLLRF	WISTK
	saHCN1	XP_016308039	<i>Sinocyclocheilus anshuiensis</i>	KLVRILMF <sup>S</sup> ARIF <sup>S</sup> MI <sup>S</sup> RLLRVPKLLRF	WISTN
	srHCN1	XP_016403257	<i>Sinocyclocheilus rhinoceros</i>	KLVRILMF <sup>S</sup> ARIF <sup>S</sup> MI <sup>S</sup> RLLRVPKLLRF	WISTN
	sgHCN1	XP_016148351	<i>Sinocyclocheilus grahami</i>	KLVRILMF <sup>S</sup> ARIF <sup>S</sup> MI <sup>S</sup> RLLRVPKLLRF	WISTN
	drHCN2	XP_009302941	<i>Danio rerio</i>	KMMRILMF <sup>S</sup> V <sup>S</sup> RII <sup>S</sup> LV <sup>S</sup> RLRVSRLVRF	AISYG
	saHCN2	XP_016316371	<i>Sinocyclocheilus anshuiensis</i>	KMMRILMF <sup>S</sup> V <sup>S</sup> RII <sup>S</sup> LV <sup>S</sup> RLRVSRLVRF	AISYG
	srHCN2	XP_016372923	<i>Sinocyclocheilus rhinoceros</i>	KMMRILMF <sup>S</sup> V <sup>S</sup> RII <sup>S</sup> LV <sup>S</sup> RLRVSRLVRF	AISYG
	sgHCN2	XP_016110760	<i>Sinocyclocheilus grahami</i>	KMMRILMF <sup>S</sup> V <sup>S</sup> RII <sup>S</sup> LV <sup>S</sup> RLRVSRLVRF	AISYG
	ipHCN2	XP_017333189	<i>Ictalurus punctatus</i>	KMVRILMF <sup>S</sup> V <sup>S</sup> RII <sup>S</sup> LV <sup>S</sup> RLRVSRLVRF	AISYG
	phHCN2	XP_026783384	<i>Pangasianodon hypophthalmus</i>	KMVRILMF <sup>S</sup> V <sup>S</sup> RII <sup>S</sup> LV <sup>S</sup> RLRVSRLVRF	AISYG
	amHCN2	XP_007255663	<i>Astyanax mexicanus</i>	KMVRILMF <sup>S</sup> V <sup>S</sup> RII <sup>S</sup> LV <sup>S</sup> RLRVSRLVRF	AISYG
	okHCN2	XP_020355314	<i>Oncorhynchus kisutch</i>	RMVRILMF <sup>S</sup> V <sup>S</sup> RII <sup>S</sup> LV <sup>S</sup> RLRVSRLVRF	QISYG
	omHCN2	CDQ60601	<i>Oncorhynchus mykiss</i>	RMVRILMF <sup>S</sup> V <sup>S</sup> RII <sup>S</sup> LV <sup>S</sup> RLRVSRLVRF	QISYG
	salHCN2	XP_023836590	<i>Salvelinus alpinus</i>	RMVRILMF <sup>S</sup> V <sup>S</sup> RII <sup>S</sup> LV <sup>S</sup> RLRVSRLVRF	QISYG
	ssHCN2	XP_014020263	<i>Salmo salar</i>	RMVRILMF <sup>S</sup> V <sup>S</sup> RII <sup>S</sup> LV <sup>S</sup> RLRVSRLVRF	QISYG
eIHCN2	XP_010878553	<i>Esox lucius</i>	RMVRILMF <sup>S</sup> V <sup>S</sup> RII <sup>S</sup> LV <sup>S</sup> RLRVSRLVRF	QIAYG	
loHCN2	XP_015219515	<i>Lepisosteus oculatus</i>	KLVRILMF <sup>S</sup> ARIF <sup>S</sup> LI <sup>S</sup> RLLRVSRLMRF	GISYG	
oIHCN2	XP_023806527	<i>Oryzias latipes</i>	KMMRILMF <sup>S</sup> V <sup>S</sup> RII <sup>S</sup> LI <sup>S</sup> RLARVSRLVRF	ALSYG	
omeHCN2	XP_024116361	<i>Oryzias melastigma</i>	KMMRILMF <sup>S</sup> V <sup>S</sup> RII <sup>S</sup> LI <sup>S</sup> RLARVSRLVRF	ALSYG	
nfhHCN2	XP_015821332	<i>Nothobranchius furzeri</i>	KMMRILMF <sup>S</sup> V <sup>S</sup> RII <sup>S</sup> LI <sup>S</sup> RLARVSRLVRF	ALSYG	
aIHCN2	XP_013888580	<i>Austrofundulus limnaeus</i>	KMMRILMF <sup>S</sup> V <sup>S</sup> RII <sup>S</sup> LI <sup>S</sup> RLARVSRLVRF	ALSYG	
prHCN2	XP_008429740	<i>Poecilia reticulata</i>	KMMRILMF <sup>S</sup> V <sup>S</sup> RII <sup>S</sup> LI <sup>S</sup> RLARVSRLVRF	ALSYG	
xmHCN2	XP_023193182	<i>Xiphophorus maculatus</i>	RMMRILMF <sup>S</sup> V <sup>S</sup> RII <sup>S</sup> LI <sup>S</sup> RLARVSRLVRF	ALSYG	
gaHCN2	PWA15592	<i>Gambusia affinis</i>	RMMRILMF <sup>S</sup> V <sup>S</sup> RII <sup>S</sup> LI <sup>S</sup> RLARVSRLVRF	ALSYG	
cvHCN2	XP_015234384	<i>Cyprinodon variegatus</i>	KMMRILMF <sup>S</sup> V <sup>S</sup> RII <sup>S</sup> LI <sup>S</sup> RLARVSRLVRF	ALSYG	
tnHCN2	CAG08228	<i>Tetraodon nigroviridis</i>	KMMRILMF <sup>S</sup> V <sup>S</sup> RII <sup>S</sup> LI <sup>S</sup> RLARVSRLVRF	ALSYG	
nbHCN2	XP_006793668	<i>Neolamprologus brichardi</i>	RMMRILMF <sup>S</sup> V <sup>S</sup> RII <sup>S</sup> LI <sup>S</sup> RLARVSRLVRF	ALSYG	
mzHCN2	XP_004573060	<i>Maylandia zebra</i>	KMMRILMF <sup>S</sup> V <sup>S</sup> RII <sup>S</sup> LI <sup>S</sup> RLARVSRLVRF	ALSYG	
pnHCN2	XP_005745343	<i>Pundamilia nyererei</i>	KMMRILMF <sup>S</sup> V <sup>S</sup> RII <sup>S</sup> LI <sup>S</sup> RLARVSRLVRF	ALSYG	
onHCN2	XP_003456651	<i>Oreochromis niloticus</i>	KMMRILMF <sup>S</sup> V <sup>S</sup> RII <sup>S</sup> LI <sup>S</sup> RLARVSRLVRF	ALSYG	
pfhHCN2	XP_016516411	<i>Poecilia formosa</i>	KMMRILMF <sup>S</sup> V <sup>S</sup> RII <sup>S</sup> LI <sup>S</sup> RLARVSRLVRF	ALSYG	
pmHCN2	XP_014842027	<i>Poecilia mexicana</i>	KMMRILMF <sup>S</sup> V <sup>S</sup> RII <sup>S</sup> LI <sup>S</sup> RLARVSRLVRF	ALSYG	
plHCN2	XP_014874297	<i>Poecilia latipinna</i>	KMMRILMF <sup>S</sup> V <sup>S</sup> RII <sup>S</sup> LI <sup>S</sup> RLARVSRLVRF	ALSYG	
csHCN2	XP_008326741	<i>Cynoglossus semilaevis</i>	KMMRILMF <sup>S</sup> V <sup>S</sup> RII <sup>S</sup> LI <sup>S</sup> RLARVSRLVRF	ALSYG	
kmHCN2	XP_017285643	<i>Kryptolebias marmoratus</i>	KMMRILMF <sup>S</sup> V <sup>S</sup> RII <sup>S</sup> LI <sup>S</sup> RLARVSRLVRF	ALSYG	
lcrHCN2	XP_010732351	<i>Larimichthys crocea</i>	KMMRILMF <sup>S</sup> V <sup>S</sup> RII <sup>S</sup> LI <sup>S</sup> RLARVSRLVRF	ALSYG	
lbcHCN2	XP_020487588	<i>Labrus bergylta</i>	KMMRILMF <sup>S</sup> V <sup>S</sup> RII <sup>S</sup> LI <sup>S</sup> RLARVSRLVRF	ALSYG	
apHCN2	XP_022073802	<i>Acanthochromis polyacanthus</i>	RMMRILMF <sup>S</sup> V <sup>S</sup> RII <sup>S</sup> LI <sup>S</sup> RLARVSRLVRF	ALSYG	
sdHCN2	XP_022596779	<i>Seriola dumerili</i>	KMMRILMF <sup>S</sup> V <sup>S</sup> RII <sup>S</sup> LI <sup>S</sup> RLARVSRLVRF	ALSYG	
sldHCN2	XP_023258015	<i>Seriola lalandi dorsalis</i>	KMMRILMF <sup>S</sup> V <sup>S</sup> RII <sup>S</sup> LI <sup>S</sup> RLARVSRLVRF	ALSYG	
lacaHCN2	XP_018559851	<i>Lates calcarifer</i>	KMMRILMF <sup>S</sup> V <sup>S</sup> RII <sup>S</sup> LI <sup>S</sup> RLARVSRLVRF	ALSYG	
pefHCN2	XP_028446135	<i>Perca flavescens</i>	KMMRILMF <sup>S</sup> V <sup>S</sup> RII <sup>S</sup> LI <sup>S</sup> RLARVSRLVRF	ALSYG	
poHCN2	XP_019956126	<i>Paralichthys olivaceus</i>	KMMRILMF <sup>S</sup> V <sup>S</sup> RII <sup>S</sup> LI <sup>S</sup> RLARVSRLVRF	ALSYG	
hcHCN2	XP_019736565	<i>Hippocampus comes</i>	RMMRILMF <sup>S</sup> V <sup>S</sup> RII <sup>S</sup> LI <sup>S</sup> RLARVSRLVRF	ALSYG	
smHCN2	AWP13541	<i>Scopthalmus maximus</i>	KMMRILMF <sup>S</sup> V <sup>S</sup> RII <sup>S</sup> LI <sup>S</sup> RLARVSRLVRF	ALSYG	
lchCN	XP_014344895	<i>Latimeria chalumnae</i>	RLFRIL <sup>S</sup> LLARVLS <sup>S</sup> LLRLLRFSRLMRL	CIGYG	

Figure 6-1: HCN, HCNL1, and HCNL2 channels and their signature sequences of S4 and the conventional pore. Conserved key amino acids are color-coded.

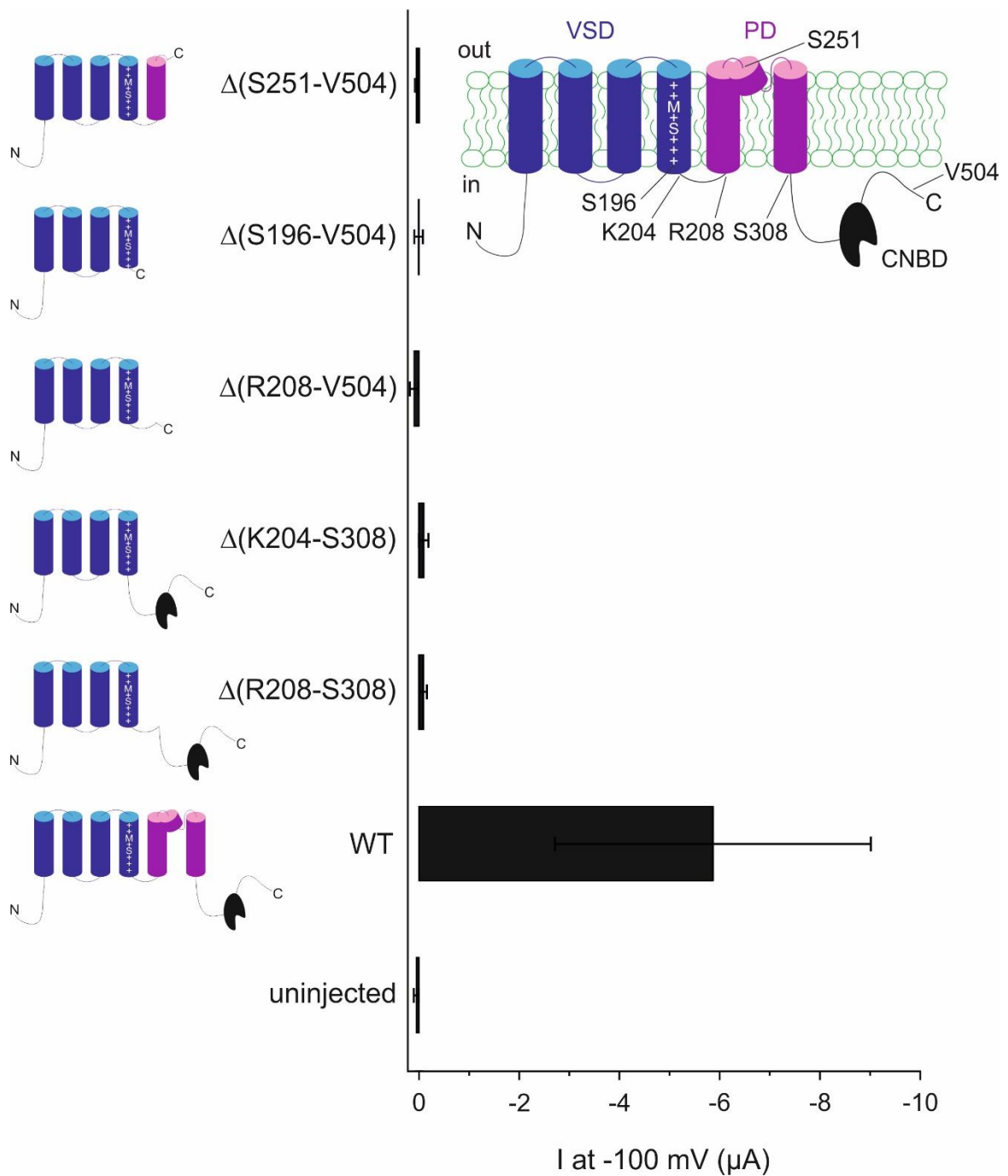


**Figure 6-2: TEVC recordings of drHCNL1-WT, various truncated drHCNL1 constructs and various drHCNL1-Splh/mmHCN2 chimera.** Inward current amplitude in response to a hyperpolarizing voltage step (-100 mV), measured in *X. laevis* oocytes injected with various truncated drHCNL1 constructs (drHCNL1- $\Delta(S251-V504)$ , n = 7; drHCNL1- $\Delta(S196-V504)$ , n = 5; drHCNL1- $\Delta(R208-V504)$ , n = 6; drHCNL1- $\Delta(K204-S308)$ , n = 10; drHCNL1- $\Delta(R208-S308)$ , n = 6; drHCNL1-WT, n = 4; uninjected, n = 16). Amplitudes were measured 0.3 s after stimulus onset and leak-subtracted. Error bars denote standard deviation.

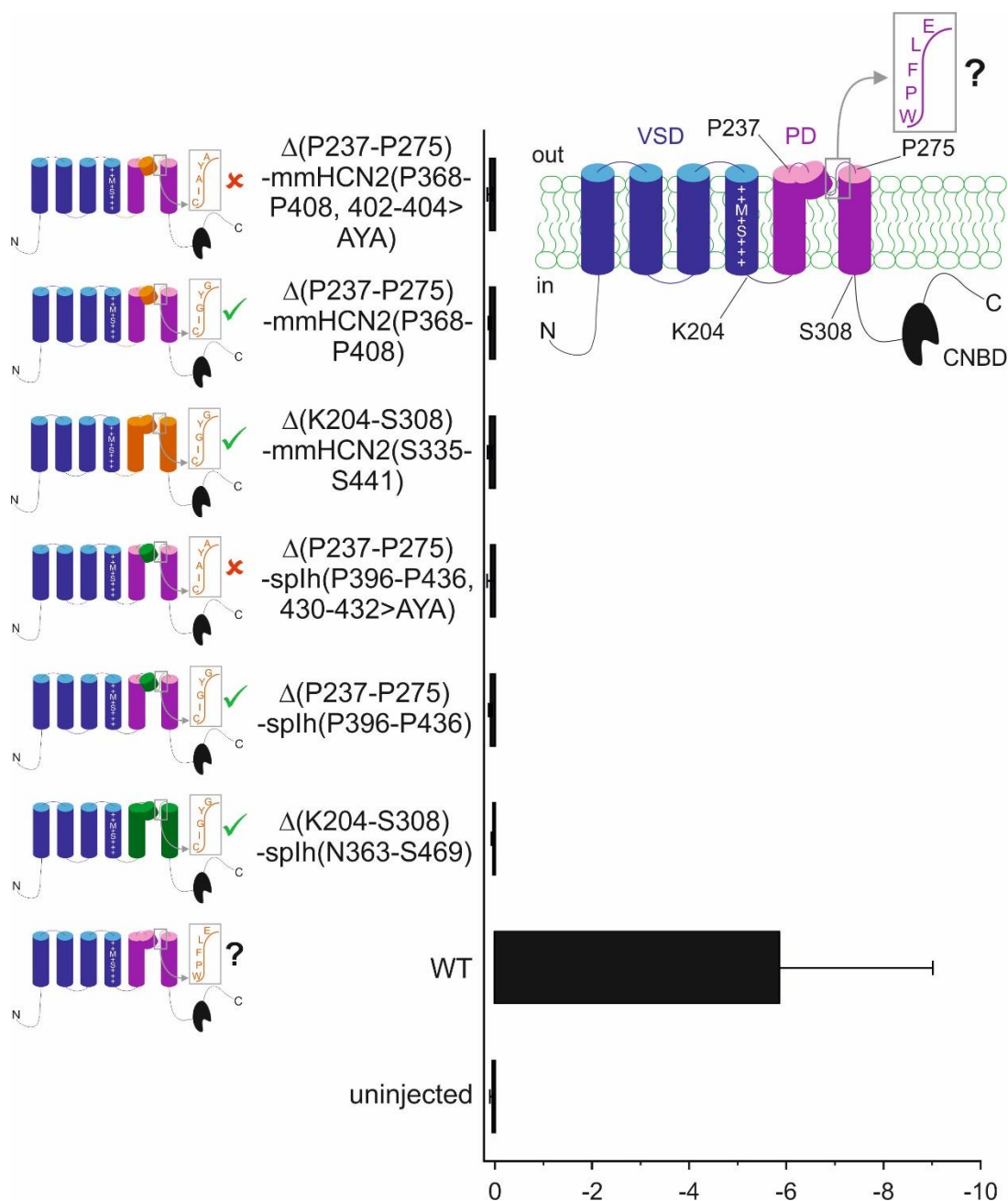


**Figure 6-3: TEVC recordings of drHCNL1-WT, various truncated drHCNL1 constructs and various drHCNL1-splh/mmHCN2 chimera.** Inward current amplitude in response to a hyperpolarizing voltage step (-100 mV), measured in *X. laevis* oocytes injected with various drHCNL1-splh/mmHCN2-chimera. Some constructs contain the sequence AYA instead of GYG in the selectivity filter sequence (indicated by “404-404>AYA”/”430-432>AYA”), which should result in a construct with a non-conducting pore. Constructs that are expected to contain a functional pore domain are indicated with a green check mark and constructs that are expected to contain a non-conducting pore with a red cross. (drHCNL1-  $\Delta(P237-P275)$ -mmHCN2(P368-P408, 402-404>AYA), n=8; drHCNL1-  $\Delta(P237-P275)$ -mmHCN2(P368-P408), n=15; drHCNL1-  $\Delta(K204-S308)$ -mmHCN2(P335-P441), n=11; drHCNL1-  $\Delta(P237-P275)$ -splh(P396-P436, 430-432>AYA), n=12; drHCNL1-  $\Delta(P237-P275)$ -splh(P396-P436), n=14; drHCNL1-  $\Delta(K204-S308)$ -splh(N363-S469), n=14; drHCNL1-WT, n = 4; uninjected, n = 16). Amplitudes were measured 0.3 s after stimulus onset and leak-subtracted. Error bars denote standard deviation.

# Acknowledgements

---

I would like to thank the following persons; without them this thesis could not have been realized:

- Prof. Dr. U. Benjamin Kaupp for the opportunity to work on this exciting project, his close interest in my work, and for supporting me as a scientist throughout my time at the caesar.
- Dr. Reinhard Seifert for his dedicated work as my supervisor, for introducing me to a fascinating field of research, and for all the extremely helpful discussion, criticism and advice.
- Dr. Thomas Berger for all his scientific advice, for sharing his immense knowledge and enthusiasm for proton pores and the great collaboration on this project.
- Dr. Michael Pankratz for acting as second reviewer on this thesis, his continued interest in my work and always asking the right questions.
- Dr. Wolfgang Bönigk and Dr. Heinz Körschen for their advice and help in molecular biology and protein biochemistry, and Jessica Görden and Sybille Wolf-Kümmeth for the great technical assistance.
- All my fellow PhD students for making my time at the caesar such a wonderful experience. I would especially like to thank Thérèse Wolfenstetter for the great collaboration on this project and being an excellent colleague; Tobias Zbik and Kai Korsching for all the great discussions in our lab meetings; Moritz Schladt, Elena Grahn and Thérèse Wolfenstetter (again) for being amazing office mates and all the lively discussions about science and other topics; and Florian Windler for all his support and advice throughout my time working on this thesis.
- Heike Krause for all her advice and help on organizational matters and more.

I would also like to thank my family and friends for all their support, I couldn't have done it without you.